UPPSALA
UNIVERSITET

Defect Thermodynamics and Kinetics in Polyanionic Cathodes

A Theoretical Roadmap for Na-ion based Batteries and Hybrid Supercapacitors

TEERAPHAT WATCHARATHARAPONG

Dissertation presented at Uppsala University to be publicly examined in Room 80101, Ångströmlaboratoriet, Lägerhyddsvägen 1, Uppsala, Wednesday, 22 May 2019 at 09:15 for the degree of Doctor of Philosophy. The examination will be conducted in English. Faculty examiner: Assoc. Prof. Dr. Palani Balaya (National University of Singapore, Singapore).

Abstract

Watcharatharapong, T. 2019. Defect Thermodynamics and Kinetics in Polyanionic Cathodes. A Theoretical Roadmap for Na-ion based Batteries and Hybrid Supercapacitors. *Digital Comprehensive Summaries of Uppsala Dissertations from the Faculty of Science and Technology* 1796. 92 pp. Uppsala: Acta Universitatis Upsaliensis. ISBN 978-91-513-0628-5.

In this thesis, the framework of the density functional theory is employed to study and predict properties of polyanionic cathodes for Na-ion batteries and hybrid supercapacitors. It consists of three main parts as follows:

The first part is primarily dedicated to kröhnkite-type $Na_2Fe(SO_4)_2 2H_2O$ cathode. The major goal is to probe diffusion mechanisms of Na^+ ions. The chemical potentials diagrams for the pentrary compound are determined under thermodynamic equilibrium and are used to calculate pH value for solution-based synthesis. We find that the presence of Na_{Fe} facilitates a faster migration and reduces the channel blockage issue. Moreover, the defect concentration can be tuned by controlling the pH condition. We conclude that defects and small hole polarons play a role in ionic and electronic conductivity.

The second part focuses on alluaudite-type $Na_{2+2\delta}Fe_{2-\delta}(SO_4)_3$ (NFSδ). We unveil the effect of the non-stoichiometry on the thermodynamics, defect nature, and voltage profiles NFSδ with δ = 0, 0.25 and 0.5. The relation between Na ion distribution and energetics is studied and reveals the necessity of using a supercell model. Chemical potential diagrams indicate an inevitable impurity precipitation in all cases, but can be reduced at low δ. Defect formation analysis shows an unlikely formation of channel blockage and can explain the impurity precipitation in experiment. Two types of phase transition are observed after half-desodiation. A higher degree of non-stoichiometry offers an improvement in specific capacity and structural reversibility for NFS0.25 and NFS0.5. The voltage profiles and formation energy reveal the Na intercalation mechanism and strategy to enhance the specific capacity.

The third part is associated with battery-type cathodes used in hybrid supercapacitors, namely the $NaMPO_4$ and $MMoO_4$ (where M is a transition metal). We find that triphylite $NaNiPO_4$ shows a better electrochemical performance as compared to maricite phase due to the merit of intercalation mechanism. A mixed-$NaMn_{1/3}Co_{1/3}Ni_{1/3}PO_4$ is predicted to show faradaic behavior, mainly contributed from the Ni and Mn redox reactions, along with an improved electronic conductivity. Moreover, the effect of M substitution on phase stability, electronic properties and charge transfer is also studied in $MMoO_4$ with M = Mn, Co and Ni. The highest capacitance is predicted for $NiMoO_4$ amongst the others and is attributed to the higher active surface area. To compromise the capacitance and cycling stability, $Mn_{1/3}Co_{1/3}Ni_{1/3}MoO_4$ is synthesized. We predict its crystal structure by using the SQS method. Based on electronic structure, we can identify a source of the improved cycling efficiency and specific capacitance of this mixed compound.

Keywords: DFT, Energy Materials, Defects, Chemical potentials, Kinetics, Hybrid supercapacitors, Na-ion batteries, Polyanionic cathodes

Teeraphat Watcharatharapong, Department of Physics and Astronomy, Materials Theory, Box 516, Uppsala University, SE-751 20 Uppsala, Sweden.

Dedicated to my beloved parents & family

List of papers

This thesis is based on the following papers, which are referred to in the text by their Roman numerals.

I **Mechanistic study of Na-ion diffusion and small polaron formation in Kröhnkite $Na_2Fe(SO_4)_2 \cdot 2H_2O$ based cathode materials**
T. Watcharatharapong, J. T-Thienprasert, P. Barpanda, R. Ahuja, S. Chakraborty
Journal of Materials Chemistry A, 2017, 5 (41), 21726-21739

II **Defect formations and pH-dependent kinetics in Kröhnkite $Na_2Fe(SO_4)_2 \cdot 2H_2O$ based cathode for sodium-ion batteries: Resembling synthesis conditions through chemical potential landscape**
T. Watcharatharapong, J. T-Thienprasert, S. Chakraborty, R. Ahuja
Nano Energy, 2019, 55, 123-134

III **Defect thermodynamics in alluaudite-based polyanionic materials: A theoretical insight of non-stoichiometry influences**
T. Watcharatharapong, S. Chakraborty, R. Ahuja
Under revision in Physical Review Materials

IV **Mapping sodium intercalation mechanism, electrochemical properties and structural evolution in non-stoichiometric alluaudite $Na_{2+2\delta}Fe_{2-\delta}(SO_4)_3$ cathode materials**
T. Watcharatharapong, S. Chakraborty, R. Ahuja
Submitted

V **Current computational trends in polyanionic cathode materials for Li and Na batteries**
S. Chakraborty, A. Banerjee, *T. Watcharatharapong*, R.B. Araujo, R. Ahuja
Journal of Physics: Condensed Matter, 2018, 30 (28), 283003

VI **Effect of transition metal cations on stability enhancement for molybdate-based hybrid supercapacitor**
T. Watcharatharapong, M. Minakshi, S. Chakraborty, D. Li, G.M. Shafiullah, R.D. Aughterson, R. Ahuja
ACS applied materials & interfaces, 2017, 9 (21), 17977â17991

VII **A combined theoretical and experimental approach of a new ternary metal oxide in molybdate composite for hybrid energy storage capacitors**
M Minakshi, *T. Watcharatharapong*, S. Chakraborty, R. Ahuja
APL Materials, 2018, 6, 047701

VIII **Synthesis, and crystal and electronic structure of sodium metal phosphate for use as a hybrid capacitor in non-aqueous electrolyte**
M. Minakshi, *T. Watcharatharapong*, S. Chakraborty, R. Ahuja, S. Duraisamy, P.T. Rao, N. Munichandraiah
Dalton Transactions, 2015, 44, 20108-20120

IX **Synthesis, structural and electrochemical properties of sodium nickel phosphate for energy storage devices**
M. Minakshi, D. Mitchell, R. Jones, F. Alenazey, *T. Watcharatharapong*, S. Chakraborty, R. Ahuja
Nanoscale, 2016, 8, 11291-11305

Reprints were made with permission from the publishers.

Comments on my own contributions:
For the articles I, II, III and IV, I had the main responsibility for designing the projects, performing calculations, analyzing the results, making the figures and writing the manuscript. Article V is in collaboration with my colleagues in Condensed Matter Theory Group. I participated in designing parts of the project and writing the parts relevant to defects and phosphate/sulfate polyanionic cathodes for Na-ion batteries. Articles VI, VII, VIII and IX are the outcomes of theory-experiment collaborations. I took a responsibility for performing calculations, analyzing data and writing in the theoretical parts of the manuscripts.

List of papers not included

The following papers were also made during the time frame of this thesis, but are not included in the thesis.

I **Structural prediction of host-guest structure in lithium at high pressure**
P. Tsuppayakorn-aek, W. Luo, *T. Watcharatharapong*, R. Ahuja, T. Bovornratanaraks
Scientific reports, 2015, 8, 5278

II **An uncompensated semimetal with extremely large magnetoresistance and signature of strong spin-orbital coupling in MoTe$_2$**
M. Abdel-Hafiez, *T. Watcharatharapong*, S. Chakraborty, Z. Guo, R. Ahuja, H. K. Mao
*Submitted*

Contents

1. Introduction

Energy is the pivotal requisite of modern era, that drives the continuous and rapid development of science and technology. For many centuries, we are utterly being reliant on the dominant energy resource from fossil fuels, like coal, natural gas, petroleum etc., due to their high energy efficiency and historical abundance. However, the relentless energy consumption have raised several concerns regarding their depleting reservoir, rising price and, especially, the drastic emission of CO_2 gas, which is the most reasonable factor behind global warming in present generation. These threats have posed a major challenge for the scientific community to expeditiously seek alternative energy sources that can provide a long-term solution from sustainable energy perspective. In this regard, numerous attempts have been made to rigorously explore and develop technologies over decades for renewable energy generation from various natural sources such as solar, wind, biomass and geothermal energies. Nevertheless, according to the variable and intermittent nature of renewable energy sources, the sustainable energy cycle will be never been replenished if the harvested energies are not effectively stored to facilitate the on-demand utilization.

As more advanced technologies for renewable energies are being developed, the subsequent need for energy storage becomes increasingly important and indispensable. Energy storage plays an important role in helping balance supply and demand through short- to long-term storage duration by converting electrical energy into another form to be stored. They can be classified by five major groups, namely mechanical, chemical (e.g., hydrogen storage), thermal, electrochemical (e.g., battery) and electrical systems (e.g., supercapacitor) [26], which have various specifications, benefits and limitations suitable for different technologies and applications. Among all of them, Li-ion batteries (LIBs) are the most viable and influential energy storage in our modern society, which can store electrical energy as chemical energy within its two electrodes. They have drawn a great deal of attention owing to several advantages in terms of energy density, power density, cyclability, storage efficiency and scalability for a broad range of functions from small-scale electronic devices, electric vehicles (EVs), robotics to the large grid based energy systems.

1.1 Fundamentals of Li- and Na-ion rechargeable batteries

As the milestone of energy evolution, the Li-ion battery was first commercialized in 1991 following the fundamental researches of Goodenough [39, 84]. This prototype cell is primarily composed of: (i) two electrodes, namely $LiCoO_2$ layered oxide cathode (positive) and graphite anode (negative), where electrical energy is stored in chemical form, (ii) an electrolyte, where Li^+ exchange takes place between two electrodes, (iii) a separator which allows the Li^+ ion diffusion but prevents an electron conduction through electrolyte, and (iv) an external circuit where electrons are circulating between two electrodes under a load (during discharging), or a power source (during charging). Figure 1.1 illustrates the main components and the direction of an ion-electron transport during discharging process in LIBs. In this state, the oxidation reaction occurs in anode, giving away a free electron (e^-) and a Li^+ ion. While the electron is migrating through the external circuit due to the higher voltage in cathode side, the Li^+ ion is instantaneously diffusing through a non-aqueous electrolyte and intercalating into the cathode to maintain the charge neutrality in the cell, This leads to a reduction reaction of $Co^{3+/2+}$, enabling the Li ion to be stored and hence completing the energy delivering. In the charging reaction, all of these processes is reversed by applying a voltage. The overall charging/discharging reactions can be written as follows,

$$LiCoO_2 + C(graphite) \iff Li_{1-x}CoO_2 + Li_xC \quad ; [3.7V] \qquad (1.1)$$
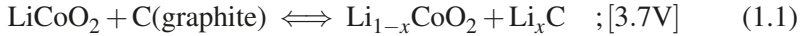
This cathode offers the high voltage at 3.7 V (or 4.2 V vs. Li/Li^+) with the high specific energy of 140 mAh/g [69, 104] and is extensively used in various applications, especially for personal electronic devices till date. However, it comes at the price of the major concerns as safety issues. Since the key element that limits a battery performance is the active element of cathode [56], researchers pay a great deal of attention to explore alternative choices for superior cathode materials.

In 1997, the new generation of LIB cathodes was introduced and widely known as $LiFePO_4$ polyanion-type cathode [91]. It adopts an olivine structure (orthorhombic; *Pnma* spacegroup) with the characteristic framework of FeO_6 octahedra and PO_4 tetrahedra. Compared to $LiCoO_2$, $LiFePO_4$ does not only open up the possibility of using Fe-based cathode, which is cheaper and less toxic than Co, but also delivers the higher specific energy (170 mAh/g) and high thermal stability [117] due to the strong covalent bonding in PO_4 tetrahedra. These advantages make them more attractive and suitable for EV and stationary storage applications. Importantly, this foundation stone inspires and opens up the intensive quests for a variety of $LiM(X_mO_n)$ polyanionic cathodes where $n = 2m+1$ for X = B, or $n = 3m+1$ for X = Si, P, S, As, Mo or W [38, 77]. According to the inductive effect proposed by Padhi et al. [91], the
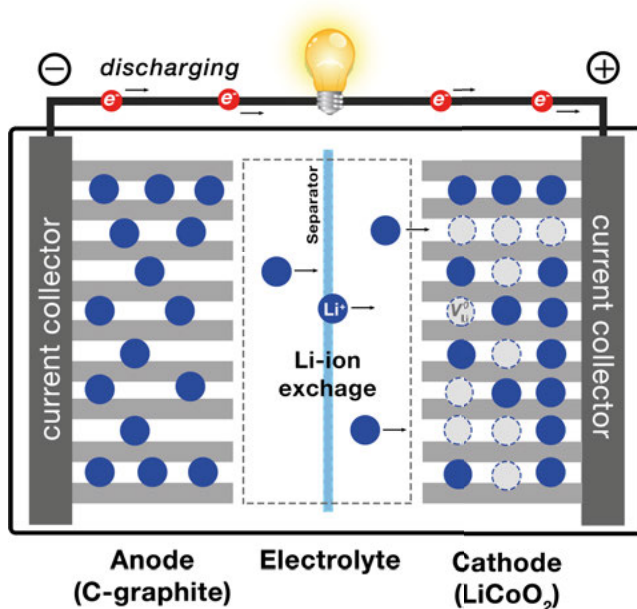
Figure 1.1. Schematic illustration of Li-ion battery based on $LiCoO_2$ cathode (positive) and graphite anode (negative) in discharging process.

higher strength of *X*-O covalency in these cathode materials leads to the lower *M* redox couple, resulting in a higher redox voltage and higher energy density. With the higher electronegativity of S, *sulfate-based polyanionic cathodes* have therefore been regarded as the highest voltage cathodes amongst other existing counterparts. This can be perceived form the following trend; Li_2FeSiO_4 (2.8 V) $<$ $LiFeBO_3$ (3.0 V) $<$ $LiFePO_4$ (3.4 V) $<$ $LiFeSO_4F$ (3.6-3.9 V) [10, 43].

Owing to the drastic increase in global Li consumption, questions and concerns about its limited supply have been raised. This can be clearly observed from 45% increment of Li price from 2002 to 2018, making it the most sought-after mineral on earth comparable to *white petroleum*. Sodium (Na) is an excellent replacement for Li due to the facts shown in Table 1.1, like Na is inexpensive and the sixth most abundant element in the earth's crust. Considering all the aforementioned reasons, iron-sulfate based cathode materials for sodium-ion batteries (SIBs) are one of the most promising candidates for the future of affordable and sustainable battery technology. Some of the sulfate-based polyanionic cathodes (also phosphate-based analogues) are shown along with their intercalation voltages and specific capacities in Fig.1.2. However, the scientific research regarding this cathode class are still limited these days. Even though Li and Na share similar alkali metal chemistries, cathodes for SIBs cannot be simply duplicated from those used in LIBs. Moreover, unlike other polyanions, the sulfate-based cathode is difficult to be synthesized

13
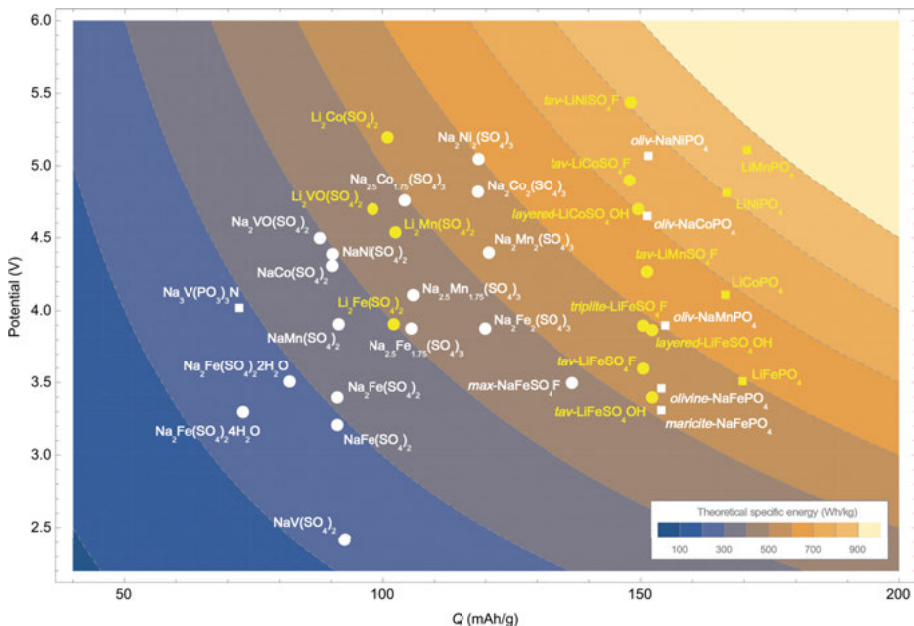
Figure 1.2. Average intercalation potential vs. specific capacity diagram for phosphate- and sulfate-based polyanionic cathodes evaluated using first-principles approaches. Shape and colour of marker points specify type of polyanionic cathodes (square: phosphate-based and circle: sulfate-based) and that of alkaline ions (yellow:Li and white:Na). Potentials for Li-ion and Na-ion cathodes are referenced to Li/Li^+ and Na/Na^+ redox potentials, respectively. The specific density is indicated by colours of each contour region as defined in scale bar. Reproduced from Ref.[20] with permission. Copyright 2018, IOP Publishing

due to (i) the inherent instability of SO_4 units at temperature above $400°C$ leading to the decomposition into SO_2 gas, and (ii) the hygroscopic nature of sulfates [10]. Therefore, the understanding behind the mechanism of sodium interactions with the host materials and the influences of synthesis conditions upon cathode properties are substantially needed to enhance in order to design high-performing sulfate-based cathodes.

1.2 Influence of crystal imperfections on battery performances

One of the crucial factors that influence chemical and physical behaviours in solids is the nature of crystal imperfections. The emergence of defects and impurities can affect materials, which can be both advantage or disadvantage from the application perspective. This could be either through extrinsic doping

Table 1.1. *The comparison between Na and Li metals.*

	Na	Li
Cation radius (Å)	1.06	0.76
Atomic weight (g/mol)	23	6.9
Standard potential (V)	-2.7	-3.0
Abundance in earth's crust (%)	2.3	0.002
Price ($/ton)	150	15,000

or intrinsic defects. Thus, a profound understanding of defect behaviors and mechanism is fundamentally essential for material designs and engineering.

Doping is one of the most promising techniques that have been utilized to manipulate material properties in modern material science and technology, such as well-known blue light emitting diodes (LED), displays, data storage, supercapacitor and battery [105]. As for battery-electrode materials, the doping effect of aliovalent cation substitutions (such as Zr and Nb) was initially studied in $LiFePO_4$ and was claimed to increase electronic conductivity drastically by 8 orders of magnitude at high temperature [22]. Several experiments opposed this claim and differently attributed such improvement to the presence of conductive carbon impurities [79]. The use of first principles methods comes into the picture when Islam *et al.* performed atomistic modelling simulation and revealed that the aliovalent doping was highly unfavorable in $LiFePO_4$, while divalent dopants for Fe (such as Mg, Mn and Co) were energetically preferable [51]. Some of the divalent substitutions were experimentally found to be effective for an enhanced electronic conductivity [42, 70].

In addition to doping, native defects often have a decisive impact on the material's performance. The types of native defects, both for Schottky and Frenkel defects, are defined as shown in Fig.1.3(a). The point defect prevailed mostly in the field of battery is the anti-site, which strongly deteriorates ionic conductivity and retention capacity by blocking the Li intercalation channels in the cathodes materials. A good example of such material with one-dimensional (1D) intercalation channels is olivine-type $LiFePO_4$ [23, 6], in which the presence of single Fe_{Li} will completely impede Li-ion migration along the entire channel as shown in Fig.1.3(b). Moreover, transition metal or alkaline ion vacancies can cause a reduced capacity, whereas oxygen vacancy may result in structural decomposition and inferior electrochemical behavior. Furthermore the native defects can also have an impact on electronic conduction in polyanionic cathodes, which generally proceeds through hopping of small polarons [47, 78, 122, 32]. Thus, an insight into the fundamental properties of native defects is ultimately required to achieve more suitable properties of materials. For example, understanding the correlation between experimental synthesis conditions and defect concentrations can enable the possibility to reduce the concentration of anti-site defect and phase impurities. However, studies on defects are still scarce for cathode materials, especially
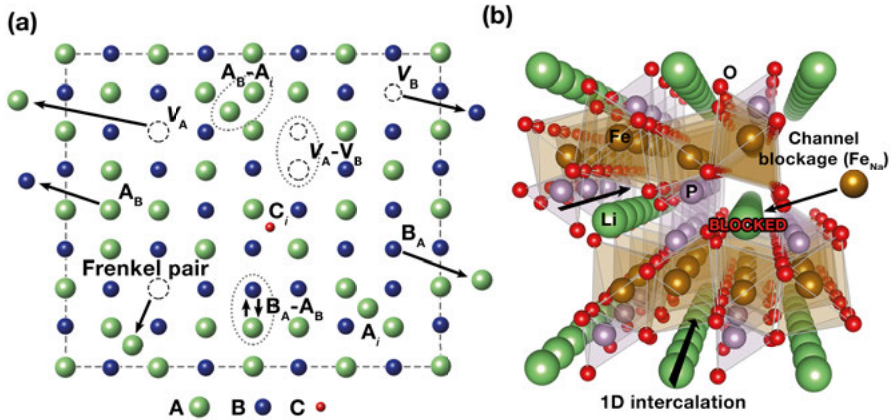
Figure 1.3. (a) Schematic illustration of defects in AB compound consisting of vacancy (V_A), interstitial (A_i), antisite (A_B), Frenkel pair, defect complex (shown in a dotted-circle) and C dopant. (b) Li-ion intercalation channels and Fe_{Na} antisite defect in olivine-type $LiFePO_4$.

for those in the newly sulfate-based family. In this regard, the present thesis will particularly focus on the investigation of influence by the native defects on electrochemical behavior, electron/ion transport and thermodynamics in sulfate-based polyanionic SIB cathodes.

Typically, the identification and characterization of defects are complex, indirect and usually requiring an ingenious combination of various experimental techniques [35, 107]. However, with the state-of-the-art computational methodology or the so-called *first principles*, it is possible to access the physical properties of materials theoretically. This approach has been rapidly developed and become a powerful tool, which does not only explain and complement experiments effectively but can also predict new materials and their properties.

1.3 Hybrid Supercapacitors as New generation Energy Storage Materials

Even though LIBs and SIBs show several advantages, they suffer from low power density. This is due to the slow processes of ionic diffusion and charge transfer, resulting in a lack of fast charging/discharging ability required in high-power applications. This bottleneck can be solved by another type of energy storage devices known as *supercapacitors* (SCs). It can provide a superior power density as compared to battier by virtue of the fast storage and delivery mechanisms based on a physical ion accumulation at the electrode/electrolyte interfaces [111]. However, as the energy retention solely depends on the ac-

tive surface area of electrodes, the corresponding specific energies of SCs are relatively lower as compared to the batteries.

In order to bridge the functionality between batteries and supercapacitors, the concept of hybrid supercapacitors (HSCs) has been intuitively emerged by combining a SC-type electrode and a battery-type electrode into a single device. This is feasible due to their similar configurations as depicted in Fig.1.4, where an activated carbon (AC) and NaMPO$_4$ are used as negative and positive electrodes separated by an electrolyte (e.g., NaOH aqueous electrolyte). During the charging process, there is negative charge accumulation on the surface of AC electrode that electrostatically attracts Na$^+$ solvated cations in the electrolyte, while simultaneously inducing the deposition of OH$^-$ solvated anions on NaMPO$_4$ positive electrodes. This leads to a fast charge storage process in the form of electrical double layer capacitance (EDLC). Moreover, as a SIB material, NaMPO$_4$ can store energy through: (i) redox pseudocapacitive behaviors, i.e., a reversible faradaic reaction and charge transfer, and also (ii) intercalation pseudocapacitive behavior, i.e., Na$^+$ ion deintercalation in this case, as demonstrated in Fig.1.4(a). Thus, the term *cathode* can be used to represent the positive electrode in HSCs. In the process of discharging, all the amounts of charges on the surface/bulk of negative electrodes are flowing to the positive electrode across an external circuit, whereas the Na$^+$ solvated ions diffuse through the electrolyte and intercalate back into the positive electrode as depicted in Fig.1.4(b). According to this design, the capacitance and energy energy in HSCs can be significantly improved but they come at the cost of reduced power density as compared to the EDLC-based SCs [124, 29, 27].

Several types of HSCs have been developed and some has reached the market in recent years. The pioneering prototype of HSCs is based on the combination of a positive activated carbon (AC) electrode with a negative Li$_4$Ti$_5$O$_{12}$ faradaic analogue in a non-aqueous electrolyte, which has been reported to provide a much improved voltage profile and 400-500% increment of energy density as compared to the nonaqueous EDLC technology [1]. Despite the remarkable properties of non-aqueous electrolyte, they suffer from several drawbacks, such as issues regarding safety and environmental damage due to the use of highly toxic and flammable solvents, and the high fabrication costs [17]. For these reasons, various attempts to use the aqueous electrolyte in HSCs have been explored by combining the capacitive AC electrode with faradaic positive electrodes which includes oxide and polyanionic compounds, such as MnO$_2$, NiO, Li$_2$Mn$_4$O$_9$ and LiTi$_2$(PO$_4$)$_2$ [110].

Even though the HSCs typically show significant improvement of both capacitance and energy density, a full utilization of overall energy density is difficult to be reached due to the slow redox reaction kinetics of battery-type electrodes. This hinders the energy storage performance of HSCs, especially during the fast charge-discharge processes. In order to overcome this shortcoming, it requires advanced strategies and architectures that can enhance the conduction properties of the battery-type electrodes. There are several tech-
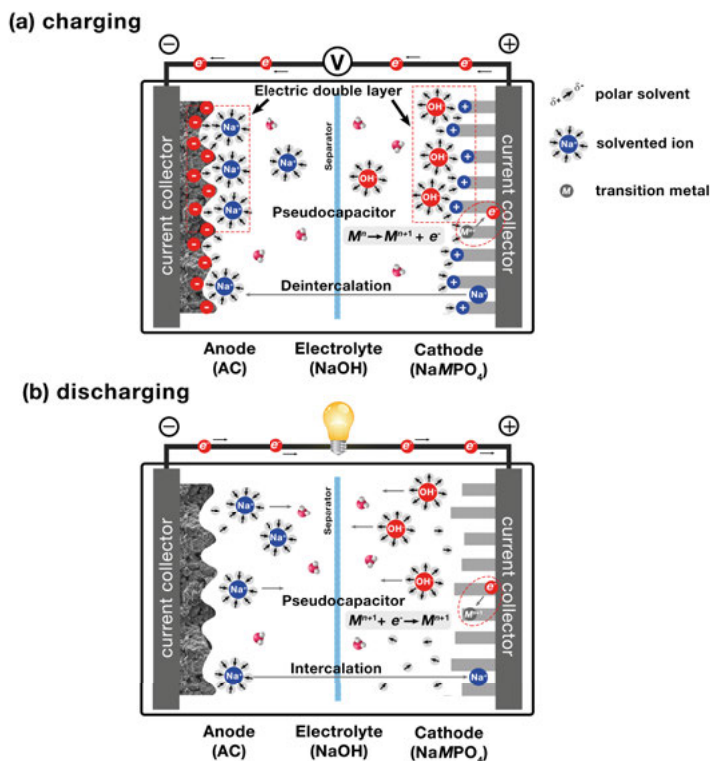
Figure 1.4. Schematic illustration of hybrid supercapacitor in (a) charging and (b) discharging processes.

niques that have been applied to attain this goal, for instance, by controlling the size and morphology of electroactive particles through carbon coating or metal doping [29]. Considering all these, the quest for novel energy storage materials both from experimental and theoretical perspectives are equally important. This can be observed through the novel explorations of several battery-type cathode materials in HSCs, including layered oxides, spinel oxide, olivine, NASICON and silicates [27], particularly those being used for Na-ion batteries. Therefore, the materials science community needs to work on enlarging the limited materials database for the HSC applications.

1.4 Thesis outline

Considering the aforementioned background, the prime objective of this thesis has been dedicated to use the density functional theory (DFT) to predict and further investigate the wide range of properties of cathode materials, such as structural, electronic, electrochemical, defect and kinetics, for SIBs and HSCs applications. The thesis is organised by six chapters (not including this chap-

ter). In Chapter 2, we provide a brief description of various methods proposed to solve many-body problems in quantum mechanics, while focusing on the DFT framework and the corresponding relevant theoretical methods.

The summary of results and discussions is sequentially provided in the next three Chapter according to type of cathode materials. Chapter 3 is primarily dedicated to a bi-hydrated sodium iron bisulfate or *kröhnkite*-type sulfate cathode ($Na_2Fe(SO_4) \cdot 2H_2O$). The major goal is to probe diffusion mechanisms of Na ions and the possibility of full-desodiation in this cathode. Moreover, as defects and small hole polarons play a vital role in these mechanisms, the investigations of defect thermodynamics and polaronic effect are also deliberately discussed in this chapter. In Chapter 4, we take a step forward to the polysulfate cathode, which delivers the highest redox potential among any Fe-based SIB cathodes, known as *alluaudite*-type sodium iron sulfate $Na_{2+2\delta}Fe_{2-\delta}(SO_4)_3$ [12]. Typically, this cathode shows the non-stoichiometry behavior, where there are partial Na substitutions for Fe sites as represented by δ in its chemical formula. Nevertheless, an influence of the non-stoichiometry is yet to be clarified till date. In this regard, we unveil the non-stoichiometric effects on the thermodynamics, defect nature, and voltage profiles for this class of cathode materials. In Chapter 5, we demonstrates the investigations of battery-type cathodes used in HSCs, namely the $NaMPO_4$ and $MMoO_4$ (where M denotes a transition metal), in the combination with experiments. The effect of transition metal substitution is given in terms of electronic structure, charge transfer, and phase stability, to support experimental findings and specify the charge storage mechanism in these two types of HSC cathodes. Finally, the conclusion are provided in the last chapter of the thesis.

2. Theoretical Methods

Density functional theory (DFT) is one of the most successful and power-ful computational method that is extensively used to solve puzzles of many-electron problems in physics, chemistry and materials science. With a long continuous development since 1970s, the DFT approach has undoubtedly demon-strated the reliability to effectively predict electronic structures and physical properties of materials at an affordable cost of computational demand. Thus, it has been considered as an essential tool determining the future of advanced materials science. Without it, the understanding and knowledge regarding a basic nature of materials would be difficult to achieve solely based on experi-mental strategies. This chapter is aimed at giving an overview of fundamental principles and methods applied to conduct all of the studies in this thesis. The first part describes the foundation of many-body problems in quantum me-chanics. Subsequently, we show a brief concept of DFT method along with all associated methods that help simplifying the many-electron problems. The re-maining parts provide the theoretical backgrounds of defect thermodynamics, ion diffusion and intercalation voltage approximations.

2.1 The Many-Body Problem

As generally known, the nature of matter is defined by the fundamental parti-cles, namely electrons and nuclei. A vast range of materials properties can be extracted if one can describe the complexity of interactions between a large number of these particles in matter, known as the *many-body problem* [76]. Based on quantum mechanics, it is theoretically possible to tackle such complexity in the form of electron wave functions by directly solving the Schrödinger equation,

$$\hat{H}\Psi = E\Psi, \tag{2.1}$$

where $\Psi = \Psi(\mathbf{r}_1, \mathbf{r}_2, \ldots, \mathbf{r}_N)$ is the wave function of an N-electron system and E is the energy eigenvalue of the Hamiltonian operator $\hat{H}$ with correspond-ing eigenvalues of a total energy E. In this case, the Hamiltonian operator is written according to the sum of kinetic and potential energies of interacting particles as follows,

$$\hat{H} = -\sum_i \frac{\hbar^2}{2m_e}\nabla_i^2 - \sum_I \frac{\hbar^2}{2M_I}\nabla_I^2 + \frac{1}{2}\sum_{I \neq J}\frac{Z_I Z_J e^2}{|\mathbf{R}_I - \mathbf{R}_J|} - \sum_{i,I}\frac{Z_I e^2}{|\mathbf{r}_i - \mathbf{R}_I|}$$

$$+ \frac{1}{2}\sum_{i \neq j}\frac{e^2}{|\mathbf{r}_i - \mathbf{r}_j|}, \tag{2.2}$$

where lower case and upper case subscripts denote electrons and nuclei with charge Z_I and mass M_I, and the coordinates of ith electron and I^{th} nuclei are denoted by $\mathbf{r}_i$ and $\mathbf{R}_I$, respectively. The first two terms are kinetic energy operators for nuclei and electrons. The remaining terms account for Coulombic couplings between nuclei-nuclei, nuclei-electron and electron-electron. respectively. Owing to a huge difference between m_e and M_I, the kinetic energy of the nuclei is much smaller that of the electrons as if the nuclei is relatively fixed among a number of the moving electrons, allowing for the decoupling of electron and nuclei kinetics.Thus the kinetic energy of nuclei can be neglected and the Coulomb potential between nuclei-nuclei is regarded as a constant to the total energy. This concept is known as the Born-Oppenheimer approximation [15] and leads to a purely electronic Hamiltonian as re-written below,

$$\hat{H} = \underbrace{-\sum_i \frac{\hbar^2}{2m_e}\nabla_i^2}_{\hat{T}_e} \underbrace{-\sum_{i,I}\frac{Z_I e^2}{|\mathbf{r}_i - \mathbf{R}_I|}}_{\hat{V}_{ext}} + \underbrace{\frac{1}{2}\sum_{i \neq j}\frac{e^2}{|\mathbf{r}_i - \mathbf{r}_j|}}_{\hat{V}_{ee}}, \tag{2.3}$$

where the second term in Eq.2.3 can be considered as a fixed potential external to electrons, denoted by $\hat{V}_{ext}$. Even with this approximation, it is still extremely difficult to find the many-body wavefunction due to the correlation of electrons. It means that the motion of electron i and its interactions with the fixed nuclei are influenced by the Coulomb repulsion from the other N-1 electrons in the N-electron system. To solve this problem, one alternative is to neglect the electron correlation and consider the many-body problem as an N-single electron problem. There are two basic independent-electron approaches known as Hartree (non-interacting) and Hartree-Fock approximations. They are both based on the assumption of uncorrelated electrons but the former does not obey the Pauli exclusion principle stating that electrons must be described by an anti-symmetric wavefunction. The Hartree-Fock (HF) method fulfills this property by defining the wavefunction in a Slater determinant (Ψ_{HF}) of single-electron wavefunctions $\psi_j(\mathbf{x}_j)$ as given below,

$$\Psi_{HF} = \frac{1}{\sqrt{N!}} \begin{vmatrix} \psi_1(\mathbf{x}_1) & \psi_2(\mathbf{x}_1) & \cdots & \psi_N(\mathbf{x}_1) \\ \psi_1(\mathbf{x}_2) & \psi_2(\mathbf{x}_2) & \cdots & \psi_N(\mathbf{x}_2) \\ \vdots & \vdots & \ddots & \vdots \\ \psi_1(\mathbf{x}_N) & \psi_2(\mathbf{x}_N) & \cdots & \psi_N(\mathbf{x}_N) \end{vmatrix}. \tag{2.4}$$

In the determinant, $\psi_j(\mathbf{x}_j)$ is a product of a function of the position $\psi(\mathbf{r}_j)$ and the spin variable $\varphi_i(\sigma_j)$. Based on this approximation, one can obtain the Hartree-Fock equation by using the variation principle to minimize the expectation value of the Hamiltonian in Eq.2.3 under the orthogonality constraints ($\langle \psi_i^\sigma | \psi_j^\sigma \rangle = \delta_{ij}$). The Hartree-Fock equation can be expressed as,

$$\left[-\frac{\hbar^2}{2m_e}\nabla_i^2 + V_{ext}(\mathbf{r}) + \sum_{j,\sigma_j} \int d\mathbf{r}' \psi_j^{\sigma_j*}(\mathbf{r}')\psi_j^{\sigma_j}(\mathbf{r}')\frac{e^2}{|\mathbf{r}-\mathbf{r}'|} \right] \psi_i^\sigma(\mathbf{r})$$

$$-\sum_j \int d\mathbf{r}' \psi_j^{\sigma*}(\mathbf{r}')\psi_i^\sigma(\mathbf{r}')\frac{e^2}{|\mathbf{r}-\mathbf{r}'|}\psi_j^\sigma(\mathbf{r}) = \varepsilon_i^\sigma \psi_i^\sigma(\mathbf{r}). \quad (2.5)$$

While the third term in the square bracket is the Coulomb interaction of an electron i with the average charge distribution of other electrons $|\psi_j^{\sigma_j}(\mathbf{r}')|^2$, the last term is the *exchange term* which is more complicated to solve due to the exchange between ψ_i^α and ψ_j^α. By using the HF approximation, the ground state wavefunction is obtained through iterative procedures of the self-consistent field approach (SCF)[1]. However, because this method scales exponentially with N, it highly suffers from computational difficulties hindering the study of many electron systems [59].

To overcome the shortcomings of this approach, a way to replace $4N$-variable wavefunction (three spatial and one spin variables for each of N electrons) with a simpler 3-variable function of the electron density was proposed in the remarkable theorems, known as the density functional theory.

However, in materials, it is almost impossible to solve the Schrödinger equation because of the complicated electron-electron interactions. The complicated problem can be simplified to a solvable problem by using density functional theory (DFT). For a long time, DFT, the most popular computational method, has been used to study physical properties of materials because this method frequently gives us reliable results when comparing with experimental results. Therefore, in this thesis, DFT has been performed through the Vienna Ab-initio simulation package (VASP) code.

2.2 Density functional theory

Density functional theory was proposed to overcome the shortcomings of the HF approach by simplifying a many-body problem into an effective single-particle problem that also includes the effects of correlations among particles. Instead of dealing with the $4N$-variable wavefunction (three spatial and one spin variables for each of N electrons), the ground state is uniquely described

---

[1]Self-consistency is achieved when the energy difference between two consecutive iterations is lower than a given convergence accuracy.

on the basis of a simpler 3-variable function of the electron density ($\rho[\mathbf{r}]$). This formulation of DFT was first proved to be valid in any interacting particle system under the effect of $V_{ext}(\mathbf{r})$ by Hohenberg and Kohn (HK) [48]. They proposed the core foundation for DFT consisting of two remarkable theorems as described below[2]

Theorem I: For any system of interacting particles in an external potential $V_{ext}(\mathbf{r})$, the potential is determined uniquely, except for a constant, by the ground state particle density $\rho_0(\mathbf{r})$.

Theorem II: A universal functional for the energy $E[\rho]$ in terms of the density $\rho(\mathbf{r})$ can be defined, valid for any external potential $V_{ext}(\mathbf{r}$. For any particular $V_{ext}(\mathbf{r})$, the exact ground state energy of the system is the global minimum value of this functional, and the density $\rho(\mathbf{r})$ that minimizes the functional is the exact ground state density $\rho_0(\mathbf{r})$.

The first theorem means that the electron density is a unique function determining the $V_{ext}(\mathbf{r})$ and other properties of the system similar to the wavefunction, whereas the second theorem says that the total energy can be viewed as a function of the electron density,

$$E_{HK}[\rho] = \underbrace{T[\rho] + E_{ee}[\rho]}_{F_{HK}[\rho]} + \underbrace{\int \rho(\mathbf{r})V_{ext}(\mathbf{r})d\mathbf{r}}_{E_{ext}[\rho]}, \qquad (2.6)$$

where the $E_{ext}[\rho]$ is the interaction energy between electron and the external potential of the nuclei while all internal energies, kinetic and potential, of the interacting particle system are included in the functional $F_{HK}[\rho]$, which is universal since it is the same for all electron systems and independent of the external potential. The HK functional is equivalent to the expectation value of the Hamiltonian $\hat{H}$ in the unique ground state $\rho_0(\mathbf{r})$ (with the wavefunction ψ_0). When considering a different density $\rho(\mathbf{r})$, the total energy of this state must be greater than E_0 [76],

$$E_0[\rho_0(\mathbf{r})] = \langle \psi_0|\hat{H}|\psi_0 \rangle \leq \langle \psi|\hat{H}|\psi \rangle = E[\rho(\mathbf{r})]. \qquad (2.7)$$

Therefore, one will obtain the exact ground state density $\rho_0(\mathbf{r})$ and energy $E_0(\mathbf{r})$ when the total energy of the system is minimized.

2.2.1 The Kohn-Sham ansatz

Based on the two HK theorems, it was proved that the electron density can be a basic variable to determine the ground state wavefunction of many-particle systems, allowing the formulation of energy functional via the use of the variational principle. Kohn and Sham proposed a simplified concept to deal with

---

[2]These theorems are quoted from ref.[76], p.122

the difficult interacting systems by replacing them with an auxiliary system of non-interacting particles with the same electron density [60].

As mentioned in the previous section, the electron-electron interaction $E_{ee}[\rho]$ and the kinetic energy of the correlated electrons $T[\rho]$ cannot be explicitly expressed due to the electron correlation in the interacting particle systems. The $F_{HK}[\rho]$ in Eq.2.6 can be written by separating the $E_{ee}[\rho]$ term into classical and non-classical terms ($E_{cl}[\rho(\mathbf{r})]$ and $E_{ncl}[\rho(\mathbf{r})]$), while the $T[\rho]$ is replaced by the kinetics of the non-interacting system $T_s[\rho]$. The difference between the interacting and non-interacting systems (i.e. $E_{ncl}[\rho(\mathbf{r})]$ and $T[\rho] - T_s[\rho]$) is specifically grouped in the *exchange-correlation functional* (E_{xc}). Therefore, $F_{HK}[\rho]$ is presented as,

$$F_{HK}[\rho(\mathbf{r})] = T[\rho(\mathbf{r})] + E_{cl}[\rho(\mathbf{r})] + E_{ncl}[\rho(\mathbf{r})] \qquad (2.8)$$
$$= T_s[\rho(\mathbf{r})] + E_{cl}[\rho(\mathbf{r})] + E_{xc}[\rho(\mathbf{r})], \qquad (2.9)$$

The $E_{cl}[\rho(\mathbf{r})]$ is defined by the Coulomb self-interacting energy of the electron density (or the Hartree energy) and the $T_s[\rho(\mathbf{r})]$ is described with respect to single-electron KS orbitals ($\phi_i(\mathbf{r})$). These two functionals are explicitly obtained from the following expressions,

$$E_{cl}[\rho(\mathbf{r})] = \frac{1}{2} \int \frac{\rho(\mathbf{r})\rho(\mathbf{r}')}{|\mathbf{r} - \mathbf{r}'|} d\mathbf{r} d\mathbf{r}'. \qquad (2.10)$$

$$T_s[\rho(\mathbf{r})] = -\frac{\hbar^2}{2m_e} \sum_{i=1}^{N} \langle \phi_i | \nabla_i^2 | \phi_i \rangle, \qquad (2.11)$$

In this regard, the energy functional based on the KS formalism can be re-written in the form,

$$E_{KS}[\rho(\mathbf{r})] = T_s[\rho(\mathbf{r})] + E_{cl}[\rho(\mathbf{r})] + E_{ext}[\rho(\mathbf{r})] + E_{xc}[\rho(\mathbf{r})], \qquad (2.12)$$

where the $E_{xc}[\rho(\mathbf{r})]$ is the only component not being in the exact form. However, this unknown term can be determined using appropriate approximations, which will be explained in the following section.

Ultilizing the HK theorem, the ground state energy for the KS auxiliary system can be obtained by minimizing the energy functional with respect to the $\phi_i^*(\mathbf{r})$ orbitals. As the last three terms in Eq.2.12 are functions of the density, chain rule for functional derivatives is employed. Thus, one obtains the variation equation as shown below,

$$\frac{\delta E_{KS}[\rho(\mathbf{r})]}{\delta \phi_i^*(\mathbf{r})} = \frac{\delta T_s[\phi_i(\mathbf{r})]}{\delta \phi_i^*(\mathbf{r})} + \left[\frac{\delta E_{ext}[\rho(\mathbf{r})]}{\delta \rho(\mathbf{r})} + \frac{\delta E_{cl}[\rho(\mathbf{r})]}{\delta \rho(\mathbf{r})} + \frac{\delta E_{xc}[\rho(\mathbf{r})]}{\delta \rho(\mathbf{r})} \right] \frac{\delta \rho(\mathbf{r})}{\delta \phi_i^*(\mathbf{r})}$$
$$= -\sum_i \frac{\hbar^2}{2m_e} \nabla_i^2 \phi_i(\mathbf{r}) + \left[\hat{V}_{ext}(\mathbf{r}) + \hat{V}_{cl}(\mathbf{r}) + \hat{V}_{xc}(\mathbf{r}) \right] \phi_i(\mathbf{r}), \quad (2.13)$$

With the use of Lagrange multipliers subject to the orthonormalization constraints, its derivative is stationery and defined as

$$\frac{\delta}{\delta \phi_i^*(\mathbf{r})} \left[E_{KS}[\rho(\mathbf{r})] - \sum_{i,j} \varepsilon_{ij}(\langle \phi_i | \phi_j \rangle - \delta_{ij}) \right] = 0, \qquad (2.14)$$

where ε_{ij} are the Lagrange multipliers and δ_{ij} is the Kronecker delta. Taking the derivative of the energy functional, one can obtain the Schrödinger-like equation for non-interacting particles within the effective potential $V_{eff}(\mathbf{r})$, or the so-called *Kohn-Sham equation*,

$$\left[-\sum_i \frac{\hbar^2}{2m_e} \nabla_i^2 + \underbrace{\left[\hat{V}_{ext}(\mathbf{r}) + \hat{V}_{cl}(\mathbf{r}) + \hat{V}_{xc}(\mathbf{r}) \right]}_{V_{eff}(\mathbf{r})} \right] \phi_i(\mathbf{r}) = \varepsilon_i \phi_i(\mathbf{r}). \qquad (2.15)$$

If the exact $V_{xc}(\mathbf{r})$ is known, one can directly solve the KS equation to determine the ground state wavefunction and energy of the interacting system by using the SCF procedures.

The first step in the SCF iteration is a selection of guessed initial density. Then, the KS Hamiltonian, including the effective potential, is constructed and operated on the guessed density, giving a new set of KS wavefunctions. From the obtained wavefunctions, a new charge density is determined and subsequently refined by mixing with the previous density. If the energy difference between this mixed density and the previous analogue does not satisfy expected tolerance (energy convergence criteria), the aforementioned processes will be iteratively repeated based on this mixed density. Once the tolerance of energy difference is achieved, one obtains the ground state wavefunction with respect to the particular nuclear configuration. Note that the force convergence criteria is also included in the SCF procedures but the details about force theorem will be discussed later.

2.3 Exchange-correlation functionals

In the KS method, the exchange-correlation functional $E_{xc}(\mathbf{r})$ is introduced by integrating all unknown terms accounting for the difference between the interacting and non-interacting systems. Owing to the complexity of electron correlation in the many-body system, this term cannot be expressed in an exact form. However, it can be determined by using several approximations, which will be given in this section.

2.3.1 Local density approximation

Local density approximation (LDA) is the simplest approximation proposed by Kohn and Sham [60]. It was assumed that electrons in a solid can be generally considered as an uniform electron gas (UEG), meaning that the electron densities at any point in space are constant ($\rho(\mathbf{r}) = \rho_0$). Therefore, the exchange-correlation functional within LDA method merely depends on the electronic density and can be written as

$$E_{xc}^{LDA}[\rho(\mathbf{r})] = \int \rho(\mathbf{r})\varepsilon_{xc}^{UEG}[\rho]d\mathbf{r} \qquad (2.16)$$

where $\varepsilon_{xc}^{UEG}(\rho)$ is the exchange and correlation energy per particle of the uniform electron gas that can be usefully separated into the exchange energy $\varepsilon_x^{UEG}(\rho)$ and the correlation energy $\varepsilon_c^{UEG}(\rho)$:

$$\varepsilon_{xc}^{UEG}[\rho] = \varepsilon_x^{UEG}[\rho] + \varepsilon_c^{UEG}[\rho] \qquad (2.17)$$

The exact form of $\varepsilon_x(\rho)$ is obtained from the expression derived by Dirac [28] as

$$\varepsilon_x^{UEG}(\rho) = -\frac{3}{4}\left(\frac{3}{\pi}\right)^{1/3}\int \rho(\mathbf{r})^{4/3}d\mathbf{r} = -\frac{3}{4}\left(\frac{3\rho_0}{\pi}\right)^{1/3}, \qquad (2.18)$$

whereas the $\varepsilon_c^{UEG}(\rho)$ can be determined from the interpolation between the high- and low-density regimes. Among several interpolation schemes, Perdew-Zunger (PZ) [92] is the most common in which the $\varepsilon_c^{UEG}(\rho)$ is parametrized based upon the quantum Monte Carlo simulations of Ceperly and Alder [19] for UEG at various densities. The LDA functional has been proved to be a successful method to simulate various materials properties in a wide range of systems, in particular those resembling the UEG model (i.e., valence electrons in metals). However, it usually leads to the overbinding problems when dealing with a highly inhomogeneous systems, such as atoms and molecules.

2.3.2 Generalized gradient approximation

To overcome the deficiency in LDA functional, a remarkable improvement to approximate the exchange-correlation energy for inhomogeneous systems was made in the form of the generalized gradient approximation (GGA) [97]. In this method, the gradient of the electron density $\nabla \rho(\mathbf{r})$ is added to incorporate the effect of inhomogeneities. Owing to the dependence of local density and the spatial variation of the density, it is regarded as a semi-local method in which the exchange-correlation functional can be expressed as,

$$E_{xc}^{GGA}[\rho(\mathbf{r})] = \int \rho(\mathbf{r})\varepsilon_{xc}[\rho, \nabla\rho]d\mathbf{r} \tag{2.19}$$

$$= \int \rho(\mathbf{r})\varepsilon_x^{UEG}[\rho] \cdot F_{xc}[\rho, \nabla\rho]d\mathbf{r} \tag{2.20}$$

where F_{xc} is an enhancement factor containing a dimensionless function of ρ and $\nabla\rho$ [76]. It is separated into two parts, namely exchange (F_x) and correlation factors (F_c), as similar as in the E_{xc} functional.

The different flavours of GGA functionals comes from the F_x which is defined in terms of dimensionless reduced density gradient (s) of m-th order [93]. The expression for s_m and its first gradient (s_1) can be written as,

$$s_m = \frac{|\nabla^m\rho|}{2^m(3\pi^2)^{m/3}(\rho)^{1+m/3}} \text{ and } s_1 = \frac{|\nabla r_s|}{2(2\pi/3)^{1/3}r_s}, \tag{2.21}$$

where r_s is the local Wigner-Seitz radius ($r_s = (4\pi\rho/3)^{-1/3}$). The expansion of $F_x(\rho, s)$ has been proposed in various forms (with $s = s_1$), for example, the most widely used forms are those proposed by Becke (B88)[13], Perdew-Wang (PW91) [97], and Perdew, Burke and Ernzerhof (PBE) [94, 95]. This leads to the different behavior of functionals. While $F_x(\rho, s)$ is invariant (equivalent to 1 as $s = 0$) for the UEG model in LDA functional, most GGA-type functionals have a similar $F_x(\rho, s)$ in the region of small s but it changes differently the region of large density gradient ($s > 3$). In this thesis, we mainly employ the xc-approximations associated with the PBE functional in which $F_x(\rho, s)$ becomes constant at large density gradient. Regarding $F_c(\rho, s)$, it is commonly treated using the Lee-Yang-Parr (LYP) [67] correlation functional.

As a result of the inclusion of the density gradient, the GGA functionals can give an improved description of electron exchange and correlations that corrects the LDA overbinding, in particular for the systems with fluctuating electron density. However, it cannot be clearly stated that GGAs will always provide more accurate results consistent to experimental analogues when compared with the LDA functional. This situation can occur due to the self-interaction error in both LDA and GGA functionals as well as the absence of van der Waals interaction.

Straightforwardly, the self-interaction error originates from the unphysical interaction of electrons with itself in the Hartree term E_{cl}, causing the excessive delocalization of electrons in both solids and molecules. The most obvious deficiency is the underestimated band gap in LDA and GGA functionals where the localization of valence electrons is too weak and, hence, the energy level representing the valence band maximum is excessively high. This problem leads to a wrong prediction of materials behavior in narrow-gap semiconductors and Mott insulators, for which both LDA and GGA show a metallic ground state instead [24]. Moreover, it can become more severe in

the systems with strong correlated and highly localized electrons, for example, transition metal oxides and rare earth compounds [76]. In the following sections, we will present the methods used to handle these issues.

2.3.3 DFT+U approach

The concept of DFT+U approach is to rationalize the correlated electron systems by integrating the Hubbard model [50] in the generic DFT formalism. In this functional, the Hubbard Hamiltonian is applied to selectively correct the strongly correlated electronic states, such as d or f orbitals, while the other states are treated using the standard LDA or GGA functional [24, 76]. The general formulation of energy functional within DFT+U can be expressed as

$$E^{DFT+U}[\rho] = E^{DFT}[\rho] + E_{Hub}[n^{\sigma}_{mm'}] - E_{dc}[n^{\sigma}_{mm'}], \qquad (2.22)$$

where $E^{DFT}[\rho]$ is the energy functional based on KS method, $E_{Hub}[n_{mm'}]^{\sigma}$ is the Hubbard energy correction for localized state, and $E_{dc}[n_{mm'}]^{\sigma}$ is a double counting correction assigned to remove contribution of strongly localized states included in the $E^{DFT}[\rho]$. Both E_{Hub} and E_{dc} are functions of occupation numbers ($n^{\sigma}_{mm'}$) defined by projections of occupied KS orbitals on the localized states.

There are different formulations implemented in DFT+U functional, such as the rotationally-invariant formulation proposed by Lichtenstein et al. [68]. In this thesis, we employ a simplified formulation proposed by Dudarev et al. [30], where the orbital-dependent interactions are replaced by a spherical average while still giving similar results as the fully rotationally invariant one. This allows the use of an effective U parameter (U_{eff}) accounting for the deduction of the Hubbard Coulomb repulsion U with the Hund exchange interaction J (U_{eff} = U - J). The energy functional can be modified as,

$$E^{DFT+U}[\rho] = E^{DFT}[\rho] + \frac{U_{eff}}{2} \sum_{\sigma} Tr[n^{\sigma}(1-n^{\sigma})]. \qquad (2.23)$$

This functional can effectively solve the deficiencies in the standard approximations at a reasonable computational cost. However, as the correction can be controlled by the U_{eff} parameter specified in a practical calculation, it rises up a tricky question of how to determine an appropriate U_{eff} value. Theoretically, this parameter can be estimated using linear response theory [25] or piecewise linearity [33]. One way commonly used is to tune it as a semi-empirical parameter by reaching agreement with a certain properties measured in experiments and then specifically use the suitable value to simulate other properties of systems.

2.3.4 Hybrid functionals

Since each approximation differently has its own strengths and drawbacks, a remarkable strategy to integrate the exchange correlation energy based on two different methods emerged, called *hybrid functionals*. As mentioned in the previous section, the GGA is a powerful functional that gives good prediction at an affordable cost of computational resources, however, it suffers from the self-interaction error. On the other side, this unphysical interaction is completely cancelled out in the exact exchange energy of the HF approach, however, it excludes the electron correlation and requires highly computational resources. According to these facts, it led to the construction of the hybrid functionals with a combination of the E_{xc} within the standard level of xc-functional with the exact E_x in the HF approach.

Till now, several formulations have been proposed to construct the hybrid functional, such as B3LYP [102], PBE0 [96], and Heyd-Scuseria-Ernzerhof (HSE) functionals [45, 46]. As a chosen hybrid functional in some part of this thesis, the HSE functional is written in the following form,

$$E_{xc}^{HSE} = \alpha E_x^{HF,SR}(\omega) + (1-\alpha)E_x^{PBE,SR}(\omega) + E_x^{PBE,LR}(\omega) + E_c^{PBE}, \quad (2.24)$$

where SR and LR stand for the short-range and long-range components, respectively. The α is a mixing parameter and ω is a screening parameter controlling the short-rangeness of the exchange interaction. Note that $\alpha = 0.25$ and $\omega = 0.2$ Å^{-1} (referred as HSE06) are standard values that usually give good results for the prediction of materials properties.

2.4 Computational methods

2.4.1 Plane wave basis sets and Bloch's theorem

Even though the DFT methods pave the way to solve the many-interacting electron system, it is still too difficult to handle an infinite number of electrons moving in the static potential created by an infinite number of ions [57]. This leads to an infinite expansion of wavefunctions over an entire space in the crystalline solid system, which requires an immense number of basis sets. However, due to the periodicity of the crystal, it is possible to represent these wavefunctions based on the plane wave basis set with a periodic function according to Bloch's theorem [76, 57]. Using this theorem, the electronic wavefunction at the i-th band index is expressed as a product of a cell periodic term (the first term) and a wavelike term (the second term) as shown below,

$$\psi_{i,\mathbf{k}}(\mathbf{r}) = u_{i,\mathbf{k}}(\mathbf{r})e^{(i\mathbf{k}\cdot\mathbf{r})}, \quad (2.25)$$

The $\mathbf{k}$ denotes a reciprocal vector of a Bravais lattice in the first Brillouin zone (in k-space) and $u_{i,\mathbf{k}}(\mathbf{r})$ is the periodic function of the crystal lattice, i.e, $u_{i,\mathbf{k}}(\mathbf{r})$

$= u_{i,\mathbf{k}}(\mathbf{r} + \mathbf{T})$ for all lattice vectors $\mathbf{T}$. The $u_{\mathbf{k}}(\mathbf{r})$ can be expanded in Fourier series as shown below,

$$u_{i,\mathbf{k}}(\mathbf{r}) = \sum_{\mathbf{G}} c_{i,\mathbf{G}} e^{(i\mathbf{G}\cdot\mathbf{r})} \qquad (2.26)$$

where $c_{i,\mathbf{G}}$ are plane wave expansion coefficients and $\mathbf{G}$ represent reciprocal lattice vectors that satisfy the condition of $\mathbf{G}\cdot\mathbf{T} = 2\pi m$ (m is an integer). With Eqs.2.25 and Eq.2.26, we can thus write a single particle KS orbital as a finite sum of plane waves,

$$\psi_{i,\mathbf{k}}(\mathbf{r}) = \frac{1}{\sqrt{\Omega}} \sum_{\mathbf{G}} c_{i,(\mathbf{k}+\mathbf{G})} e^{(i(\mathbf{k}+\mathbf{G})\cdot\mathbf{r})}. \qquad (2.27)$$

This seems to create another problem, i.e., an infinite number of reciprocal space vectors within the first Brillouin zone (termed as k-points). However, it is not necessary to consider all of these k-points as the wavefunctions is nearly identical for the k values that are sufficiently close. Thus, it is possible to sample a finite number of discrete k-points that efficiently describes an entire k-space. There are several k-point sampling methods, such as the most commonly used one developed by Monkhorst and Pack [85]. In practice, the sufficiently high number of k-points can be determined from the convergence in total energy of the system. With the converged k-points, one can thus calculate the ground state of electronic wavefunctions at reasonable computing cost.

When putting Eq.2.27 into the KS equation (Eq.2.15), we obtain the KS equation in the plane wave form,

$$\sum_{\mathbf{G}'} \left[\frac{\hbar^2}{2m_e} |\mathbf{k}+\mathbf{G}|^2 \delta_{\mathbf{G}\mathbf{G}'} + V_{eff}(\mathbf{G}-\mathbf{G}') \right] c_{i,(\mathbf{k}+\mathbf{G}')} = \varepsilon_i c_{i,(\mathbf{k}+\mathbf{G})}. \qquad (2.28)$$

While the reciprocal space representation of the kinetic energy is diagonal, the potential energy is expressed in terms of Fourier components. This equation can be solved by diagonalizing the Hamiltonian matrix $\hat{H}_{\mathbf{k}+\mathbf{G},\mathbf{k}+\mathbf{G}'}$ shown in the bracket [76]. Although the sum over $\mathbf{G}$ vectors is infinite, the plane wave expansion can be truncated at a kinetic energy cut-off (E_{cut}) in order to achieve a finite basis set . The E_{cut} is defined as

$$\frac{\hbar^2}{2m_e} |\mathbf{k}+\mathbf{G}|^2 \leq E_{cut}. \qquad (2.29)$$

The value of required E_{cut} will be extremely large for an all-electron calculation including both valence and core electrons. This led to the development of a remarkable computational technique used in ab-initio calculations, which will be discussed in the next section.

2.4.2 Projector-augmented wave method

Based on the unique characteristics of wavefunctions, electrons near the nuclei is undergoing the influence of a strong Coulomb interaction. This leads to highly rapid oscillations of the wavefunction in the nuclear region which requires an extremely large number of plane waves to properly represent its description. Outside such region, the wavefunction is varying slowly due to the screening effect. These two regions are categorized as *core* and *valence* that are separated at a certain cutoff radius (r_c). The core electrons are tightly bound in the vicinity of the nucleus (in closed shells) but valence electrons are outside that region and play a key role in most of the physical properties. Therefore, this leads to a concept of *pseudopotential* approximation in which electrons in these two regions can be treated separately to reduce the number of required plane waves. Several pseudopotential methods have been developed, such as Norm-conserving approach of Kleinman and Bylander [58] and Ultrasoft approach of Vanderbilt [108].

In this thesis, we use the Vienna Ab initio Simulation Package (VASP) [64, 63, 62] implementing the plane wave basis within the Projector-augmented wave (PAW) [14], which is one of the most efficient methods for DFT calculations. In the PAW method, an all-electron single particle wavefunction $|\Psi\rangle$ is mapped into a smooth auxiliary wavefunction, which is more computationally convenient, called pseudo wavefunction $|\tilde{\Psi}\rangle$. This is done by using a linear transformation $\mathscr{T}$ such that $|\Psi\rangle = \mathscr{T}|\tilde{\Psi}\rangle$. The linear transformation $\mathscr{T}$ is expressed as,

$$\mathscr{T} = \hat{1} + \sum_R \mathscr{T}_R \tag{2.30}$$

where each $\mathscr{T}_R$ acts only in an augmentation region, Ω_R enclosing the core region. Thus, the all-electron (AE) and pseudo (PS) wavefunctions are identical outside the Ω_R region.

To construct $\mathscr{T}$, the $\mathscr{T}_R$ operators are defined as,

$$|\phi_i\rangle = (\hat{1} + \mathscr{T}_R)|\tilde{\phi}_i\rangle, \tag{2.31}$$

where $|\phi_i\rangle$ and $|\tilde{\phi}_i\rangle$ are AE and PS partial waves, respectively. The index i denotes the angular and magnetic quantum numbers lm. The $|\phi_i\rangle$ is the solution of the radial Schrödinger equation for the isolated atom and $|\tilde{\phi}_i\rangle$ can be directly obtained from the $|\phi_i\rangle$ outside the Ω_R sphere. As the partial wave should be orthogonal to the core states, the wavefunction can be expanded as a linear combination of partial wave basis sets,

$$|\Psi\rangle = \sum_i c_i |\phi_i\rangle; \text{ inside } \Omega_R. \tag{2.32}$$

Thus, these AE partial waves can transformed into the corresponding PS partial waves by the $\mathscr{T}$ operator such that $|\phi_i\rangle = (1 + \mathscr{T}_R)|\tilde{\phi}_i\rangle$. The $\mathscr{T}_R$ can be then obtained by the difference between AE and PS partial waves,

$$\mathscr{T}_R|\tilde{\phi}_i\rangle = |\phi_i\rangle - |\tilde{\phi}_i\rangle. \tag{2.33}$$

As the $\mathscr{T}$ is linear, the coefficients c_i can be written as an inner product with a set of projector functions $|p_i\rangle$: $c_i = \langle p_i|\Psi\rangle$ that fulfills the completeness relation $\sum_i |\tilde{\phi}_i\rangle\langle\tilde{p}_i| = 1$ and the orthogonality criterion $|\tilde{\phi}_i\rangle\langle\tilde{p}_j| = \delta_{ij}$. Thus, we obtain

$$|\tilde{\Psi}\rangle = \sum_i |\tilde{\phi}_i\rangle\langle\tilde{p}_i|\tilde{\Psi}\rangle. \tag{2.34}$$

By applying $\mathscr{T}_R$ in the above equation, the transformation of the AE wavefunction into the PS wavefunction can be written as

$$|\Psi\rangle = |\tilde{\Psi}\rangle + \sum_i (|\phi_i\rangle - |\tilde{\phi}_i\rangle)\langle\tilde{p}_i|\tilde{\Psi}\rangle, \tag{2.35}$$

$$= |\tilde{\Psi}\rangle + \underbrace{\sum_i (|\phi_i\rangle\langle\tilde{p}_i|\tilde{\Psi}\rangle}_{\text{AE onsite}} - \underbrace{\sum_i |\tilde{\phi}_i\rangle\langle\tilde{p}_i|\tilde{\Psi}\rangle}_{\text{PS onsite}}, \tag{2.36}$$

where the second and third terms represent AE and PS onsite contributions within the Ω_R region, and the exact form of $\mathscr{T}$ is then given by

$$\mathscr{T} = \hat{1} + \sum_i (|\phi_i\rangle - |\tilde{\phi}_i\rangle)\langle\tilde{p}_i|. \tag{2.37}$$

Based on this transformation, one can write the KS equation for PS wavefunctions as shown below,

$$(\tilde{H} - \varepsilon_i \tilde{O})|\tilde{\psi}_i\rangle = 0, \tag{2.38}$$

where $\tilde{H} = \mathscr{T}^\top H \mathscr{T}$ and $\tilde{O} = \mathscr{T}^\top \mathscr{T}$. Therefore, it is shown that the PAW method is an efficient method that can replace the AE wavefunctions with the PS wavefunctions, leading to the reduction of the computational cost to an affordable level. This method significantly facilitates further calculations for a wide range of quantities, such as charge density, total energy and forces.

2.5 Force theorem

The crucial criterion to justify the equilibrium of the crystal structure is the force acting upon each atom in the system. The ground state structure is achieved when the total interatomic force reaches zero in the process of geometry optimization. Typically, the acceptable tolerance for the residual force

is at least $\sim 10^{-2}$ eV/Å. The force acting on the I-th atom at position R_I can be evaluated from

$$F_I = -\nabla_{R_I} E, \qquad (2.39)$$

where E is the total energy of the system subject to the Hamiltonian $\hat{H}$ with an eigenfunction Ψ, expressed as

$$E = \frac{\langle \Psi | \hat{H} | \Psi \rangle}{\langle \Psi | \Psi \rangle}. \qquad (2.40)$$

On substituting Eq.2.40 into Eq.2.39, we obtain

$$
\begin{aligned}
F_I &= -\left\langle \frac{\partial \Psi}{\partial R_I} \middle| \hat{H} \middle| \Psi \right\rangle - \left\langle \Psi \middle| \frac{\partial \hat{H}}{\partial R_I} \middle| \Psi \right\rangle - \left\langle \Psi \middle| \hat{H} \middle| \frac{\partial \Psi}{\partial R_I} \right\rangle \\
&= -E \frac{\partial}{\partial R_I} \langle \Psi | \Psi \rangle - \left\langle \Psi \middle| \frac{\partial \hat{H}}{\partial R_I} \middle| \Psi \right\rangle \\
&= -\left\langle \Psi \middle| \frac{\partial \hat{H}}{\partial R_I} \middle| \Psi \right\rangle. \qquad (2.41)
\end{aligned}
$$

The above equation corresponds to the Hellmann-Feynman theorem [34], showing that the derivative of the total energy with respect to any parameter is equivalent to the expectation value of the Hamiltonian's derivative with respect to that same parameter. Thus, this enables the determination of the interatomic force in many-body systems on the basis of the KS wavefunctions, making the ground state geometry optimization possible.

2.6 Nudged elastic band method

In order to investigate the intercalation process in cathode materials, it is important to determine the migration energy of alkaline ions. This can be achieved by using the Nudged Elastic Band (NEB) [55] which is robust technique for finding saddle points and minimum energy paths (MEP) between two local minima on a potential energy surface. The first step is to define the set of $N+1$ images, which is denoted by $[r_0, r_1, r_2, \ldots , r_N]$. The end point, r_0 and r_N, are fixed and considered as the energy minima at initial and final states along MEP, whereas the rest of the images are adjusted by the optimization algorithm. To prevent each images moving out from the interpolation pathway, each image is assumed to be connected through a spring with k spring constant. Thus, the total force acting on each image is the sum of the spring force along the local tangent and the true force perpendicular to the local tangent as expressed below,

$$F_i = F_i^s|_{||} - \nabla E(r_i)|_\perp, \tag{2.42}$$

where the true force is expressed by

$$\nabla E(r_i)|_\perp = \nabla E(r_i) - \nabla E(r_i) \cdot \hat{\tau}_i, \tag{2.43}$$

Here, E is the energy of the system, a function of all atomic coordinates, $\hat{\tau}_i$ is the normalized local tangent at image i. The spring force can be written as,

$$F_i^s|_{||} = k(|r_{i+1} - r_i| - |r_i - r_{i-1}|) \cdot \hat{\tau}_i. \tag{2.44}$$

By performing the SCF based on DFT method, each image is simultaneously optimized to find the lowest energy possible while maintaining equal spacing to neighboring images. When the force is minimized according to the force convergence criteria, the MEP is obtained. However, it require a large number of images to exactly find the saddle point along the MEP. The climbing image NEB (cNEB) [44] was later developed to solve this problem by removing the spring force for the highest energy image (i_{max}), called the climbing image. This small modification does not cost any significant computational effort and information about the shape of the MEP is still maintained. In this method, the force acting on i_{max} is given by,

$$F_{i_{max}} = -\nabla E(r_{i_{max}}) + 2\nabla E(r_{i_{max}})|_{||}. \tag{2.45}$$

The true force acting on this image along the tangent is inverted. The climbing image tries to maximize its energy along the band, and minimize in all other directions. Therefore, when this image converges, we will be able to find the saddle point and MEP. This can be achieved with a small number of images and a reduced computational cost.

2.7 DFT investigations of defect thermodynamics

First-principles calculations based on DFT Framework are crucial tools for defect calculations. The methods can provide an in-depth understanding of defect chemistry and physics, such as the most favourable type of defects, incorporating lattice sites, effects on electronic and ionic conduction, or even optimal synthesis conditions. These theoretical results can significantly explain what obtained in experiments and also serve as guidelines to be applied in materials engineering.

2.7.1 Concentration and formation energy of defect

Defect concentration is a key factor that directly governs the effects of created defects on materials properties. For instance, the capacity and intercala-

tion processes in LiFePO$_4$ are drastically degraded with a higher concentration of Fe$_{Li}$ antisite [73]. Thereofre, it is possible to manipulate properties of materials by tailoring the defect concentrations. Under the assumption of thermodynamic equilibrium, the concentration of defect D ($c[D]$) at elevated temperature T is defined as follows [107, 35],

$$c[D] = N_{site}N_{config} \, exp\left(\frac{-E^f[D]}{k_\mathrm{B}T}\right),\qquad(2.46)$$

where N_{site} is the number of sites that defect can be incorporated in lattice per unit volume, N_{config} is the number of equivalent configurations, k_B is Boltzmann's constant, and $E^f[D]$ is a formation energy of defect D. From this formalism, we know that the defect with a lower E^f can form with a higher concentration in the corresponding host lattice. Based on the DFT method, the total energies of many-body systems can be determined and used to calculate the defect formation energy using the following equation [121, 106],

$$E^f[D^q] = E_\mathrm{tot}[D^q] - E_\mathrm{tot}(\mathrm{bulk}) - \sum_i n_i\mu_i + q\left(\varepsilon_\mathrm{F} + E_{VBM}\right) + E_\mathrm{corr},\quad(2.47)$$

where $E_\mathrm{tot}(\mathrm{D}^q)$ and $E_\mathrm{tot}(\mathrm{bulk})$ are the total energies of supercell containing defect D in charge state q and that of pristine system, respectively. The third term is the product of the number of atomic species i (n_i), that are removed (denoted by -) or added (denoted by +) to create the defect D, and the corresponding atomic chemical potential (μ_i). The Fermi level (ε_F) is referenced to the top of the valence band in bulk (E_{VBM}).

It is worth noting that the uncertainties of calculated defect formation energy are typically emerged from the artificial interactions between a charged defect and its periodic images. To get rid of for these interactions, it requires the use of huge supercell and hence an expensive computational resources. However, various schemes have been proposed to correct this finite-size supercell errors, such as (i) Makov and Payne [72], (ii) Freysoldt, Neugebauer, and Van de Walle [36] and (iii) Lany and Zunger [66]. More detail about these corrections is reviewed in ref.[61]. In this thesis, the correction proposed by Freysoldt, Neugebauer, and Van de Walle (FVN) is employed to determine the finite-size supercell correction term (E_{corr}). In this thesis, the notation of defects is based on the formalism described in Ref.[107], where V_D, D_i and $D1_{D2}$ represent D vacancy, D interstitial and the substitution of $D2$ for $D1$.

2.7.2 Chemical potentials

The chemical potential (μ_i) is a conjugate thermodynamic variable, which can represent experimental synthesis conditions in terms of the temperature (T) and partial pressure (P) [121, 107]. In vacuum-based synthesis, i.e., solid

35

state synthesis, the reaction entropy is dominated by the entropy of O_2, and the effect of temperature is mostly described by the change in μ_O [47, 87]. Considering O_2 as an ideal gas, the dependence of μ_O on T and P can be written as,

$$\mu_O(T,P) = \frac{1}{2}\left[\mu_{O_2}(T,P_0) + k_B T \ln \frac{P_{O_2}}{P_0}\right], \qquad (2.48)$$

and $\mu_{O_2}(T,P)$ is determined by,

$$\mu_{O_2}(T,P) = \Delta H_{O_2}(T,P_0) - T S_{O_2}(T,P_0) + H_{O_2}(0.P_0), \qquad (2.49)$$

where P_0 is the reference partial pressure of O_2 at 1 atm and $\Delta H_{O_2}(T,P_0)$ = $H_{O_2}(T,P_0)$ - $H_{O_2}(0,P0)$. The temperature-dependent parameters of O_2, namely enthalpy (H) and entropy (S), are taken from the thermochemical tables [21] while $H_{O_2}(0,P_0)$ corresponds to the calculated total energy of O_2. The lower μ_O is relevant to either the higher T or lower P_{O_2} or the presence of oxygen-reducing agents in the system. For instance, O_2 is supposedly abundant during growth process when μ_{O_2} is equivalent to the total energy of O_2, which is termed as O-rich or extreme oxidizing condition.

However, the value of all constituent μ_i must satisfy the stability condition of the host compound so that it will not be uniformly grown or disintegrated. Let assume we consider $LiFePO_4$ compound, its stability condition under thermodynamic equilibrium can be written as

$$\mu_{Li} + \mu_{Fe} + \mu_P + 2\mu_{O_2} = \Delta H^f(LiFePO_4), \qquad (2.50)$$

where ΔH^f is the formation enthalpy. To prevent the precipitation of other competing phases, such as metallic Li or inert mass Li_3PO_4, this condition needs to be further limited by a set of constraints imposing by the competing phases, for example,

$$\mu_{Li} < \Delta H^f(Li-metal) \qquad (2.51)$$
$$3\mu_{Li} + \mu_P + 2\mu_{O_2} < \Delta H^f(Li_3PO_4). \qquad (2.52)$$

By solving the stability condition bound by various constraints, the possible range of each chemical potential can be determined. The obtained μ_i can be used to evaluate the parameters of synthesis conditions.

2.7.3 Binding energy of defect complex

When point defects occur with high c or at low T, they can also agglomerate and form defect complexes. To determine the likelihood of complex defect formation between $X1$ and $X2$, the binding energy of $X1$-$X2$ defect complex (E_b) can be computed using the formation energies of the complex and its constituents as shown in following equation [107],

$$E_b(X_1 - X_2) = E^f(X_1) + E^f(X_2) - E^f(X_1 - X_2). \tag{2.53}$$

In principle, the complex should be bound and stable with a positive E_b. However, it might not readily form in the lattice if the concentration of the complex is lower than that of its constituents. In order to guarantee the formation of defect complex under equilibrium conditions, E_b is required to be higher than the larger of $E^f(D1)$ and $E^f(D2)$ [107, 35].

2.8 Evaluation of intercalation voltage profiles

Typically, a cell voltage of SIB is proportional to the chemical potential difference of Na in anode and counter cathode [98],

$$\bar{V}(x) = -\frac{\mu_{Na}^{cat}(x) - \mu_{Na}^{an}(x)}{e}. \tag{2.54}$$

The chemical potential can thus be computed based on the thermodynamics of these electrodes. The average intercalation voltage $V(x)$ can be approximated by the standard Nernst equation,

$$\bar{V}(x) = -\frac{\Delta G_r}{\Delta x}, \tag{2.55}$$

where the numerator is the Gibbs free energy ($\Delta G_r = \Delta E + P\Delta V - T\Delta S$) associated with the following reaction,

$$Na_{x_2}MXO_4 \Leftrightarrow Na_{x_1}MXO_4 + \Delta x \cdot Na^+ + \Delta x \cdot e^-, \tag{2.56}$$
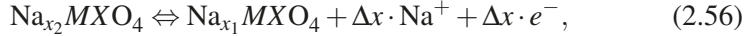
whereas the denominator is the number of extracted Na^+ ions ($\Delta x = x_2 - x_1$). As the contributions of volume (ΔV) and entropy (ΔS) to ΔG_r are relatively much smaller than the internal energy (ΔE), the average intercalation voltage for the above reaction can directly be approximated as a function of Na intercalation content as follows [7],

$$\bar{V}(x_1, x_2) = \frac{-E_{tot}(x_2) - E_{tot}(x_1) - \Delta x \cdot E_{tot}(Na)}{\Delta x}, \tag{2.57}$$

where $E_{tot}(x_2)$, $E_{tot}(x_1)$ and $E_{tot}(Na)$ denote the total energy of $Na_{x_2}MXO_4$, $Na_{x_1}MXO_4$ and bcc-Na metal, respectively, in eV unit.

In order to have a clear picture of the voltage profiles and intercalation mechanism, the intercalation voltage as a function of x can be determined by considering the formation energy of desodiated configurations $\Delta E(x)$ as defined below,

$$\Delta E(x) = E_{tot}(x) - \left[\frac{xE_{tot}(x_{max}) + (x_{max} - x)E_{tot}(x_{min})}{(x_{max} - x_{min})} \right], \tag{2.58}$$

where x is variant in a range of the maximum number (x_{max}) to the minimum number (x_{min}) of Na$^+$ ions depending on the intercalation reaction of interest. Assembling all the obtained $E_{form}(x)$, we have constructed the convex hull to find a set of the most likely configurations during the intercalation reactions. The voltage plateaus of the corresponding reactions are defined by the different slopes of each tie line on the convex hull.

3. Kröhnkite-based bisulfate polyanionic cathode materials

Hydrated alkaline metal bisulfates $A_2M(SO_4)_2 \cdot nH_2O$ (where A = Li, Na, K, Rb, Cs; M = Mg, Mn, Fe, Co, Ni, Cu, Zn, Cd) is one of the interesting classes of sulfate-based polanionic materials due to the variability in the hydration degrees and the complexity of the monoclinic framework. Hydrated derivatives adopt various known mineral structures, such as blöedite, konyaite and leonite. Based on the concept of sustainability, the exploration of these derivatives inspires the possibility of utilizing the available mineral sources as precursors to prepare novel superior materials.

Recently, a new candidate cathode for Na-ion batteries, known as kröhnkite-type bihydrated sulfate $Na_2Fe(SO_4)_2 \cdot 2H_2O$ (termed as NFS2H), was successfully synthesized at low temperature (80°C) in the work of Barpanda and his colleagues [11]. Apart from the benefits of containing inexpensive and abundant elements, it provides a high $Fe^{2+/3+}$ redox potential at 3.25 V (vs. Na/Na$^+$) and a reversible capacity of 70 mAh/g. This material is different from other sulfate-based cathodes in terms of its appealing ability to possess a manipulable hydration level. Each hydrated derivative shows distinct morphology, electronic, and electrochemical properties. For instance, it can transform into blöedite $Na_2Fe(SO_4)_2 \cdot 4H_2O$ [81] under moist conditions, and become either anhydrous $Na_2Fe(SO_4)_2$ or alluaudite $Na_2Fe_2(SO_4)_3$ in the dehydration reaction [74, 75]. While poor electronic conductivity is a major concern, this material was experimentally found to show a fast Na$^+$ ions diffusion [11]. However, the sodium diffusion mechanism in NFS2H, including other fundamental properties such as electronic properties and defect formations, have not been explored much. Thus, it motivates us to initiate the first-principles studies with the main goal to fundamentally understand the diffusion mechanism in the NFS2H cathode.

3.1 Description of crystal structure

In order to have an insight into this material, it is essential to understand the nature of crystal structure and bulk properties. The crystal structure of monoclinic kröhnkite-type NFS2H is shown in Fig.3.1. It is mainly composed of three structural units: (i) an octahedral $FeO_4(H_2O)_2$, (ii) a tetrahedral SO_4, and (iii) a Na$^+$ ion layer. Two hydrogen ions are attracted by lone pairs of electrons from oxygen (O5-site) in the z-component of the FeO_6 octahedron as if
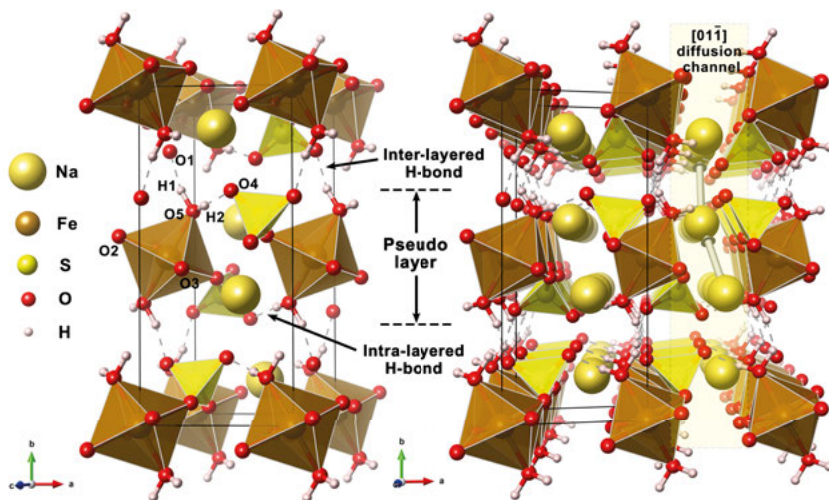
Figure 3.1. Illustration of kröhnkite-type NFS2H structure. Dashed bonding represents hydrogen interactions between and within pseudolayers. Non-equivalent sites of O and H are assigned in the left-hand side structure and the Na$^+$ ion diffusion along [01$\bar{1}$] channel is demonstrated in the yellow-shaded box in the right-hand side analogue.

there are water-like molecules inside NFS2H, which are called structural H$_2$O units. Each of the remaining four O ligands (O1-O4) is corner-linked with a bridging tetrahedral SO$_4$ generating a two-dimensional framework of infinite octahedralâtetrahedral chains along *c*-axis. When looking toward the *c*-axis, one can simply see a convoluted channel of Na$^+$ ions lying along the *b*-axis, which was claimed to be the Na$^+$ diffusion channel in this material [11, 99].

This structure is regarded as a pseudo-layered structure where each layer is bound by inter-layered hydrogen bonds between O1 and H1. Moreover, the other hydrogen at H2 site also creates an intra-layered hydrogen bond with O4 within each layer. To investigate the influence of the structural H$_2$O, a whole H$_2$O and hydrogen ions are removed from the NFS2H structure. It is found that removing a whole H$_2$O unit leads to a huge structural change. When all hydrogen ions are removed, the octahedral FeO$_6$ undergoes a strong octahedral distortion along with 4.59% volume contraction and an increasing separation distance between pseudo-layers. Thus, the presence of structural H$_2$O is proved to be important for stabilizing the NFS2H structure.

3.1.1 Effect of exchange correlation and vdW correction

In order to accurately describe the electron interactions in NFS2H, various exchange correlation functionals are employed to optimize the geometry of NFS2H lattice. Moreover, we also apply the DFT-D2 approach developed by Grimme [40] in order to incorporate the the long-range interactions, i.e., the

inter- and intra- layered hydrogen bonds, into our DFT calculations. In this case, the energy functional including the contribution of long-range interaction (E_{DFT+D2}) can be determined by adding the sum of the induced dipole-dipole interactions (E_{disp}) into the total energy calculated within the KS-DFT method (E_{KS}),

$$E_{DFT+D2} = E_{KS} + E_{disp} \tag{3.1}$$

The dispersion correction term E_{disp} is expressed as

$$E_{disp} = -s_6 \sum_{i<j} \frac{C_6^{ij}}{r_{ij}^6} \frac{1}{1 + e^{-d(R_{ij}/R_r - 1)}} \tag{3.2}$$

where s_6 is a global scaling factor, C_6^{ij} is the dispersion coefficient, d is an adjustable parameter, R_{ij} are the atomic distances and $R_r = R_i + R_j$ is the sum of the van der Waal (vdW) radii of atom i and j. This approach has been proved to provide an improved accuracy of DFT calculations in the vdW systems. Table 3.1 shows all calculated lattice parameters, bond distances, magnetic moments on Fe (μ_{Fe}), volume (V), and electronic band gaps (E_g) for the fully-sodiated NFS2H, which are calculated within PBE, PBE+U (with/without D2 correction), and HSE06 functionals. Overall, the calculated lattice parameters are quite consistent with experimental values. The PBE functional shows an underestimated band gap (0.21 eV) as compared to the much larger band gaps of 4.13 eV obtained from the HSE06 functional. This indicates the presence of a strong self-interaction in this system. Thus, this compound should behave like a wide band gap insulator. The cancellation of self-interaction error in PBE+U and HSE06 causes an increase in the Fe^{2+} spin moment from 3.61 μ_B (PBE) to 3.72 μ_B (HSE06) due to the localization of Fe $3d$-electrons. We find that the most appropriate U value is 4.7 eV because the descriptions of band gap and the density of states (DOS) profile are nearly identical to the HSE06 outcomes. The PBE+U+D2 results give a better prediction of the lattice paramaters, close to the experimental values, as compared to the PBE+U analogues. This can be clearly seen from the higher Baur's distortion index for FeO$_6$ octahedra Δ(Fe-O) obtained within PBE+U (without D2). This index is computed from

$$\Delta(M - O) = \frac{1}{n} \sum_{i=1}^{n} \frac{|(M - O)_i - \langle M - O \rangle|}{\langle M - O \rangle}, \tag{3.3}$$

where n is the coordination number of M center ion, $(M$-O$)$ is the bond length between M and O, and $\langle M$-O$\rangle$ is the average bond length. Thus, PBE+U+D2 with $U = 4.7$ eV is employed throughout this chapter.

Table 3.1. *Calculated lattice parameters, cell volume (V), average spin moment of Fe (μ_{Fe}), band gap (E_g), the Baur distortion coefficient (Δ), and an average bond distance $\langle M - O \rangle$ of bulk NFS2H calculated using PBE+U (with/without D2 correction) and HSE06 functionals.*

| | PBE+U | PBE+U+D2 | | | | |
	$U = 4.7$	$U = 0$	$U = 4.7$	$U = 5.1$	HSE06	Exp.
a (Å)	5.81	5.75	5.77	5.77	5.71	5.764
b (Å)	13.15	12.81	12.84	12.84	12.73	12.975
c (Å)	5.53	5.45	5.45	5.45	5.41	5.449
β (°)	106.09	106.83	106.78	106.79	106.81	-
V (Å^3)	407.75	384.52	386.25	386.33	376.74	-
μ_{Fe} (μ_B)	3.76	3.61	3.75	3.76	3.72	-
E_g (eV)	4.08	0.21	4.10	4.40	4.13	-
Δ(Fe-O)	0.015	0.027	0.023	0.023	0.024	-
$\langle$Fe-O$\rangle$	2.166	2.134	2.148	2.148	2.129	-
$\langle$Fe-O2$\rangle$	2.195	2.182	2.180	2.183	2.173	-
$\langle$Fe-O3$\rangle$	2.187	2.172	2.189	2.188	2.163	-
$\langle$Fe-O5$\rangle$	2.117	2.049	2.074	2.074	2.053	-
$\langle$S-O$\rangle$	1.496	1.494	1.494	1.494	1.469	-
$\langle$H-O$\rangle^a$	1.708/1.672	1.651/1.619	1.660/1.623	1.662/1.622	1.655/1.620	1.86

^{a} Given as intra/inter-layered hydrogen bond distances.

3.1.2 The inductive effect

In order to understand the bonding nature, we have calculated the Electron Localization Function (ELF) as plotted in Fig.3.2. As electrons are strongly localized around the H_2O unit as well as in the middle of S-O bonds in the SO_4 unit, it clearly demonstrates a strong covalent bonding of these two units. Moreover, small electron localization between hydrogen and oxygen atoms signifies the presence of hydrogen bonds. As shown in Fig.3.2(b), the electrons delocalized around Fe sites reveals the fact that Fe-O bonds in FeO_6 are highly ionic and, hence, implies the possibility for NFS2H to offer a high redox potential according to the concept of the inductive effect.

3.2 Intercalation voltage profile

In order to determine the voltage profile theoretically, it is crucial to find the minimum energy configuration (MEC) of desodiated structures with a variant Na content along the considered desodiation reaction. To achieve that, the SQS method is performed using the orderliness optimization in the evolutionary algorithm as implemented in USPEX code [37, 123]. It is revealed that the MEC of half-desodiated phase can be obtained in the sampled configuration with the highest distance between two neighboring Na$^+$ ions and the highest average Na-Na distance due to the lowest Coulomb interactions amongst
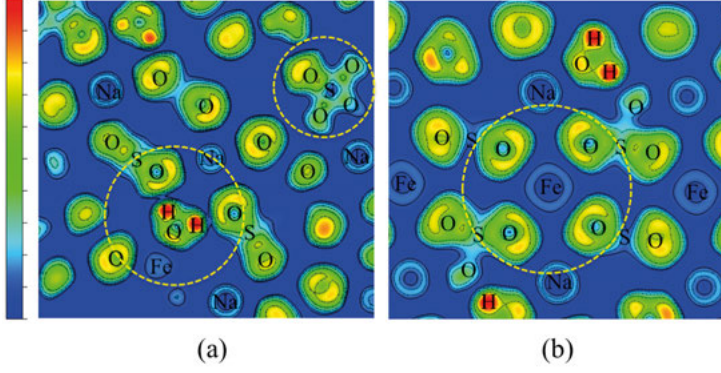
Figure 3.2. The 2D contour plot of ELF for NFS2H (a) in the plane of a structural H_2O unit and (b) in that of octahedral FeO_6. The intensity of electron localization is represented by a color in contours as designated in a bar scale.

Na^+ ions. The half-desodiated structure is illustrated in Fig.3.3(a). Ab-initio molecular dynamics is performed for this obtained structure at 1500 K for 5 ps. We find that this MEC is dynamically stable as there are no broken bonds being observed during the simulation.

With the total energy of MECs obtained at different Na content (x), their formation energies can be calculated using Eq.**??** according to the below reaction,

$$Na_{x_2}Fe(SO_4)_2 \cdot 2H_2O \iff Na_{x_1}Fe(SO_4)_2 \cdot 2H_2O + \Delta x[Na^+ + e^-], \quad (3.4)$$
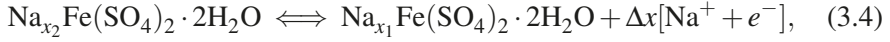
In Fig.3.3(b), the convex hull of E_{form} with respect to the x parameter shows two voltage plateaus at 4.01 and 5.31 V for half- and full-desodiation reactions, which are computed using Eq.2.57. As the calculated voltage for half-desodiation is higher than the experimental value of 3.25 V, we suggest that the voltage reduction may be attributed to a structural change in NFS2H during desodiation, particularly on the surface of NFS2H which is sensitive to moisture and can be transformed into ödite phase [81]. It is worth noting that the voltage for half-desodiation is predicted to be 3.51 V when excluding the vdW correction. The voltage for full desodiation is unlikely to occur due to the limit of the current electrolyte stability window for SIBs (4.5 V vs. Na/Na^+ for non-aqueous $NaClO_4$).

3.3 Small polaron formation

When one extra electron or hole is introduced in the system, it generally occupies the CBM or VBM, respectively, as a free charge carrier. However, they can get trapped by local lattice distortions at a certain location as a self-trapped
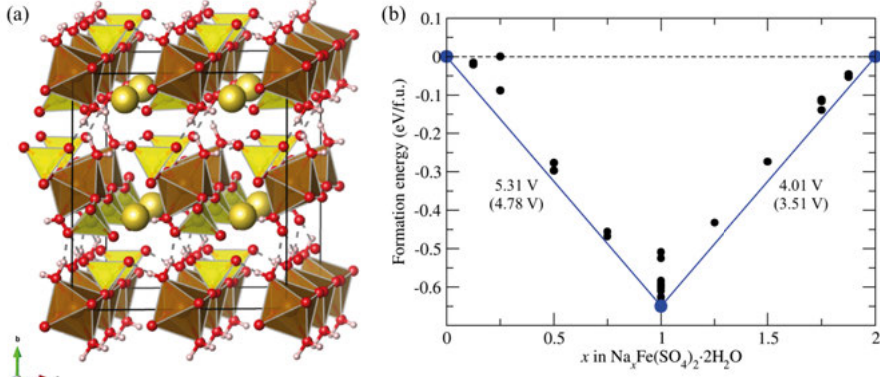
Figure 3.3. (a) The absolute minimum for $Na_2Fe(SO_4)_2 \cdot 2H_2O$ obtained from the structural order optimization. (b) A convex hull of calculated formation energies of $Na_xFe(SO_4)_2 \cdot 2H_2O$ per formula unit. Voltages calculated without D2 correction are shown in parentheses.

particle or so-called polaron [18, 5, 101]. When the radius of the lattice distortion for trapping the charge carrier is much larger than the lattice constant of the material, this polaron is called a large polaron. If the polaron is confined in a volume of one unit cell or less, it is called a small polaron. The small poloron has been found to be related to the optical properties and the difficulties in achieving p-type doping in several oxide materials, such as In_2O_3 [109] and TiO_2 [54]. On the other hand, it has been also reported that the small polaron plays a role in electronic conduction via hopping mechanism in wide band gap electrode materials used in batteries, such as Li_2O_2 [88], Na_2O_2 [3] and the well-known $LiFePO_4$ [47, 78, 32].

When a hole or electron is additionally introduced in the NFS2H supercell, we find that these charge carriers disperse on Fe sites throughout the lattice. Nevertheless, the additional hole is locally trapped as a small hole polaron (η^+) when applying a structural distortion onto a particular octahedral FeO_6, opposite to the case of the electron, which is not trapped in the fully-sodiated NFS2H. The dispersion and self-trapping hole are identified by band decomposed charge densities as shown in Fig.3.4. The stability of the self-trapped hole, or the self-trapping energy (E_{ST}), can be determined by the difference in the total energies between the localized and delocalized charge carriers,

$$E_{ST} = E_{tot}(bulk : e^-/h^+) - E_{tot}(bulk : \xi^-/\eta^+) - \Delta V, \qquad (3.5)$$

where $E_{tot}(bulk:e^-/h^+)$ and $E_{tot}(bulk:\xi^-/\eta^+)$ are the total energies of a supercell containing an extra delocalized electron e^- or hole h^+ and the one containing a self-trapped electron ξ^- or hole η^+, and ΔV is an alignment of average electrostatic potentials between the supercell with and without self-trapped carriers. Using this equation, we obtain a positive E_{ST} (0.239 eV),
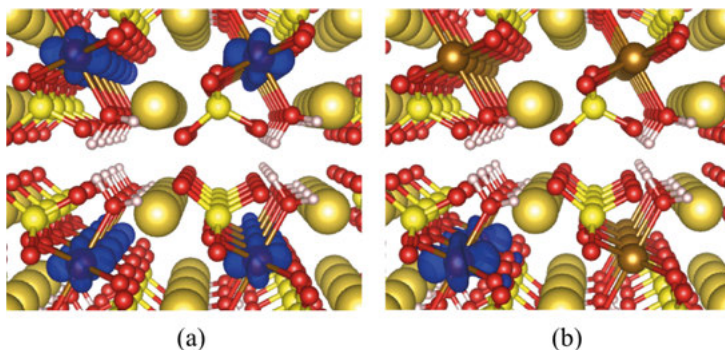
44

Figure 3.4. Band-decomposed charge density of (a) a delocalized hole and (b) a self-trapping hole in NFS2H. The charge density isosurfaces are shown at 10% of their maximum value.

which indicates the preferable formation of η^+ in NFS2H. We find that the formation of η^+ is coupled to various native defects in NFS2H, for example, the Na extraction during desodiation reaction. The influence of η^+ on defect formation and conductivity are intensively discussed in the next section.

3.4 Defect thermodynamics

The major difficulty for the defect formation study in polyanionic cathode materials is the determination of atomic chemical potentials that satisfy the thermodynamic boundary condition (or the stability condition) of a specific compound. An unphysical chemical potential, which conflicts with this condition, can severely mislead the interpretation of defect concentrations. In this regard, the evaluation of chemical potentials for NFS2H is primarily discussed before the defect calculation.

3.4.1 Chemical potential diagrams

In order to achieve the uniform crystallization of NFS2H compound, the atomic chemical potentials must satisfy the following stability condition,

$$2\mu_{\text{Na}} + \mu_{\text{Fe}} + 2\mu_S + 10\mu_O + 4\mu_H = \Delta H^f[\text{Na}_2\text{Fe}(\text{SO}_4)_2 \cdot 2\text{H}_2\text{O}]. \qquad (3.6)$$

Bound on these μ_i are constrained with the formation of several possible secondary phases as given in Fig.3.5(b). To be able to solve this equation, We specifically varied μ_S and μ_H to define the ranges allowing NFS2H crystallization by reducing the values from their rich conditions ($\mu_i = 0$ eV). First, μ_H is fixed within its available range and μ_S is subsequently varied. At a specific μ_S, a number of sets indicating μ_{Na}, μ_{Fe}, μ_O parameters is obtained
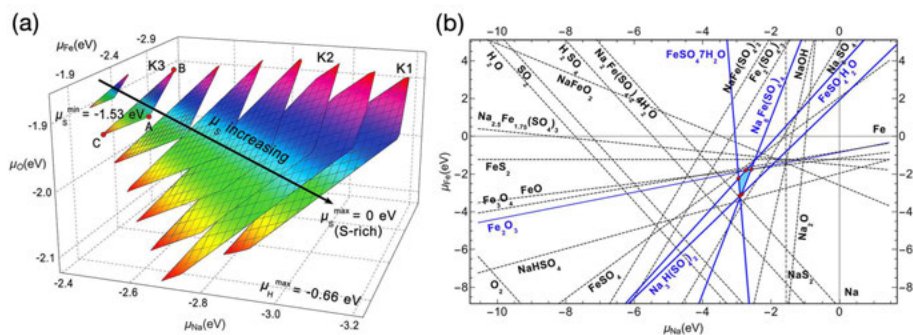
Figure 3.5. (a) Influence of varying μ_S on the phase boundary represented in three-dimensional chemical potential diagram for $Na_2Fe(SO_4)_2 \cdot 2H_2O$ at K condition, the possibly highest μ_H. (b) Projected chemical potential diagram at K2 condition onto the plane of μ_{Na} and μ_{Fe} showing competing phases we considered, and the phase boundary which is labeled in blue. Conditions only in the blue region will ensure the stability of this compound.

as illustrated by each stability region (a shaded polyhedral slice) in a three-dimensional chemical potential diagram in Fig.3.5(a). The corners of each slice represent thermodynamic equilibria (TEs) between two thermodynamic limits of competing phases.

To clearly identify the limiting phases for each slice, the diagram is projected onto a two-dimensional plot (μ_{Na} vs μ_{Fe}) as shown in Fig.3.5(b). Based on the exhaustive considerations, NFS2H is found to be thermodynamically stable under the conditions, -1.6 eV $\leq \mu_H \leq -0.5$ eV and -5.8 eV $\leq \mu_S \leq$ 0 eV. According to the variation of μ_H in this range, calculated chemical potential diagrams can be categorized into four types as follows: (i) **K** where $\mu_H = -0.66$ eV and $\mu_S = 0$, -0.40, -1.20 eV are denoted as K1, K2, and K3, (ii) **L** where $\mu_H = -0.95$ eV and $\mu_S = -0.90$, -1.20, -2.00, -2.80 eV are denoted as L1, L2, L3, and L4, (iii) **M** where $\mu_H = -1.11$ eV and $\mu_S = -2.00$, -2.60, -2.80, -3.60 eV are denoted as M1, M2, M3, and M4, and (iv) **N** where $\mu_H = -1.32$ eV and $\mu_S = -3.60$, -3.90, -4.30, -4.70 eV are denoted as N1, N2, N3, and N4, respectively, as shown in Fig.3.6. Each region is enclosed by different groups of limiting phases, which generally consist of $NaHSO_4$, $Na_3H(SO_4)_2$, $Na_6Fe(SO_4)_4$, Fe_2O_3, $Na_2Fe(SO_4)_2 \cdot 4H_2O$, $FeSO_4 \cdot nH_2O$ ($n = 4$ and 7) and $NaFe(SO_4)_2$ phases. Some of these compounds are parts and byproducts of synthetic reactions for NFS2H, for example, the precursor $FeSO_4 \cdot 7H_2O$, which can easily dissociate to $FeSO_4 \cdot H_2O$, and $Na_6Fe(SO_4)_4$ impurity phase in a dehydration reaction [11]. Moreover, based on these diagrams, one can determine the suitable experimental parameters for controlling the formation of secondary phases.
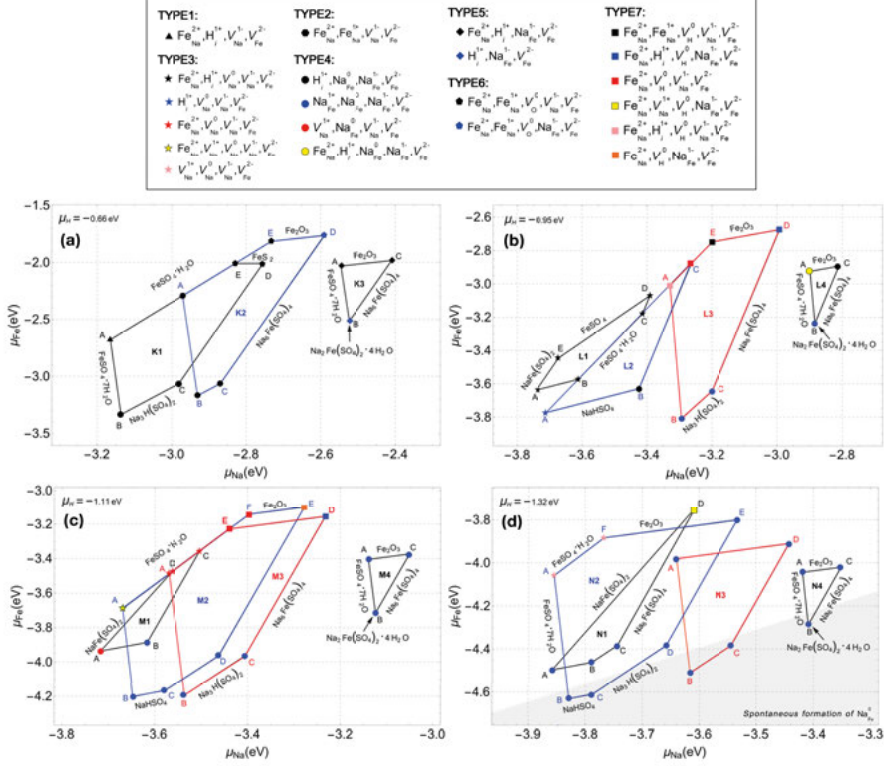
Figure 3.6. Schematics of chemical potential diagram for NFS2H in the available range of μ_i. Based on a variation of μ_H, they are divided into four primary conditions, where (a) μ_H = -0.66 eV, (b) -0.95 eV, (c) -1.11 eV, (d) -1.32 eV termed as K, L, M, N conditions, respectively, and plotted against μ_{Na} and μ_{Fe}. In each condition, phase boundaries are further divided with respect to μ_S and compounds limiting phase boundary are specified on the edge of polyhedron. Groups of dominant defects are presented at each TE by symbols as assigned beside the diagrams. Conditions in the red-shaded region are subject to a spontaneous formation of Na_{Fe}.

3.4.2 Solution-based synthesis

Since NFS2H is synthesized in a solution-based growth environment through a classical dissolution and precipitation route by dissolving equimolar amounts of Na_2SO_4 and $FeSO_4·7H_2O$ in distilled water, the calculated chemical potentials should be therefore correlated with mole fraction or concentration in the solution corresponding to Raoult's law [9], in which the chemical potential of each component is re-written as

$$\mu_i(T,P) = \mu_i(T,P_0) + RT\ln(x_i), \qquad (3.7)$$

where x_i is the mole fraction of the component i in the ideal solution and R is the gas constant. Note that R is the product of k_B and the Avogadro constant. In principle, pH is determined by,

$$pH = -\log c[H^+] \tag{3.8}$$

When incorporating this relation with the definition of μ_H, we find that μ_H is an inverse linear function of the pH value at a constant T. The pH of the solution is extremely acidic (pH = 0) or basic (pH = 14) when μ_H reaches its maximum or minimum, respectively, corresponding to the water chemical potential limit, $\mu_{H_2O} = \mu_{H^+} + \mu_{OH^-}$. We assume that $\mu_H(max) = (1/2)E_{tot}(H_2)$ at pH = 0 and $\mu_H(min) = E_{tot}(H_2O) - E_{tot}(OH)$ at pH = 14. Using the linear interpolation between the $\mu_H(max)$ and $\mu_H(min)$, the pH value can be approximated through the following equation,

$$pH = 14 \times \frac{\mu_H - \mu_H(max)}{\mu_H(min) - \mu_H(max)}, \tag{3.9}$$

According to the boundary of calculated μ_{H^+}, we find that NFS2H is likely to form under an acidic-to-neutral condition ($2.0 \leq pH \leq 6.8$). Moreover, the specific values of μ_{H^+} for the K, L, M and N diagrams are corresponding to the pH conditions of 2.8, 4.0, 4.7, and 5.6, respectively. It should be noted that the pH value here is approximated just to see a qualitative trend of the effect of chemical potential on defect formation energy and conductivity.

3.4.3 Influence of native defects on electronic structures

The density of states of pristine NFS2H supercell and the ones with native point defects are shown in Fig.3.7. The energy states in pristine NFS2H (in Fig.3.7(a)) are mainly contributed by Fe-3d and O-2p orbitals. The VBM (and also the CBM) is dominantly contributed by Fe-3d orbitals, indicating the active behavior of $Fe^{2+/3+}$ redox potential in NFS2H. The introduction of some defects can give rise to intermediate states in the band gap, especially, for those associated with η^+ formation, i.e., V_{Na}^0, Na_{Fe}^0, and V_H^0. These intermediate states are merely contributed from the half-unoccupied states of Fe^{3+}-d orbitals and indicate the presence of η^+ induced by defects.

One can see that the transition of defect charge state is associated with the formation of η^+, instead of incorporating with the created defect. For instance, V_{Na}^0 consists of V_{Na}^{1-} and η^+. When electron is added in the lattice with V_{Na}^0, the electron will fill the polaron state and localize on the octahedral FeO_6, leaving only V_{Na}^{1-} in the lattice. An additional η^+ will be created when the q is increased from 0 to 1+. The charge state without η^+ will be regarded as an elementary charge state. Based on the DOS, we can identify the elementary defects in NFS2H, which consists of V_{Na}^{1-}, V_{Fe}^{2-}, V_O^0, V_H^{1-}, Na_{Fe}^{1-}, Fe_{Na}^{1+}, Na_i^{1+} and H_i^{1+}. The formation of η^+ is found in the cases of V_{Na}, V_{Fe}, V_H, Na_{Fe} and
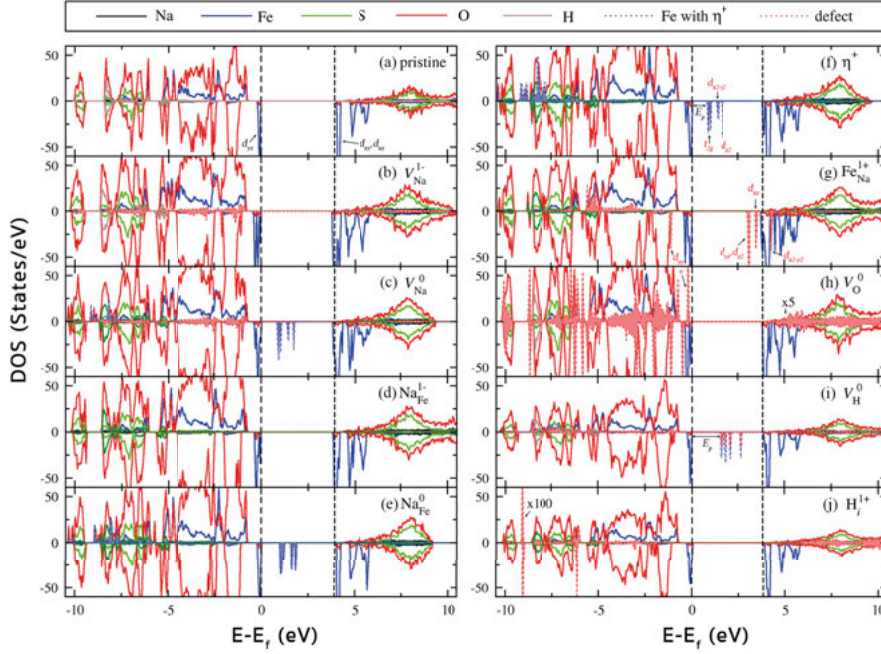
Figure 3.7. PDOS of NFS2H with/without either intrinsic defects or small hole polarons. Red and blue dot lines represent PDOS of atoms associated with a certain defect, and that of the Fe ion at which small hole polarons is situated, respectively. The area under these lines are highlighted by their corresponding line colors. The VBM and CBM are designated by dashed lines.

Fe_{Na}. We conclude that the change in electronic structure of defects mainly originates from η^+ formation. This implies that η^+ should play an important role in the electronic conduction of NFS2H.

3.4.4 Defect formation energy

Using Eq.2.47, defect formation energy can be determined under different TEs and plotted against the Fermi level as shown in Fig.3.8. We find that dominant defects in NFS2H could be Fe_{Na}, H_i, V_H, V_O, V_{Na}, Na_{Fe} and V_{Fe}, depending on the chosen equilibrium condition. This material cannot exhibit either n- or and p-type characteristics as both donors (Fe_{Na}) and acceptors (V_{Na} and Na_{Fe}) do not have a shallow level. The H^i has a shallow level but its E^f is too high in the n-type condition. Therefore, electronic conduction should not be governed by the band-like transport. In order to capture the general trend of E^f for all the TEs, the dominant defects are qualitatively summarized in Fig.3.6 by different symbols at corners of each stability region. From this figure, we conclude that (i) while the strong acidic condition (K conditions) provokes Fe_{Na}, it restrains the η^+ formation and (ii) at higher pH value, the

trend of dominant defects approaches the cases that are mainly governed by Na_{Fe}, which can occur spontaneously according to its unphysical negative E^f [35].
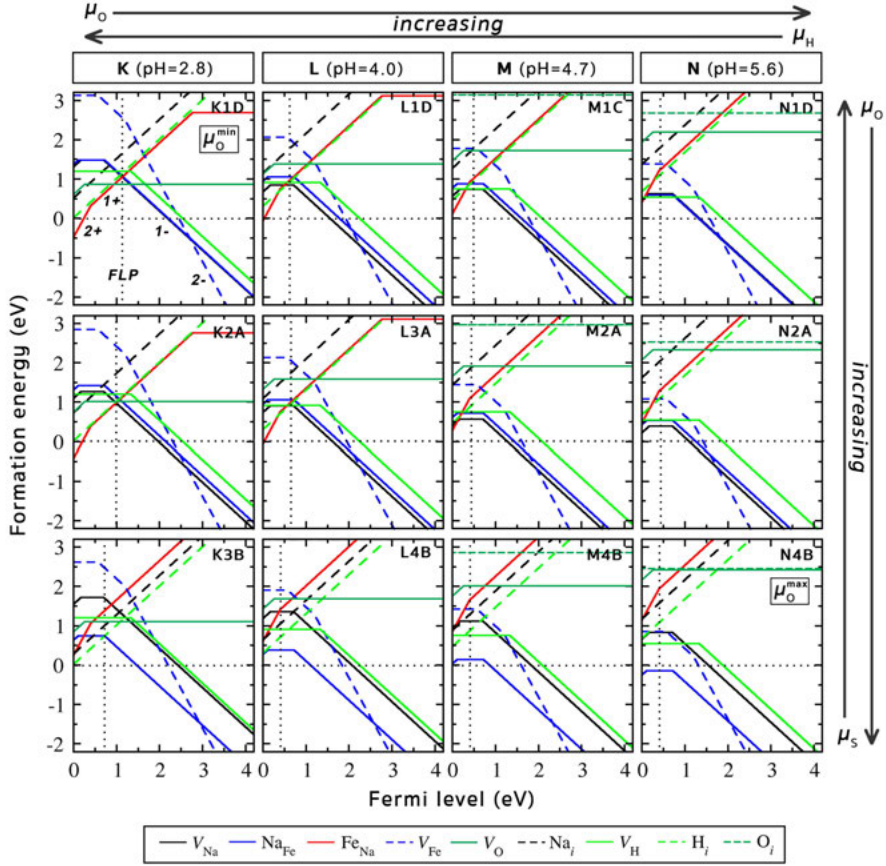

Figure 3.8. The variation of calculated formation energies for intrinsic defects in NFS2H at different TEs. Each plot is expressed as a function of the Fermi level with respect to the VBM, and the Fermi-level pinning (FLP) is represented by a vertical dashed line according to charge neutrality. All of the plots are given in the sequence of pH value, μ_O, and μ_S as described by the direction of arrows.

In order to calculate defect concentrations, the Fermi level pinning (FLP) is set by the condition of charge neutrality,

$$\sum_{D,i} q_i c_i [D^q] + n_h - n_e = 0 \qquad (3.10)$$

where n_h and n_e are the concentration of free holes and electrons, which can be approximated by an effective mass of electron and hole [57]. Due to the flat-band character of the VBM and CBM observed in NFS2H, n_h and n_e should
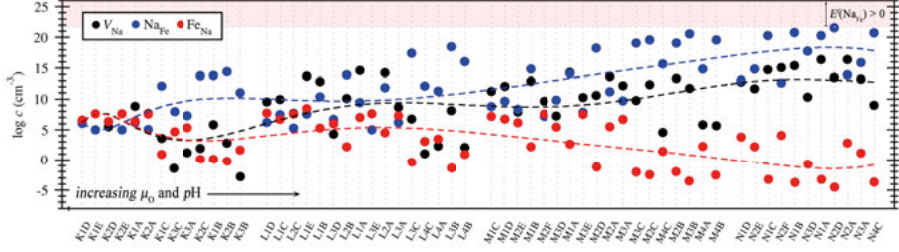
Figure 3.9. Comparison of defect concentrations of V_{Na}, Na_{Fe} and Fe_{Na} at each TE. The change in defect concentrations with respect to pH and μ_O is expressed by non-linear curve fitting (dashed-lines). Spontaneous formation of Na_{Fe} can emerge at the upper limit of pH where its formation energy becomes negative in a red-shaded area.

be relatively small and be cancelled out in this case. Defect concentration under each TE is evaluated at the synthesis temperature of 343 K according to the corresponding FLP as shown in Fig.3.9. This figure clearly shows that the channel blockage Fe_{Na} can be suppressed with the increasing pH of mixing solution or an addition of O content in the synthesis environment. Such conditions also lead to a higher concentration of V_{Na}^0 and Na_{Fe}^0, and thus an increasing amount of small hole polarons.

3.5 Diffusion mechanism

Based on vacancy-assisted diffusion and cNEB method, a migration energy is calculated for the Na^+ ion diffusion along six possible pathways as demonstrated in Fig.3.10. These results are summarized in Table 3.2. The presence of η^+ in the case of V_{Na^0} slightly increases the E_m along these paths by 0.1 eV. A single η^+ shows an isotropic hopping with a low E_m of 0.2 eV. Thus, the electronic conductivity should be dictated by the fast η^+ hopping. Owing to the lowest E_m for the Na^+ diffusion along path1 and path3, the intercalation mechanism is revealed to moderately occur along [01$\bar{1}$] direction with a migration energy of 1.16 eV.

In order to account for the fast-ion diffusion, diffusion mechanisms associated with defects are envisaged. We find that the dominant Na_{Fe} can migrate to V_{Na} site in its proximity and leave V_{Fe} behind. Fig.3.11 shows that the E_m of Na_{Fe} diffusion are 0.73 and 0.92 eV along path1 and path2 respectively. The diffusion along path1 is more preferable because of a lower distortion created by the moving Na^+ ion. This mechanism is not only faster than the one along the [01$\bar{1}$] direction, but also provides a cross-link between each [01$\bar{1}$] channel which effectively reduces the channel-blocking issue in NFS2H. However, according to the monoclinic framework of NFS2H, the [01$\bar{1}$] channel is still required in the intercalation process. Thus, it can be suggested that if this main channel is truncated, the enhanced ionic conductivity should be achieved.
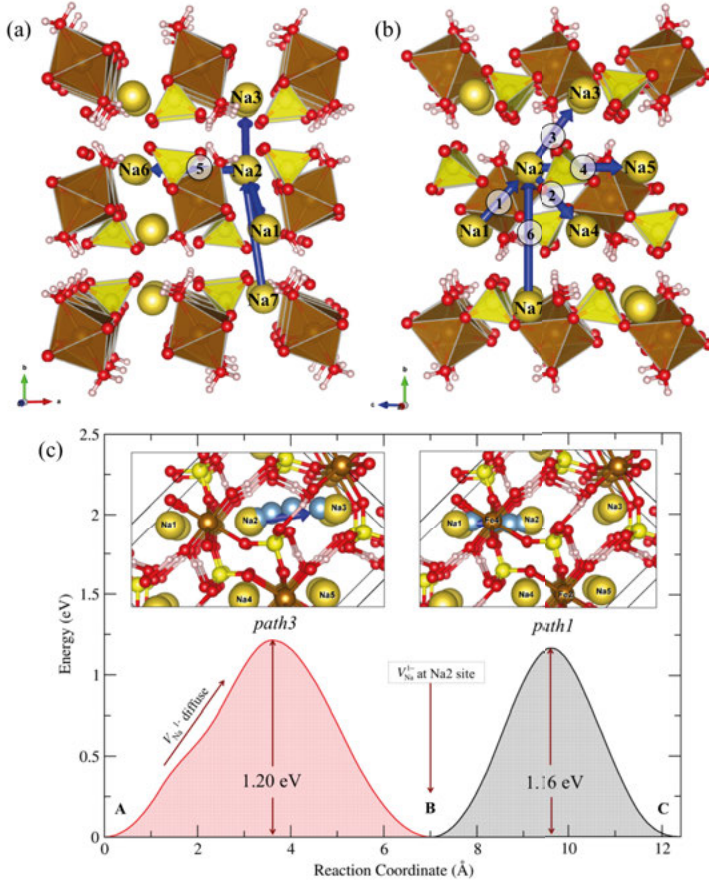
Figure 3.10. Illustration of Na$^+$ diffusion pathways in a supercell lattice: (a) in *c*-axis and (b) in *a*-axis. (c) Migration barriers of V_{Na}^{1-} along MEPs of path 3 and path 1. The insets show the migration pathway of Na$^+$ ion in the [01$\bar{1}$] direction.

3.6 Conductivity

Fig.3.12(a) shows the activation energy for ionic and electronic diffusion (Q_{ionic} and Q_{elec}) based on thermal activation in defective- NFS2H, where $Q = E_m + E^f$. While E^f of the most dominant associated with Na$^+$ ion diffusion is used to compute Q_{ionic}, the Q_{elec} depends on the E^f of defects that induces η^+. Both activation energies are rapidly decreased following the increasing μ_O and pH due to the decrement of E^f. Based on the Einstein relation [57], the mobility of the Na$^+$ ion can be obtained using the following equation,

$$\mu_m = \frac{vqa^2}{k_B T} exp(\frac{-Q}{k_B T}),$$ (3.11)

Table 3.2. *Migration energy (E_m) and diffusion distance for Na^+ ion along pathways in NFS2H containing neutral and singly-negatively charged sodium vacancies (V_{Na}^0 and V_{Na}^{1-}).*

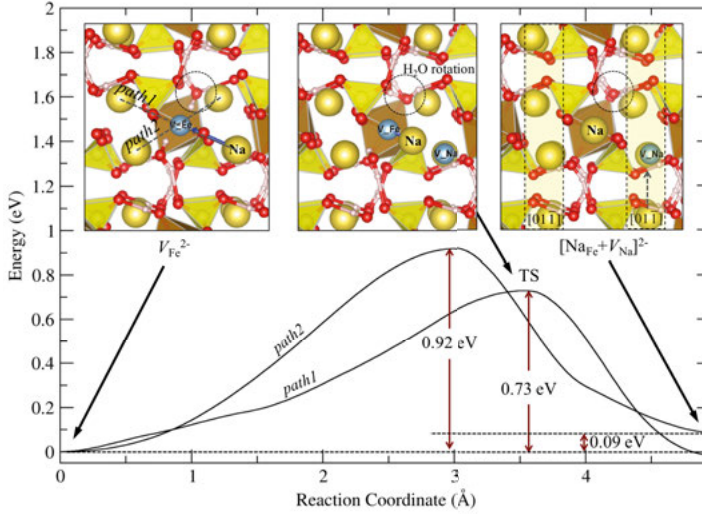|	V_{Na}^0						V_{Na}^{1-}		
	1	2	3	4	5	6	1	2	3
Initial	Na1	Na2	Na2	Na2	Na2	Na7	Na1	Na2	Na2
Final	Na2	Na4	Na3	Na5	Na6	Na2	Na2	Na4	Na3
Distance (Å)	3.981	4.257	4.406	5.447	5.770	6.482	3.981	4.257	4.406
E_m (eV)	1.288	1.760	1.237	1.962	1.846	2.926	1.157	1.761	1.203

Figure 3.11. Minima energy pathways and migration energies for ionic diffusion associated with Na_{Fe} defect in NFS2H. Structural changes during the diffusion are demonstrated in the insets as well as the predicted diffusion mechanisms where an exchange of Na^+ ion between Na_{Fe} and V_{Na} sites in [01$\bar{1}$] channel is taken place.

where ν is the attempt frequency for migration and a is the diffusion distance. The total conductivity σ can be determined from the sum of the product of $c[D^q]$ and μ^m as follows,

$$\sigma = \sum_i |q_i| c[D_i^q] \mu_i^m, \tag{3.12}$$

The calculated ionic and electronic conductivity (σ_{ionic} and σ_{elec}) are shown as a function of μ_O and pH value in Fig.3.12. The σ_{ionic} is determined from the Na^+ diffusion along the alternative channel at room temperature (300 K). We find that both σ_{ionic} and σ_{elec} for NFS2H prepared at low pH condition are poor not only due to the defect hindrances but also are the low concentration of V_{Na}, Na_{Fe} and induced η^+. Our results can be reasonably compared with the experimental measurements [81, 80] and explain the source of the enhanced
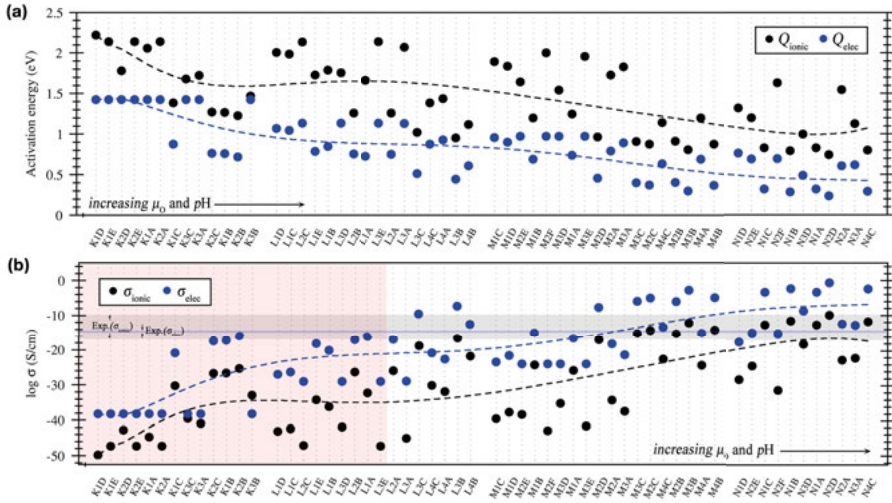
Figure 3.12. (a) Activation energies for electronic and ionic diffusion in NFS2H. (b) Electronic and ionic conductivities computed according to the respective activation energy and defect concentration at each TE. Their experimental values are shown in blue- and black-shaded area, respectively. Trends of calculated electronic and ionic components are represented by dashed-lines obtained from polynomial curve fitting.

conductivity in NFS2H/C composite structure, which is attributed to the fast η^+ hopping and the Na$^+$ diffusion along the alternative channel. By controlling the pH value in weak acidic condition (pH = 4.7-5.6), these parameters are predicted to reach the order of 10^{-10} and 10^{-3} S/cm at room temperature, respectively.

4. Non-stoichiometry in Alluaudite-type sulfate cathodes

Alluaudite-type sodium iron sulfate $Na_2Fe_2(SO_4)_3$ cathodes (termed as NFS) have emerged as one of the most suitable replacements to lithium-ion battery cathodes. Apart from containing low-cost and abundant elements, it delivers the highest operating voltage among any Fe-based cathode materials (3.8 V vs. Na^+/Na), a high specific capacity of ca. 100 mAh/g, fast ion transport and excellent cyclability [12, 31, 71]. Interestingly, unlike other cathode materials, this material generally occurs in the non-stoichiometric form $[Na_{2+2\delta}Fe_{2-\delta}(SO_4)_3]$ (termed as NFSδ) with partial Na substitutions on Fe sites, where the non-stoichiometric degree $\delta = 0$, 0.25 and 0.5 depends on the synthesis conditions. The non-stoichiometry in alluaudite cathodes was studied in the experimental work of Oyama and his colleagues [89]. They reported that the change in δ (within $0 \leq \delta \leq 0.4$) is associated with the precipitation of impurity phases, which is minimized in the case of NFS0.25. For this reason, many contemporary research has particularly directed to this non-stoichiometric compound.

Inspired by the idea that NFS0 is expected to offer an enhanced specific capacity of 120 mAh/g, this stoichimetric compound should be a more promising cathode as compared to the NFS0.25. However, the influence of the non-stoichiometry on properties is yet to be intensively unveiled in this class of material till date, especially based on the fundamental perspectives. In this regard, the first-principles calculations are performed with the main aims to understand the nature of impurity precipitation and find a suitable synthesis condition for NFSδ compounds. The influence of the non-stoichiometry towards defect thermodynamics (Paper III) and electrochemical behavior (Paper IV) in the alluaudite-type NFSδ where $\delta = 0$, 0.25 and 0.5 are provided in this Chapter.

4.1 Non-stoichiometry and crystal structure

The initial important step is to clearly determine the crystal structures of each NFSδ. The crystal structure of NFS0.25 was reported to adopt either $P2_1/c$ or $C2/c$ space group due to their close similarity. While $C2/c$ symmetry has been claimed experimentally [71, 89, 90], the determination based on DFT methods were differently suggested that $P2_1/c$ is energetically more favorable [31, 4,
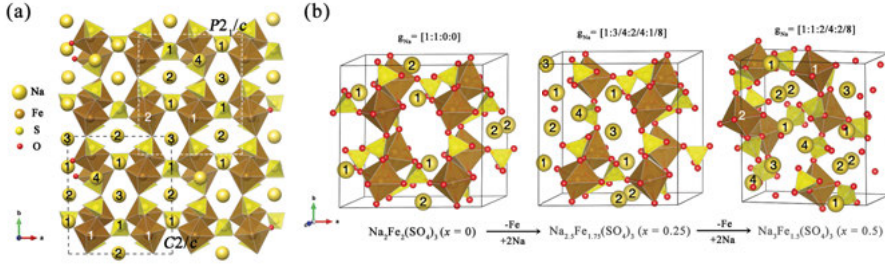
Figure 4.1. Crystal structures of alluaudite $Na_{2+2\delta}Fe_{2-\delta}(SO_4)_3$ (δ = 0, 0.25, 0.5). (a) The general differences in unit cells between $C2/c$ and $P2_1/c$ phases are illustrated in the [001] projection as marked by black and red dashed lines. The numbers 1-4 in black (1-2; white) show the inequivalent sites of Na (Fe) in each cell. (b) The minimum energy configurations in their preferable phases with the occupancy of Na sites are denoted by $g_{Na} = [g_{Na1}:g_{Na2}:g_{Na3}:g_{Na4}]$.

115]. NFSδ4.1(a) illustrates a comparison between alluaudite structures in $C2/c$ and $P2_1/c$ space groups along the c-axis described by the black and red unit lattices. Due to the narrower β angle, $P2_1/c$ lattice has a lower crystal symmetry along with a higher number of inequivalent sites for Fe, S, and O. Both structures contain four different Na positions, which are generally termed as Na1, Na2, Na3, and Na4 (or Na_{Fe}) sites.

4.1.1 Random-swapping algorithm

In order to find an optimal Na distributions for each NFSδ, we employ a generalized global minima searching, called a random swapping method. As the position of Na^+ ions are explicitly specified in these compounds, a set of Na positions can be directly sampled from all the possible sites using the weighted-random choice algorithm. With this algorithm, we sample fifty different initial configurations for each NFS and optimize them by using the low-accuracy SCF in order to screen out the high-energy configurations. Due to the slow SCF convergence for alluaudite compounds, each sampled configurations are relaxed within a certain number of iterations several times until the trend of their total energies becomes consistent. Eventually, the first ten lowest-energy configurations for each NFSδ are fully optimized with the optimal convergence accuracy. The configuration with the lowest total energy is regarded as a minimum energy configuration for each NFSδ.

4.1.2 Minimum energy configuration and Phase stability

Based on the random-swapping algorithm, we are able to explain the relation between Na distribution pattern (SDP) and energetics in the aspect of the Na occupancy (g_{Na}). This result also suggests that the site preference for

56

Table 4.1. *Calculated lattice parameters, energy gap (E_g), and formation enthalpy (ΔH^f) for $Na_{2+2\delta}Fe_{2-\delta}(SO_4)_3$ with δ = 0, 0.25, 0.5 in C2/c and P2$_1$/c primitive cells.*

Symmetry	δ	a (Å)	b (Å)	c (Å)	β (°)	V (Å^3)	E_g (eV)	ΔH^f (eV)
$C2/c$	0	12.70	12.78	6.62	115.09	972.00	3.38	-32.42
	0.25	12.66	12.90	6.60	115.49	973.41	3.27	-33.23
	0.5	12.68	12.94	6.68	115.66	986.99	3.45	-34.05
	0.25*	12.52	12.77	6.55	115.49	944.64	3.86	-34.76
$P2_1/c$	0	11.57	12.77	6.62	95.76	973.32	3.37	-32.41
	0.25	11.49	12.91	6.60	95.64	973.52	3.24	-33.23
	0.5	11.49	12.92	6.67	95.96	985.12	3.40	-34.06
	0.5*	11.35	12.83	6.59	95.68	954.74	4.06	-35.61

* Obtained within HSE06 functional.

Na^+ ion in a sequence of Na4 > Na1 > Na2 > Na3. Fig.4.1(b) shows the MECs for NFS0, NFS0.25 and NFS0.5 with g_{Na} = [1,1,0,0], [1,3/4,2/4,1/8] and [1,1,2/4,2/8], respectively. This prediction is in reasonable agreement with the g_{Na} for NFS0.25 reported in the experiments [89, 90]. Moreover, we investigate the phase stability by using the energy difference between $C2/c$- and $P2_1/c$-MECs. The result reveals that NFSδ tends to crystallize in the $C2/c$ phase for δ = 0 and 0.25 while the $P2_1/c$ phase is be energetically more favorable. However, the relative energies are in the order of thermal energy at room temperature (25 meV), the possibility of two-phase coexistence is anticipated. With the increasing δ, the lattice parameters for NFSδ show a negligible change as summarized in Table 4.1. The energy gap varies in a range of 3.2-3.5 eV for PBE+U, and 3.8-4.1 eV calculated using HSE06. Moreover, the higher lattice stability for the non-stoichiometric alluaudite phases is predicted due to the lower formation enthalpy.

4.1.3 Supercell configuration

In order to study the defect formations based on our calculations using planewave basis sets, it is crucial to employ a supercell approach to minimize the spurious interactions between defects and their periodic images. This can be done in a straightforward way for NFS0. Nevertheless, it is different for the non-stoichiometric phases as the Na4 positions and Na distribution in a larger lattice can be readjusted to further reduce the interactions due to the artificial periodicity.

We construct eleven different supercell configurations for NFS0.25 and NFS0.5 based on the g_{Na} for their MECs. To compare their stability, the relative energy between a sampled configuration N and the MEC in supercell is computed via $\Delta E_c = E_{tot}(N) - E_{tot}(MEC)$. Fig.4.2 shows the differences between each supercell configuration in terms of ΔE_c, an averaged $d_{Na4\text{-}Na4}$, and a sodium distribution pattern (SDP). The SDP for each NFSδ-N, where N de-
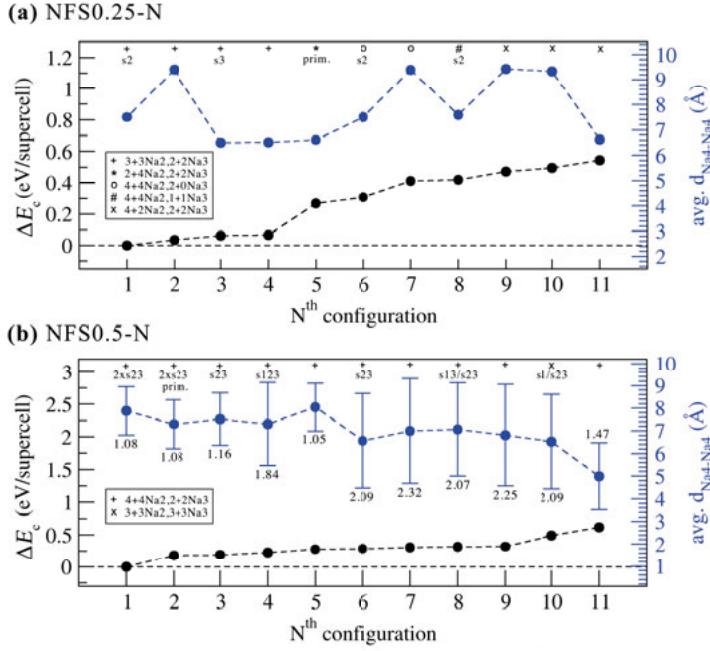
Figure 4.2. Structure-energetics correlation in NFSδ-N supercell configurations with (a) $\delta = 0.25$ and (b) $\delta = 0.5$. The relative energy (ΔE_c) and the Na4-Na4 interatomic distance ($d_{Na4\text{-}Na4}$) of each configuration are represented by black and blue dots, respectively. The standard deviation of $d_{Na4\text{-}Na4}$ in NFS0.5 is displayed by blue vertical bars together with the respective value at the bottom. Crystallographic details, i.e., Na+ arrangement and Na-Na connection for each configuration are described by different symbols and labels at the top.

notes a supercell configuration presented on the energy scale, is specified by different symbols at the top of each plot. This figure clearly proves that the supercells generated from the respective primitive MECs (marked by "prim."), namely NFS0.25-5 and NFS0.5-2, are not the actual MECs. The ΔE_c for these configurations are 0.27 and 0.18 eV/supercell, respectively. These values are high enough to cause the presence of a negative formation energy in alluaudite phases. In this regard, the supercell configuration is highly needed for the alluaudite compounds.

To see the structural differences, both MECs for NFS0.25 and NFS0.5 in primitive cell and supercell are shown in Fig.4.3, where the labels indicate the positions of Na$^+$ ion within the 4-Å vicinity of Na4 (blue atoms) and creates a link between two Na4 ions (shown with a bond). In addition to g_{Na}, the NFS0.25 and NFS0.5 supercell configurations are also identified by "$a+b$Na2∥$c+d$Na3", where a and b (c and d) denote the number of Na2 (Na3) ions in the respective channels as depicted in Fig.4.3. Moreover, we notice that the configuration will have a lower energy if two Na4 ions are coupled
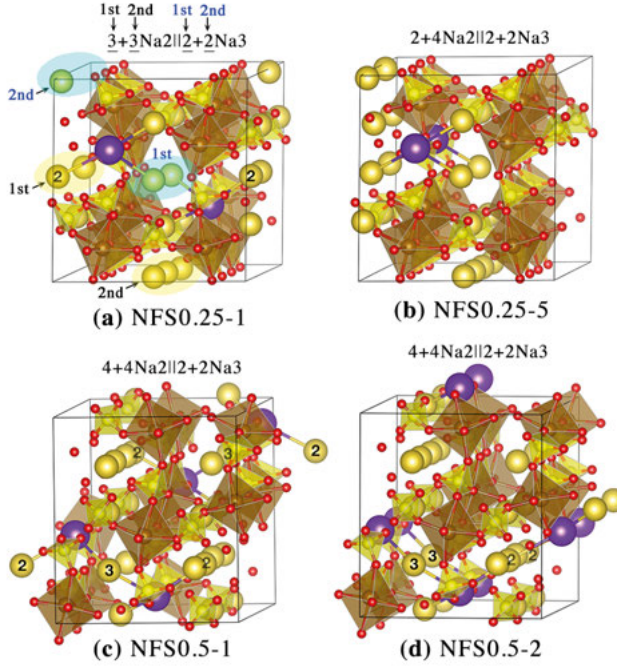
58

Figure 4.3. Minimum energy configurations of NFSδ-1 supercell with (a) $\delta = 0.25$ and (c) $\delta = 0.5$. The NFS0.25-5 and NFS0.5-2 configurations simulated from the primitive cell are shown in (b) and (d). The description of sodium distribution pattern is given at the top of each configuration as depicted in (a), and the blue atom represents Na4 position.

with the same Na^+ ion in diffusion channel. The configurations with such link are marked in Fig.4.2 by "si" where i indicates the type of the coupled Na^+ ion. Since NFS0.5 supercell contains four Na4 ions, we also consider the standard deviation of $d_{\text{Na4-Na4}}$ (SD) as represented by the vertical bar at $d_{\text{Na4-Na4}}$ data point along with its value in Fig.4.2(b). We conclude that NFS0.25-1 and NFS0.5-1 are the most stable configurations because their SDPs satisfy the criteria of long $d_{\text{Na4-Na4}}$, the presence of Na4-Na2-Na4 link, and low SD. Consequently, these two configurations are mainly used for the further investigations.

4.2 The duality of chemical potential diagrams

The stability condition for $Na_{2+2\delta}Fe_{2-\delta}(SO_4)_3$ is written as,

$$(2+2\delta)\mu_{\text{Na}} + (2-\delta)\mu_{\text{Fe}} + 3\mu_{\text{S}} + 12\mu_{\text{O}} = \Delta H^f[Na_{2+2\delta}Fe_{2-\delta}(SO_4)_3]. \quad (4.1)$$
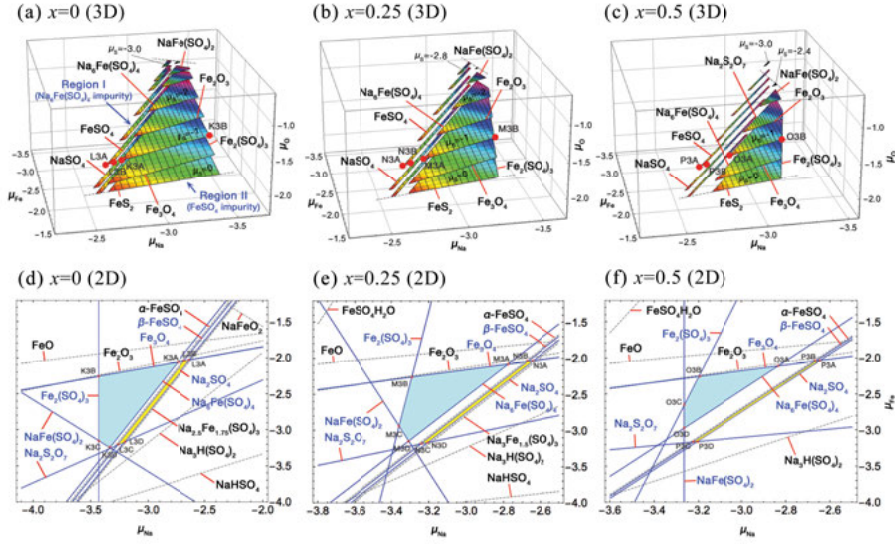
Figure 4.4. Chemical potential diagrams of NFSδ with $\delta = 0$, 0.25 and 0.5 represented in 3D-(a-c) and 2D-(d-f) perspectives. Two types of polygon slices in (a-c) indicate conditions where NFSδ is crystalized with $Na_6Fe(SO_4)_4$ precipitation (Region I) and $FeSO_4$ impurities (Region II) under a certain μ_S varied from S-rich condition to its minimal limit. The projection of these phase boundaries at $\mu_S = -1.0$ eV on a μ_{Na}-μ_{Fe} plane are represented in (d-f). The limiting compounds that enclose the stability region are denoted in blue and their interceptions represent equilibrium conditions.

By solving this condition with the constraints imposed by competing phases, we can define a range of atomic chemical potentials representing thermodynamic equilibrium conditions for all the three compounds. Differently from the previous chapter, we find that the Eq.4.1 cannot be solved if the constraints for the competing phases $Na_6Fe(SO_4)_4$ and $FeSO_4$ are both included. This result suggests an inevitable precipitation of either one of these secondary phases, which was consistently observed in the experiments [89, 31]. In this regard, both situations are considered and result in two separated phase boundaries for each NFS as depicted in Fig.4.4(a-c). The left- (region I) and a right-hand polygons (region II) represent the conditions that $Na_6Fe(SO_4)_4$ or $FeSO_4$ coexists with NFSδ, respectively. The narrower shape of the region I indicates the difficulty in controlling the chemical conditions to avoid $FeSO_4$. Therefore, the precipitation of $Na_6Fe(SO_4)_4$ impurity should be controlled more easily.

All the chemical potential diagrams show a similar description of the stability region both in terms of the limiting phases and the range of μ_i. However, they are differentiated by a different energy separation between two stability regions. As the energy separation is reduced following the reduction of δ, it suggests the possibility to minimize the impurity precipitations in NFS0 com-

pound. Here, the 2D-stability regions for X3 conditions are selectively plotted as a function of μ_{Na} and μ_{Fe} in Fig.4.4(d-f). The K3, M3 and O3 stability regions (blue region) are similarly enclosed by Fe_3O_4, $Fe_2(SO_4)_3$, $NaFe(SO_4)_2$, and $Na_6Fe(SO_4)_4$, whereas L3, N3, and P3 (yellow region) are defined by Fe_3O_4, $FeSO_4$, $Na_2S_2O_7$, and Na_2SO_4. At higher μ_S, FeS_2 is also in equilibrium with $NFS\delta$, while Fe_3O_4 is replaced by Fe_2O_3 at lower μ_S, Fe_2O_3.

4.2.1 The interpretation of oxygen chemical potential

According to the calculated chemical potential diagrams, all the $NFS\delta$ are stable within a range of μ_O from -2.00 eV (at S-rich condition) to -0.93 eV (at S-poor condition). Using Eq.**??**, we can determine μ_O as a function of T and P_{O_2} as plotted in Fig.4.5. This μ_O range corresponds to the temperature range of 410 - 1150 K under medium to ultra-high vacuum ($10^{-1} \leq P_{O_2} \leq 10^{-7}$ in Pa unit). since $NFS\delta$ were reported to undergo thermal decomposition above 750 K [12, 31], the conditions corresponding to $T > 750$ K are ruled out from consideration. The experimental synthesis condition at 650 K is theoretically simulated by $\mu_S = -1.0$ eV and -1.67 eV $\leq \mu_O \leq -1.37$ eV as highlighted in the yellow region. Interestingly, the chosen stability regions at $\mu_S = -1.0$ eV (in Fig.4.4(d-f)) are all described by the limiting phase of Fe_3O_4, which was also observed in experiments using solid-state synthesis. Moreover, our results also suggest the precipitation of Fe_2O_3 below 600 K (at $P_{O_2} = 10^{-7}$ Pa) in agreement with the outcomes of ionothermal synthesis [31]. Therefore, this strongly reinforces the reliability of our calculated chemical potential diagrams, allowing us to proceed in investigating the likelihood of defect formations in these three compounds.

4.3 Formation of small hole polarons and native defects

4.3.1 Site preference of defects

In each $NFS\delta$, an excess electron is delocalized in the conduction band (CB), whereas the positive E_{ST} of 0.25-0.35 eV indicates that an excess hole is preferably trapped by a lattice distortion around FeO_6 octahedron in the form of a small hole polaron. Similar to the kröhnkite cathode discussed in Chapter 3, native defects in $NFS\delta$ can be introduced as: (i) a complex binding with the different number of η^+ (or ξ^-) or (ii) an isolated defect in its elementary charge state without η^+. Apart from the charge state, it is of importance to find the most preferable site for defects. Referring to the dependency of Na occupancy pattern and lattice stability discussed in the section.4.1, the site preference for Na^+ ion is not only more favorable at Na2 and Na3 sites than Na1, but also prefers being situated close to Na4 due to the Coulombic attrac-
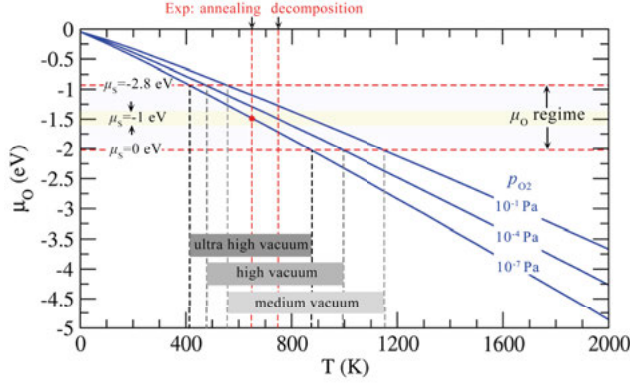
Figure 4.5. Oxygen chemical potential (μ_O) as a function of temperature T and its partial pressure P_{O_2} for alluaudite compound. Blue and yellow regions represent the range of μ_O at μ_S = -1.0 eV, respectively. The vertical dashed-lines in black and grey indicate the range of synthesis temperature, where μ_O corresponds to the thermodynamic boundary condition, under $P_{O_2} = 10^{-1}$ (medium vacuum), 10^{-4} (high vacuum), and 10^{-7} Pa (ultra high vacuum). The annealing temperature in the synthesis and the decomposition temperature from experiment are marked by red vertical dashed lines.

tion between Na_i^{1+} and Na_{Fe}^{1-}. Therefore, a positively charge defect is placed far from Na4, whereas a negatively charged defect is created nearby Na4 site.

In addition to the above criterion, the site preference of defect is thoroughly checked for all non-equivalent Nai and Fei sites. In this chapter, we primarily investigate the formation of V_{Na}, Na_i, Fe_{Na} and Na_{Fe} because they are expected to affect the capacity and ion transport of cathode materials. The general trend of defect site preferences is summarized as follows: (i) V_{Na}^{1-}: Na3 $\geq$ Na2 > Na1 > Na4, (ii) Na_i^{1+}: Na2 > Na3, (iii) Na_{Fe}^{1-}: Fe2 > Fe1 (in $P2_1/c$), and (iv) Fe_{Na}^{1+}: Na4 > Na1 > Na2 > Na3. Thus, these defects are created at their most preferable sites and further considered in defect calculation.

Amongst these defects, antisite defects are regarded as a source of the non-stoichiometry in alluaudite compounds. The above trend indicates that the Fe_{Na}^{1+} prefers to reside on either Na1 in NFS0 or Na4 in the other compounds rather than the sites along the diffusion channels. Thus, we expect that a fading capacity due to channel blockage is very unlikely in alluaudite phases. From our simulation perspective, Fe_{Na}^{1+} on Na4 site (Fe_{Na4}^{1+}) is regarded as a defect compensation for the formation of Na_{Fe}^{1-}, which controls the level of non-stoichiometry in this system, whereas Fe_{Na1}^{1+} might occur during desodiation reaction.

4.3.2 Defect formation energy

Fig.4.6 shows the defect formation energies for NFS0, NFS0.25, and NFS0.5 under the simulated experimental conditions under X3 conditions. We find that all the NFSδ compounds contain a high level of defect concentrations as the E^f at the FLP is quite close to zero (ca. below 0.2 eV) and even becomes negative under some equilibrium conditions. The unlikelihood of *n*- or *p*-type doping in NFSδ is expected as a shift of the FLP due to additional donor or acceptor dopants will result in a negative E^f. In this plot, we also include the possible formation of defect complexes as determined by the binding energy (in Eq.2.53).
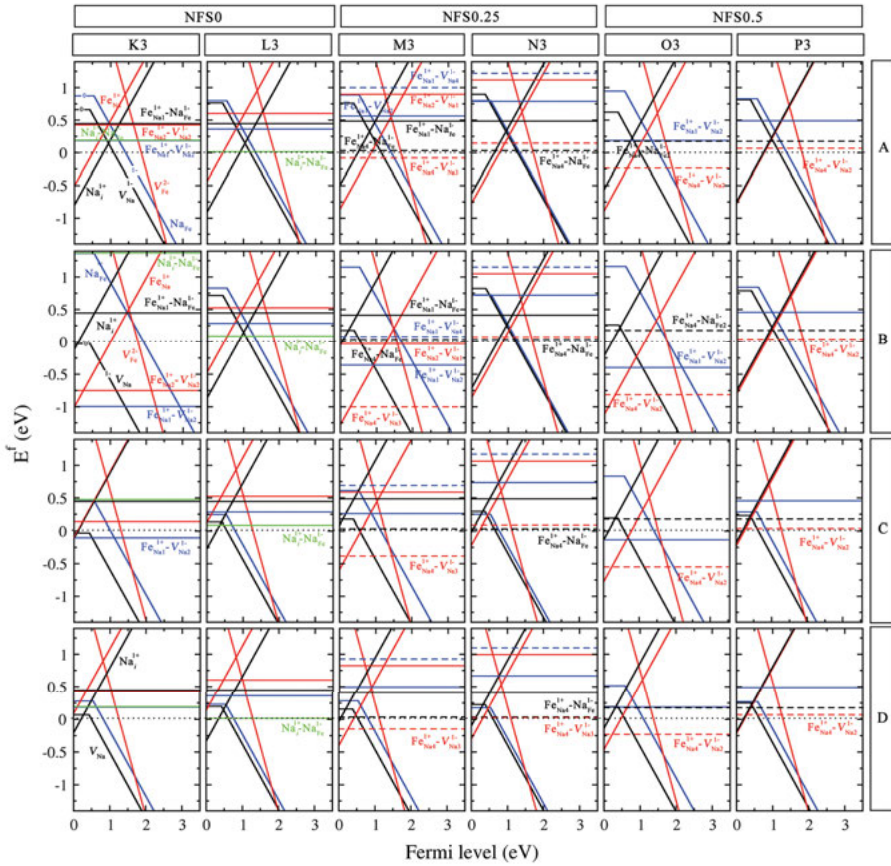

Figure 4.6. Defect formation energies (E^f) of NFSδ under equilibrium conditions at μ_S = -1.0 eV (X3 conditions). The description of these conditions is displayed in Fig.4.4. Plots in the left (right) panel for each compound represent the condition, where FeSO$_4$ (Na$_6$Fe(SO$_4$)$_4$) impurity is coexistent. To clearly identify the sign of E^f, a dotted line is referenced at E^f = 0. The E^f of complexes associated with Na4 (or Na$_{Fe}$) are expressed by dashed-lines.

Overall, we find that the formation of Fe_{Na}^{1+}-V_{Na}^{1-} and Na_i^{1+}-Na_{Fe}^{1-} defect complexes is dominant in these compounds, which highly depends on δ value and synthesis condition. The Fe_{Na}^{1+}-V_{Na}^{1-} complex inherently forms in NFS0.25 and NFS0.5 when $Na_6Fe(SO_4)_4$ impurity is precipitated (N3 adn P3 conditions), but spontaneously occurs in the conditions with $FeSO_4$ impurity (M3 and O3 conditions). Thus, the equilibrium conditions in the second case is not suitable for growing non-stoichiometric alluaudite phases. However, in these conditions, NFS0 can be synthesized under Na-excess condition (K3A and K3D conditions) with the likelihood formation of isolated Na_i^{1+} and V_{Na}^{1-}. These predictions can nicely explain the reason behind the experimental observation of $FeSO_4$ and $Na_6Fe(SO_4)_4$ impurities when $\delta < 0.25$ and $\delta > 0.25$, respectively. Moreover, our result suggest that the $Na_6Fe(SO_4)_4$ is possible to occur in NFS0 with a high concentration of Na_i^{1+}-Na_{Fe}^{1-} complex. Consequently, we identify this complex as an origin of the inherent non-stoichiometry in the alluaudite compounds.

4.4 Structural evolution during desodiation process

Instead of describing the non-stoichiometry by the δ factor, this factor will be denoted in the remaining sections by x and y parameters of N_xF_yS. This is for convenience in mentioning each compound during desodiation reaction. Considering the predicted criteria for the site preferences of Na (discussed in section.4.3.1), we can determine the MECs with different x and SDP, which occur upon desodiation reactions. During desodiation process, we find that the host structures are possible to undergo structural changes in three different ways as illustrated by half-desodiated $N_{1.25}F_{1.75}S$ phase in Fig.4.7(d-f). The first one is a typical structural change in lattice parameters in the original lattice geometry (shown in Fig.4.7(a-c)). In this case, each compound behaves like a solid solution during charging/discharging process.

When distorting the desodiated crystal lattices in the original phase, the structures tend to get distorted and transform into two different phases, namely d-phase and t-phase. For d-phase, there is a distinct separation of Fe_2O_{10} dimers into two FeO_5 trigonal bipyramid. As x reaches zero, the d-phase encounters a phase transformation into the t-phase with a remarkable elongation along c axis and a wider lattice angle of β and γ. It leads to an rearrangement of FeO_5 trigonal bipyramid into distorted octahedral FeO_6 that connects with SO_4 via an edge sharing. Structural changes for each compound in different phases are systematically depicted in Fig.4.8. We find that d-phase will not emerge at $x > 2.25$ for $N_xF_{1.75}S$ and $x > 1.5$ for $N_xF_{1.5}S$. This is because the higher amount of Na^+ ions in alluaudite structures enlarge the diffusion channels and push two FeO_5 units back to reform Fe_2O_{10} bi-octahedron. This result suggests that non-stoichiometry can reduce the degree of structural change and enhance the structural reversibility.
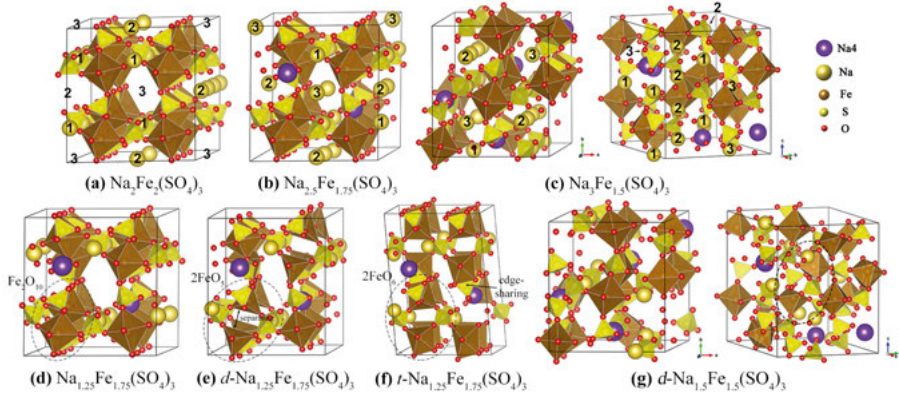
Figure 4.7. Minimum energy configurations of $Na_xFe_y(SO_4)_3$ in $C2/c$ symmetry for $y = 2$ and 1.75, and in $P2_1/c$ for $y = 1.5$ illustrated in (a-c) pristine and (d-h) distorted alluaudite phases (*d*- and *t*-phases), where structural changes in each phase are indicated in the dashed-circles. A number labeled on Na atoms indicates the type of Na lattice sites, namely, Na1, Na2 and Na3.

4.5 Formation energy of desodiated compounds

According to the obtained MECs of desodiated N_xF_yS, a sequence of sodium extractions in the three compounds is similarly occurred at Na3 site, followed by Na2, Na1 and Na4 sites. This trend can be simply concluded with respect to x and the theoretical specific capacity (C) in Fig.4.9(a-c). The specific capacity is calculated using the following equation,

$$C = \frac{F \cdot \Delta x}{3.6m} = \frac{2.68 \times 10^4 \cdot \Delta x}{m}, \tag{4.2}$$

where F is the Faraday constant, δx is the number of extracted Na^+ ions and m is the molar mass of the corresponding cathodes.

In order to compare the relative stability of N_xF_yS in three different phases, we compute the formation energies of each configuration (ΔE) using Eq.2.58 and plotted them with respect to their corresponding x as displayed in Fig.4.9(d-f). At the early stage of charging, we find the ΔE for *d*- and *t*-phases are higher than that for the original ones, indicating an unlikely structural rearrangement. However, these phases become energetically more favorable after the half-desodiation process (as indicated in red shaded regions), when Na^+ ion is first extracted from Na1 site. This strongly proves the crucial role of Na1 as a binding pillar in the alluaudite structures. Moreover, the *d*-phase is possibly nucleated in $N_xF_{1.75}S$ before half-desodiation at $x = 1.5$ since the ΔE is different from the one for the original phase merely within the scale of thermal energy at room temperature. Although *t*-phase is clearly more stable than the other phases after the half-desodiation, it should form only at the nearly full desodiation due to the expected high activation energy for substantial struc-
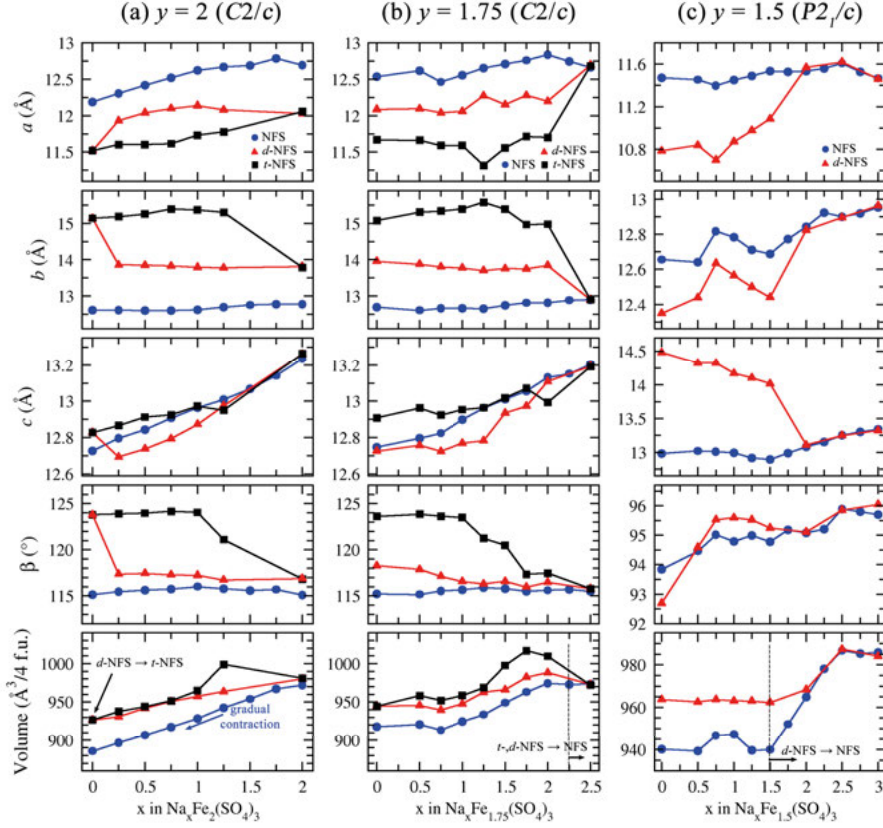
(a) $y = 2$ (C2/c) **(b)** $y = 1.75$ (C2/c) **(c)** $y = 1.5$ ($P2_1/c$)

Figure 4.8. Structural changes for $Na_xFe_y(SO_4)_3$ compounds during intercalation where (a) $y = 2$, (b) $y = 1.75$ and (c) $y = 1.5$ in their preferable phases. Solid and dashed lines represent the changes in the original and distorted structures, respectively.

tural rearrangement. As more than half of Na were usually extracted in the experiments, we highly expect that d-phase should partially occur in the operating cathode, while the t-phase is possibly observed if the cell is further charged.

4.6 The implication of voltage profiles and sodium intercalation mechanism

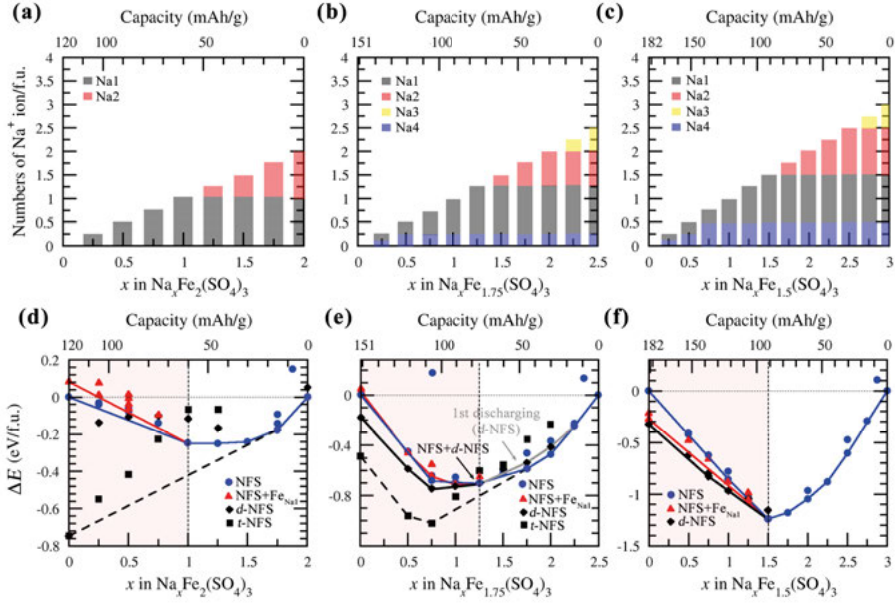The average intercalation potential is calculated using Eq.2.57 for the following reaction,

$$Na_{x_2}Fe_y(SO_4)_3 \iff Na_{x_1}Fe_y(SO_4)_3 + \Delta x \cdot Na^+ + \Delta x \cdot e^-, \tag{4.3}$$
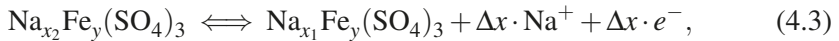
Figure 4.9. A sequence of sodium intercalation mechanism in $Na_xFe_y(SO_4)_3$ cathodes where (a) $y = 2$, (b) $y = 1.75$ and (c) $y = 1.5$. The bar color is to differentiate the possible Na sites, namely Na1 (grey), Na2 (red), Na3 (yellow) and Na4 (blue). (d-f) Their respective formation energies with respect to their fully charged and discharged configurations. Data points on each line represent the possibly metastable configurations with different Na content (x) upon desodiation reaction.

where $\Delta x = x_2 - x_1$. We obtain the averaged OCV of the half-desodiation as 3.88, 3.81 and 3.75 V for N_xF_yS with $y = 2$, 1.75 and 1.5, respectively. In order to determine voltage profiles during desodiation, a convex hull is constructed on the basis of the relative formation energies between the fully sodiated and desodiated compounds in the original phase. According to the possible pathways of phase transitions (including the case of Fe migration to Na1 site), we envisage up to four different convex hulls as separately depicted in Fig.4.9(d-f). Using Eq.2.57, the intercalation voltage is calculated by considering x_{max} and x_{min} based on the x of low-formation energy configurations on each convex hull. Hence, we obtain the voltage profiles for each N_xF_yS as shown in Fig.4.10. This figure is considered together with the results of the density of states. It indicates that the maximum number of Na^+ ions that can be extracted without an oxidation reaction on oxygen atoms are 2, 0.75 and 1.5 per formula unit (represented by dashed-lines in Fig.4.10).

Even though N_xF_2S is electrochemically possible for the full desodiation, which results in the theoretical C of 120 mAh/g, the presence of t-phase at the end of full desodiation reaction is predicted to cause a steady voltage at 3.77 V and a huge irreversible capacity. Thus, N_xF_2S is not a potential candidate as widely expected. As for the other N_xF_yS, the voltage is increased above
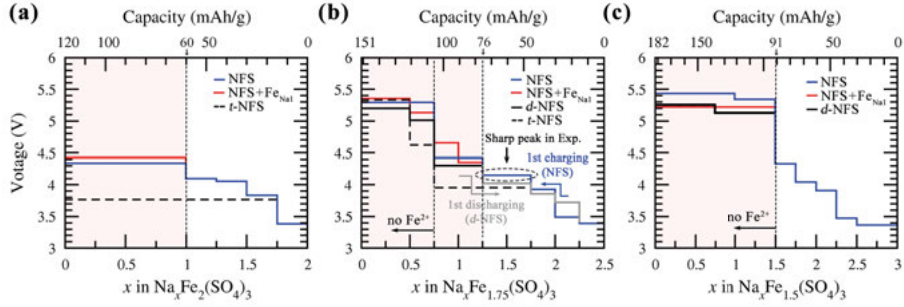
Figure 4.10. Voltage profiles for $Na_xFe_y(SO_4)_3$ cathodes in the pristine phase (blue solid line) and with the occurrence of *d*-phase (black solid line), *t*-phase (black dashed line) and Fe diffusion (red solid line). The red area is where the original NFS phase is less stable than any other phases.

the limit of current electrolyte stability window for SIBs at 4.5 V (for non-aqueous $NaClO_4$) after the full utilization on $Fe_{2+/3+}$ redox reaction. We find that the capacity for $N_xF_{1.75}S$ can reach 107 mAh/g in agreement with experiment, however, this will lead to the nucleation of *d*-phase. As the *d*-phase is expected to form before half-desodiation, the nucleation of this phase should be associated with the calculated voltage at 4.15 V and can be attributed to the sharp peak at 4.06 V observed in the dQ/dV plot [90, 31]. Regarding $N_xF_{1.5}S$, it is predicted to deliver the capacity of 91 mAh/g (equivalent to the energy density of 342 Wh/kg), close to the $N_xF_{1.75}S$ case, via the half-desodiation reaction. More importantly, there is no structural rearrangement during the reaction. Therefore, our results suggest that $N_xF_{1.5}S$ emerges as an alternative cathode competitive to the well-known $N_xF_{1.75}S$ due to the high energy density and an excellent structural reversibility.

5. Polyanionic electrodes for Hybrid Supercapacitors

This chapter is devoted to polyanionic cathodes for hybrid supercapacitor applications. We particularly study two different cathodes, namely NaMPO$_4$ and MMoO$_4$ (where M = Mn, Co and Ni) by using a combined theoretical and experimental approach. However, the results and discussion provided in this chapter are primarily based on the first-principles investigations. The main objectives is to study the effect of transition metal substitution on crystal structure, phase stability, electronic properties and redox behavior in order to explain experimental findings and identify the electrochemical storage mechanism in these two types of HSC cathodes.

5.1 Case I: NaMPO$_4$

The olivine LiFePO$_4$ has been considered a promising cathode material in LIBs. The substitution for Li in olivine by Na produces the analogue, but exists in two distinct polymorphs, namely triphylite (t) and maricite (m), depending on the synthetic temperature (300-550 °C). Although NaFePO$_4$ was claimed to be not viable as a cathode material for battery applications in non-aqueous media [120], we find that this material is electrochemically active when using an aqueous NaOH electrolyte and suitable for hybrid supercapacitor applications.

First, we focus on NaNiPO$_4$ in both phases. In the experimental part, the triphylite and maricite polymorphs are prepared by a facile synthesis at 400 and 550 °C, respectively. We find that the t-NaNiPO$_4$ vs. AC in 2 M NaOH exhibits the maximum specific capacitance of 125 F/g and 85 F/g respectively, at 1 A/g, as well as an excellent cycling stability with retention of 99% capacity up to 2000 cycles. The m-NaNiPO$_4$ showed 70 F/g with a significant drop in capacity after just 50 cycles. To understand the role of NaNiPO$_4$ polymorphs in the redox reactions, we perform DFT calculations for both polymorphs. The crystal structures of m- and t-NaNiPO$_4$ adopt *Pnma* space group (no. 62) as illustrated in Fig.5.1. As they are energetically favourable in anti-ferromagnetic spin configuration, the stable magnetic orientation is determined and shown in the figure. We find that the predicted band gap using HSE06 functional is 4.94 and 5.03 eV for m- and t-phases, respectively, which are much larger than the ones obtained within PBE functional (0.76 and 0.86 eV), indicating a severe self-interaction error in this system. The electronic structures of
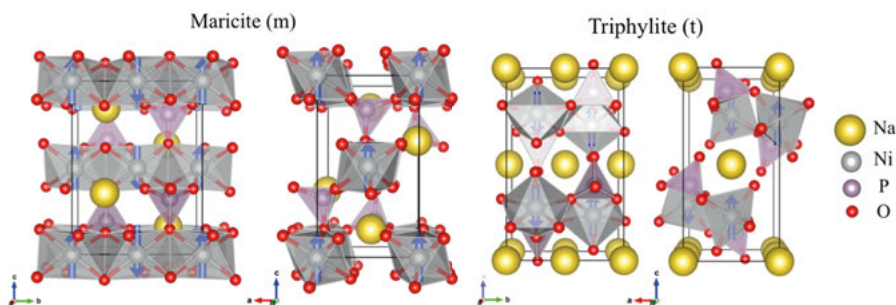
Figure 5.1. Crystal structures and magnetic orientation of NaNiPO$_4$ polymorphs. *m*-(left) and *t*-NaNiPO$_4$ (right) in their antiferromagnetic configurations. The Ni magnetic moments are depicted by blue arrows.

both phases reveals a similar redox activity of Ni$^{2+/3+}$, which is Ni^{2+} high spin state. Although *m*-NaNiPO$_4$ has a smaller E_g, such small difference should not make an explicit difference on their inherent electronic conductivity. Since the high storage capability corresponds to the intrinsic electronic conductivity, it implies that regardless of the presence of Na-diffusion channels, the observed high performance for triphylite sample should not be originated from its electronic conductivity itself. However, this should be attributed to the intercalation pseudocapacitve behavior due to the viable diffusion pathways in *t*-NaNiPO$_4$.

Even though the *t*-NaNiPO$_4$ shows a better electrochemical performance as compared to *m*-NaNiPO$_4$, it is not stable and can solely be synthesized by chemical or electrochemical Li-Na exchange process, making it less attractive. In order to improve the performance for the maricite NaNiPO$_4$, a mixed-NaMn$_{1/3}$Co$_{1/3}$Ni$_{1/3}$PO$_4$ is synthesized by replacing Ni with a mixing of Mn$_{1/3}$Co$_{1/3}$Ni$_{1/3}$. Based on our experimental results, it shows that the mixed-compound in a nonaqueous electrolyte shows redox peaks in the cyclic voltammograms and asymmetric profiles in the charge-discharge curves while exhibiting a specific capacitance of 40 F/g and a high electrochemical reversibility.

To model the mixed-NaMn$_{1/3}$Co$_{1/3}$Ni$_{1/3}$PO$_4$ structure, we construct a number of $3\times1\times1$ supercell of 4 based on the criterion of different *M-M* distances. The first three lowest total energy configurations are only considered and termed as C1, C2 and C3. We find that the minimum energy configuration (C3) can be obtained when *M* atoms in the same species are placed far to each other. The average *M-M* distance for C1, C2 and C3 are 3.379, 3.383 and 5.891 Å, respectively. Moreover, the homogeneity of the charge distribution of the C3 configuration also makes it more stable than C1 and C2 analogues. From the projected density of state of this mixed compound shown in Fig.5.2, we find that the VBM and CBM are mainly contributed by Ni-3*d* and Mn-3*d* orbitals, indicating the redox activity of these *M* in this compound. Due to
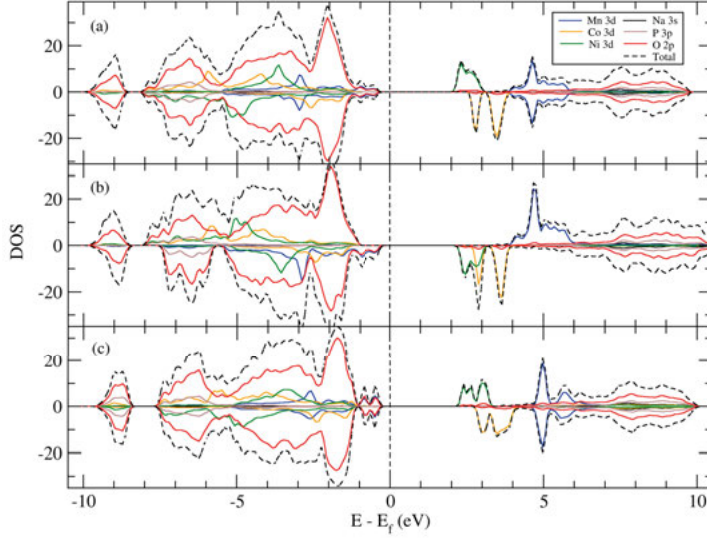
Figure 5.2. The total DOS (dash line) and orbital-decomposed DOS for each element (solid line) for the (a) C1, (b) C2, and (c) C3 configuration of *m*-NaMn$_{1/3}$Co$_{1/3}$Ni$_{1/3}$PO$_4$ obtained from GGA+*U* calculations.

the smaller E_g (2.24 â 2.32 eV) of *m*-NaMn$_{1/3}$Co$_{1/3}$Ni$_{1/3}$PO$_4$ as compared to NaNiPO$_4$, this compound is predicted to have an improved electronic conductivity.

5.2 Case II: *M*MoO$_4$

Transition metal molybdates (*M*MoO$_4$) have attracted great interest in the field of energy storage devices, such as batteries and supercapacitors [116, 100, 118]. This is primarily due to the environmental safety and enhanced electrochemical properties compared to their corresponding oxides. Although the electrochemical studies for molybdates as cathodes have been reported, no work has been reported for a range of transition metal cations (*M*MoO$_4$, where *M* = Mn, Ni or Co) outlining the advantages and limitations for each of the systems from chemical aspects that are suitable for hybrid devices. In this regard, we employ a combined theoretical and experimental approach to investigate the effect of *M* transition metal substitution on crystal structures, electronic properties and electrochemical performance of the molybdate compounds.

Generally, the crystal structure of *M*MoO$_4$ adopt the *C*2/*m* monoclinic space group in two different polymorphs. These consist of (i) α-phase, which is isotypic with α-CoMoO$_4$-type structure, and (ii) β-phase, which refers to α-MnMoO$_4$-type structure. For this reason, *M*MoO$_4$ in both phases are studied in order to perceive their relation between energy and structural informa-
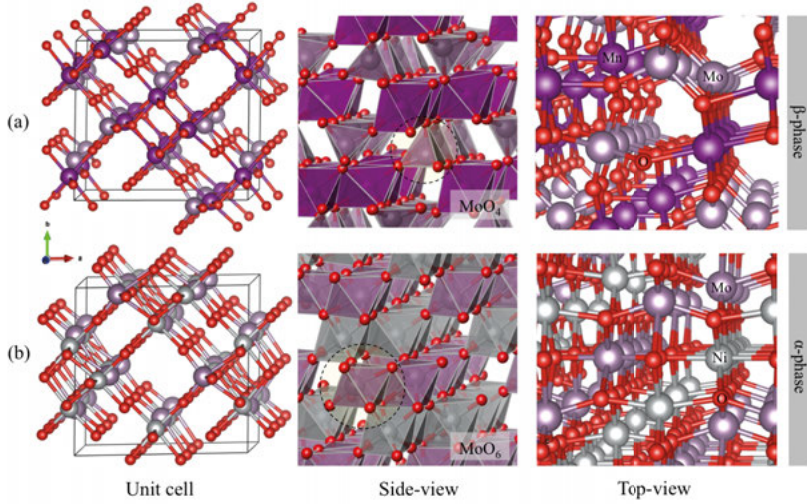
Figure 5.3. Monoclinic structures of MMoO4 (M = Mn, Co, and Ni) molybdate framework. The upper (a) and lower (b) rows display β-phase of MnMoO$_4$ and α-phase of NiMoO$_4$, respectively, in different perspectives. Side and top views are projected along the [$\bar{1}1\bar{2}$] direction and b-axis of the corresponding unit cells. The unit of MoO$_x$ (x = 4 and 6) is indicated by dashed circles in side-view perspective.

tion. All the compounds are optimized using DFT method within PBE+U functional, where U_{eff} for Mn, Co and Ni are 3.9, 3.4 and 6.0 eV, respectively. Their crystallographic data are shown in Table 5.1. Our calculated lattice parameters and E_g for each compound is well-corresponded with the corresponding experimental values. We find that the cell volume and E_g for α-phase are usually smaller than those for β-phase. This is attributed to the anisotropic coordination of Mo which forms MoO$_6$ octahedra in α-phase but becomes MoO$_4$ tetrahedra in β-phase as illustrated in Fig.5.3. The structural distortion in β-phase leads to the presence of an additional channel for intercalation mechanism as shown in the case of MnMoO$_4$.

Fig.5.4(a) shows the decreasing trend of M-O and M-M bond distances from Mn- to Ni-based compounds. The presence of MO$_x$ Jahn-Teller (JT) distortion is observed in all the compounds and described by the distortion coefficient ($\Delta(M$-O)) which is computed from Eq.3.3. We find that the JT distortion is smallest in NiMoO$_4$ and is expected to be associated with the redox reaction. Furthermore, the phase stability is determined by the total energy difference between α- and β-MMoO$_4$, which is written as $\Delta E_{tot} = E_{tot}(\alpha)$ - $E_{tot}(\beta)$. The ΔE_{tot} is obtained with different exchange correlation functionals as shown in Fig.5.4(b). We find that an inclusion of U_{Mo} is highly required for the molybdates since it provides the results that CoMoO$_4$ and NiMoO$_4$ crystallize in α phase while MnMoO$_4$ prefers forming in β phase, in agreement with our experimental observation. This is because the strongly localized elec-

Table 5.1. *Crystal structural parameters, band gap (Eg), M^{2+} spin moments $|\mu_M|$, and cohesive energy (E_{coh}) for $MMoO_4$ (M = Mn, Co, and Ni) in α and β phases.*

| M	phase		a (Å)	b (Å)	c (Å)	β (°)	V (Å^3)	E_g (eV)	$|\mu_M|(\mu_B)$	E_{coh} (eV)
Mn	α	cal	10.08	9.18	7.86	113.5	667.4	1.98	4.60	-10.66
	β	cal	10.64	9.70	7.25	105.7	720.3	2.57	4.62	-10.74
		exp	10.47	9.52	7.13	106.0	683.7	1.96		
Co	α	cal	9.81	8.97	7.73	113.8	621.9	2.17	2.73	-8.89
		exp	9.52	8.86	7.75	113.2	600.9	2.17		
	β	cal	10.39	9.41	7.11	106.9	665.5	2.66	2.74	-8.86
		exp	10.20	9.18	7.16	106.9	641.5			
Ni	α	cal	9.69	8.88	7.71	113.9	606.5	2.75	1.80	-8.84
		exp	9.54	8.74	7.66	113.6	585.0	2.81		
	β	cal	10.28	9.29	7.07	106.9	645.8	3.20	1.81	-8.83
		exp	10.15	9.24	7.10	107.1	636.5			
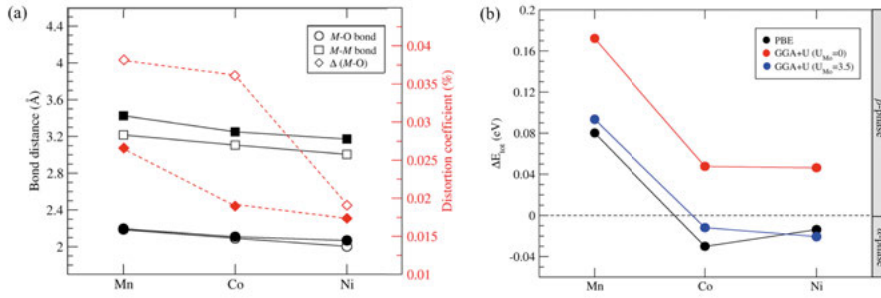
Figure 5.4. (a) Comparison of the *M*-O and *M-M* distances (black, left axis), and average distortion coefficients of *M*-O octahedra (red, right axis) of *M*-based molybdates (*M* = Mn, Co, and Ni). The empty and filled symbols indicate such parameters of α- and β-phases, respectively. (b) Total energy difference between α- and β-phases calculated with PBE, GGA+U (UMo = 0 eV), and GGA+U (U_{Mo} = 3.5 eV). The negative (positive) value is corresponding to α-phase (β-phase).

trons on Mo-site cannot be properly described within the standard exchange correlation functional.

In order to investigate the electrochemical behavior, the projected density of states are calculated and shown in Fig.5.5. We find that Mo in both phases are not associated with the redox activity due to an insignificant electron contribution near the VBM. The electron contribution at the VBM is the most prominent in $NiMoO_4$, however, it is mostly contributed from oxygen, suggesting the possibility for $NiMoO_4$ to undergo the oxidation reaction and structural changes. For $MnMoO_4$, the redox activity is predicted to be inferior to the other compounds. These results are reasonably consistent with the trend of an initial capacitance measured in experiment as depicted in Fig.5.6. This figure shows that hybrid device comprising $NiMoO_4$ vs AC exhibits excellent electrochemical performance having the specific capacitance 82 F/g at a current
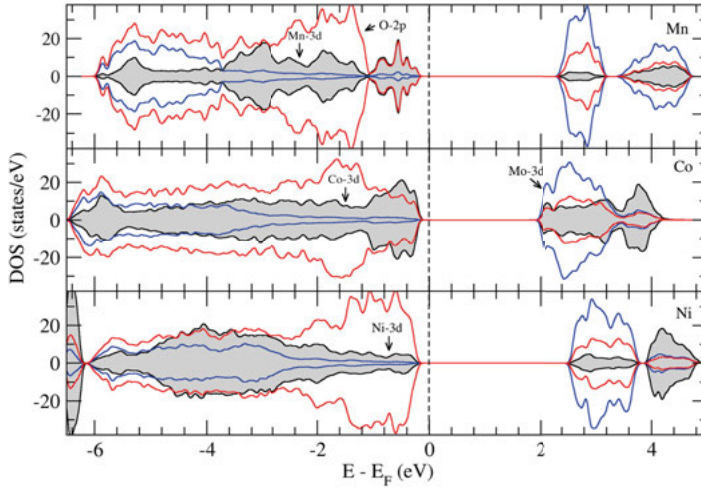
Figure 5.5. Projected density of states (PDOS) for $M\text{MoO}_4$ (M = Mn, Co, and Ni). Black, blue, red, and brown lines represent the contribution of M, Mo, and O, respectively. The dashed line shows the Fermi level aligned at 0 eV.

density of 0.1 A/g, but the cycling stability require a significant improvement. We find that an implication of the cohesive energy (E_{coh}) can reasonably explain the trend of cycling stability in $M\text{MoO}_4$.

Moreover, we find that the weak inductive effect is attributed to the low redox potential in $M\text{MoO}_4$. This is due to the ionic and covalent behavior of Mo-O and M-O bonds, respectively. The difference in redox potential for $M\text{MoO}_4$ can be explained by the strength of the Madelung electric field on M ions. The shorter distance between two M cations reduce the magnitude of such electric field, resulting in a higher redox potential [43]. Consequently, the shortest M-M distance in NiMoO_4 is identified as the reason behind the higher redox potential as compared to the other molybdates.

In order to improve the electrochemical performance of $M\text{MoO}_4$, a new ternary material $\text{Mn}_{1/3}\text{Co}_{1/3}\text{Ni}_{1/3}\text{MoO}_4$ (termed as MCNMoO_4) is synthesized. From our experimental results, we find that this mixed compound shows a compromise between the high specific capacitance of NiMoO_4 and high cycling stability of MnMoO_4 by offering a specific capacitance of 58 F/g at a current density of 0.5 A/g and an enhanced reversibility with cycling efficiency of 90% after 2000 cycles as shown in Fig.5.6. In this part, the DFT method is employed to investigate its crystal structure and electrochemical behavior of this new ternary compound. We perform a generalized special quasi-random structure (SQS) method implemented in USPEX[123] to explore the MCNMoO_4 structure [37]. A candidate structure is randomly generated by applying a permutation operator to randomly swap the positions of M ions. All the obtained structures can be distinguished by types of the M species in
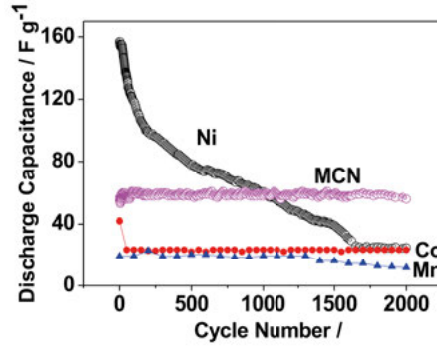
Figure 5.6. The experimental measurement of cycling profiles of MCNMoO$_4$ in comparison with MnMoO$_4$, CoMoO$_4$, and NiMoO$_4$.

Table 5.2. *The geometric details of all optimized Mn$_{1/3}$Co$_{1/3}$Ni$_{1/3}$MoO$_4$ structures calculated within PBE and HSE06 functionals. The relative total energy (ΔE) is referenced to the total energy of the B1 configuration.*

E_{xc}	Conf.	a (Å)	b (Å)	c (Å)	β (°)	V (Å^3)	ΔE (eV)
PBE	A1	9.72	8.85	23.42	114.23	76.55	0.21
	A2	9.71	8.85	23.42	114.21	76.51	0.24
	A3	9.69	8.84	23.46	114.28	76.34	0.42
	A4	9.66	8.83	23.44	114.15	75.95	1.55
	B1	10.32	9.36	21.36	106.90	82.25	0.00
	B2	10.28	9.34	21.41	106.65	82.05	0.10
	BA	9.68	8.83	23.48	114.19	76.22	0.93
HSE06	A1	9.76	8.91	23.22	113.82	76.93	1.19
	B1	10.35	9.37	21.30	106.50	82.56	0.00

four binding octahedral MO$_6$ unit ($4MO_6$) as demonstrated in Figs.5.7(a) and (b).

Table 5.2 shows crystal lattice parameters and total energies of chosen configurations obtained from PBE and HSE06 functionals. The total energy difference (ΔE) is referenced with the total energy of B1 as expressed by $\Delta E = E_{tot}(i) - E_{tot}(B1)$. The structures in α and β phases are represented as Ai and Bi (where i is a configuration number), respectively, while the BA configuration is the β-phase structure transformed from α phase after geometry optimization.

Fig.5.7(c) shows that the A1 and B1 configurations, the most stable configuration for each phase, prefer forming in the MCNMoO$_4$ that contains only one M species in each of $4MO_6$ unit. Based on both PBE and HSE06, we conclude that MCNMoO$_4$ should form in the β phase. The volume of MCNMoO$_4$ is less than that of α-MnMoO$_4$, implying the higher surface area of MCNMoO$_4$. This explains why an initial specific capacitance for MCNMoO$_4$ is lower than the Ni-based system while still higher than the Mn-based molybdate as re-
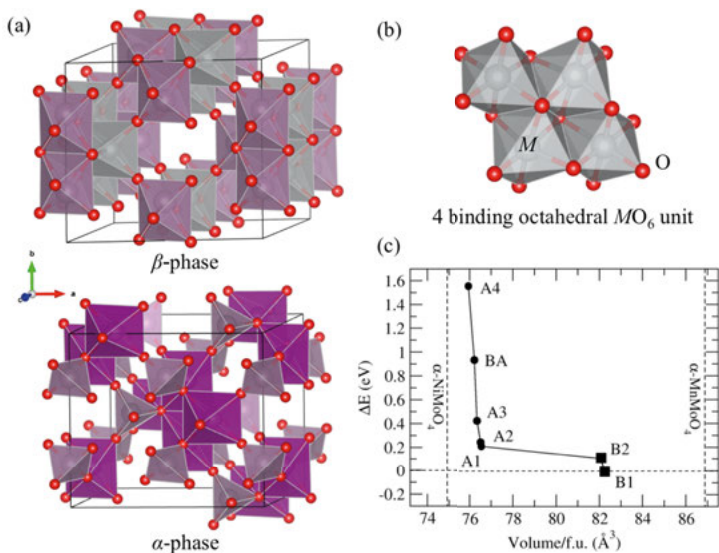
Figure 5.7. (a) Illustration of α- and β-MMoO$_4$ (b) A group of four binding octahedral MO$_6$ components in metal molybdate structure. (c) A comparative plot showing a relative total energy for each considered configurations against their corresponding volumes per formula unit.

flected in Fig.5.6. Based on the density of states, we reveal that Mn is the main source of the redox activity of MCNMoO$_4$.

6. Summary

In this thesis, the framework of the DFT is employed to study and predict properties in polyanionic cathode materials for Na-ion batteries and hybrid supercapacitors. Owing to the inductive effect in polyanionic compounds, PBE+U functional is mainly employed for all the electronic structure calculations to describe the highly localized electrons properly. This thesis are divided in five chapters. The first chapter addresses the importance and background of energy storage, along with the motivations of this thesis. In Chapter two, we describe a brief detail about the DFT formalism and all other theoretical methods employed in this thesis. Subsequently, all the achieved results are given in the last three chapters, which can be summarized as follows.

Chapter three primarily aims at unveiling the Na intercalation mechanism in kröhnkite-type $Na_2Fe(SO_4)_2 \cdot 2H_2O$ cathode material (termed as NFS2H). The journey to this goal begins with the fundamental understanding in bulk properties of NFS2H. Hydrogen bonds associated with structural H_2O units are found to have a crucial impact on structural stability and charge transfer within the inter- and intra-pseudolayers. While the full desodiation is not applicable due to the limit of electrolyte potential window, we obtain a higher voltage for half-desodiation at 4.01 V compared to the experimental one (3.25 V). This is attributed to an unknown structural change induced by water adsorption in NFS2H. From the electronic structure, although a wide-band gap character with flat band edges implies a poor electronic conduction in NFS2H, this property is predicted to rather depend on small hole polarons, which shows the favorable formation and fast hopping process. Based on vacancy-assisted diffusion and NEB method, the Na-ion intercalation mechanism is found to moderately occur along $[01\bar{1}]$ direction with a migration energy of 1.16 eV. Due to this high migration energy, native defects are expected to govern the fast-ion diffusion as experimentally reported.

In order to examine the defect formations in NFS2H, we systematically determine chemical potential diagrams under its thermodynamic equilibrium conditions. The calculated diagrams reveal the existence of secondary phases in agreement with experimental observations and also provide a suitable range of atomic chemical potentials for the crystal growth of NFS2H cathode. Since NFS2H is merely synthesized in liquid solution, the pH value for synthesis condition is approximated by using the chemical potential of hydrogen The result suggests the acidic growth condition ($2.0 < pH < 6.4$). Subsequently, the defect formation is investigated under each equilibrium condition at different pH values. The dominant defects in NFS2H are revealed to be either of Fe_{Na},

V_{Na} or Na_{Fe}, and their concentrations can be manipulated by tuning the pH value of the precursor solution. The Fe_{Na} channel blockage is dominant at low pH but can be suppressed at pH between 4.0 and 5.6, where V_{Na} and Na_{Fe} become predominant. These two defects can also induce small hole polarons, resulting in an enhanced electronic conductivity under weak acidic condition. Here, we show that the presence of Na_{Fe} is beneficial for the ionic diffusion as it provides an alternative pathway that bridges each $[01\bar{1}]$ diffusion channel, which helps mitigating the defect hindrance issue. Moreover, it also enables a faster diffusion as compared to the one along the major diffusion channel. Therefore, this mechanism is a key factor for the improved ionic conductivity observed in nanostructured NFS2H.

In Chapter four, we investigate the non-stoichiometric behavior in alluaudite-type $Na_{2+2\delta}Fe_{2-\delta}(SO_4)_3$ cathode for $\delta = 0$, 0.25 and 0.5 (termed as N_xF_yS where $y = 2$, 1.75 and 1.5). The random swapping method is employed to find their minimal energy configurations and reveal a correlation between energetics and Na distribution pattern in this class of material. This result reveals the site preference for Na in a sequence of Na4 > Na1 > Na2 > Na3 according to their Na intercalation mechanisms. The use of supercell is highly required in order to properly describe the non-stoichimetry in N_xF_yS. Next, the chemical potential diagrams are constructed for each compound to perceive the difference in the thermodynamic perspective and define the range of chemical potentials for defect energy calculations. Our calculated diagrams nicely prove the inevitable precipitation of $Na_6Fe(SO_4)_4$ and $FeSO_4$ phase impurities as commonly observed in experiments. Interestingly, it also points out the possibility to minimize the impurity concentrations in each N_xF_yS, especially for N_2F_2S.

Based on the obtained chemical potentials, defect formation energy determination is carried out according to different experimental conditions. Overall, all the N_xF_yS show a high concentration of native defects, which might become spontaneous under some conditions. This result is well matching with the experimental tendency for impurity precipitation. Moreover, it reveals an unlikely formation of channel blockage and the formation of Fe_{Na}^{1+}-V_{Na}^{1-} and Na_i^{1+}-Na_{Fe}^{1-} dominant defect complexes in these compounds. We eventually identify Na_i^{1+}-Na_{Fe}^{1-} as an origin of the inherent non-stoichiometry because it dominantly occurs only in the stoichiometric compound.

Furthermore, redox potential profile and Na intercalation mechanism are studied for each compound. We unveil the possibility of structural evolution during desodiation, particularly after an initial extraction of Na1. Firstly, N_xF_yS compounds undergo the partial distortion, leading to a lattice expansion and a structural rearrangement from Fe_2O_{10} bi-octahedra into two FeO_5 trigonal bipyramid (called d-phase). When Na^+ ions are further removed, the crystal lattice is significantly enlarged and transformed into another C2/c structure called t-phase. These two phases are expected to show an inferior

performance of Na-ion diffusion as compared to the original one, while the electrochemical behavior is barely altered due to their similar electronic structures. Subsequently, redox potential profile is deliberately determined for all the phases, including the one with Fe migration. The average redox potential for half desodition is slightly reduced from 3.88 to 3.75 V, following an increasing y value. Amongst three compounds, $N_{2.5}F_{1.75}S$ offers the highest specific capacity at 107 mAh/g. However, it leads to a nucleation of d-phase, which is anticipated to be the reason behind the sharp peak at 4.06 V in the experimental dQ/dV plot. Moreover, $N_3F_{1.5}S$ is regarded as a promising alternative to the well-known $N_{2.5}F_{1.75}S$ cathode as it can provide a nearly similar capacity at 91 mAh/g and a superior structural reversibility.

The last chapter focuses on $NaMPO_4$ and $MMoO_4$, which are used as cathodes in hybrid supercapacitors. In this part, the first-principles approach is employed to explain and support experimental results. In the case of $NaMPO_4$, the crystal structures and electronic properties $NaNiPO_4$ in maricite and triplylite phases are studied. Our result indicates that both phases show an electrochemical activity of $Ni^{2+/3+}$ redox reaction, and the superior capacitance for the triplylite phase is mainly contributed from the additional intercalation. To improve the performance for the maricite-$NaNiPO_4$, a mixed-$NaMn_{1/3}Co_{1/3}Ni_{1/3}PO_4$ is synthesized. The minimum energy configuration of the mixed compound is obtained according to the homogeneity of charge distribution. In a nutshell, the mixed compound is predicted to show faradaic behavior, mainly contributed from the Ni and Mn redox reactions, along with an improved electronic conductivity.

Moreover, we study the effect of M transition metal substitution on phase stability, electronic properties and charge transfer in $MMoO_4$ with $M = $ Mn, Co and Ni. While $MnMoO_4$ crystallizes in α phase, $CoMoO_4$ and $NiMoO_4$ prefer forming in β phase. The reason behind the higher redox potential of $NiMoO_4$ is relevant to the strong electrostatic repulsion between Ni cations. Our result suggests that the highest capacitance in $NiMoO_4$ amongst other $MnMoO_4$ is attributed to the higher surface area. Experimental effort is made to develop a new ternary metal oxide based on Mn-Co-Ni molybdate with the chemical formula of $Mn_{1/3}Co_{1/3}Ni_{1/3}MoO_4$ (or $MCNMoO_4$). Using the SQS method, we determine its stable structure crystallizing in β phase. Based on the crystal structure and electronic properties, we can identify a source of the improved cycling efficiency and specific capacitance of $MCNMoO_4$ compound.

7. Svensk sammanfattning

I den här avhandlingen har ramverket från DFT använts för att studera och förutsäga egenskaper hos polyanjoniska katodmaterial Na-jonbatterier och hybrida superkondensatorer. P.g.a. den induktiva effekten hos polyanjoniska föreningar användes huvudsakligen PBE+U-funktionalen i alla beräkningar för att noggrant beskriva högst lokaliserade elektroner. Den här avhandlingen är uppdelad i fem kapitel. Det första kapitlet tar upp betydelsen och bakgrunden till energilagring tillsammans med motiveringarna för den här avhandlingen. I kapitel två beskriver vi på enkelt sätt DFT-formalismen och alla andra teoretiska metoder, vilka användes i avhandlingen. Sen ges alla uppnådda resultat i de sista tre kapitlen, vilket kan sammanfattas på följande sätt.

Kapitel tre är först och främst inriktat på att genomskåda insättningsmekanismen för Na i krönkitliknande katodmaterial, $Na_2Fe(SO_4)_2 \cdot 2H_2O$, (kallade NFS2H). Resan mot målet Resan mot målet bröjar med en fundamental förståelse av bulkegenskaper hos NFS2H. Vätebindningar associerade med strukturella H_2O-enheter upptäcktes ha en avgörande inverkan på stabiliteten hos strukturen och laddningsöverföring inom inter- och intrapseudolager. Fastän totalt borttagande av natrium inte är möjligt p.g.a. begränsníngen av elektrolytfönstret, ser vi en högre spänning vid halvt borttagande av natrium vid 4,01 V jämfört med den experimentella (3,25 V). Detta kännetecknas av en okänd strukturell förändring inducerad av vattenadsorption i NFS2H. Baserat på vakansassisterad diffusion och NEB-metoden fann vi, att insättningsmekanismen för Na långsamt sker längs $[01\bar{1}]$-riktningen med en migrationsenergi på 1,16 eV. P.g.a. den höga migrationsenergin tros naturliga defekter vara ansvariga för den snabba jondiffusionen, vilket är experimentellt rapporterat.

För att kunna undersöka defektbildningar i NFS2H, fastställer vi systematiskt kemisk-potentialdiagram under termodynamisk jämvikt. De beräknade diagrammen avslöjar existensen av sekundära faser, vilket stämmer överens med experimentella observationer och ger oss ett passande omfång av atomära kemiska potentialer för kristalltillväxten av NFS2H-katoden. Eftersom NFS2H till största delen syntetiseras i vätskelösning, approximeras pH-värdet för syntetiseringstillstånden genom att använda den kemiska potentialen för väte. Resultatet visar sura tillväxttillstånd ($2,0 < pH < 6,4$). Dessutom undersöktes defektformationen i varje jämviktstillstånd vid olika pH-värden. De dominanta defekterna i NFS2H har visat sig vara antingen of Fe_{Na}, V_{Na} eller Na_{Fe} och deras koncentration kan manipuleras genom att ställa in pH-värdet i utgångslösningen. Fe_{Na}-kanalblockaget är dominant vid lågt pH, men kan undertryckas vid pH mellan 4,0 och 5,6 där V_{Na} och Na_{Fe} blir övervägande.

De här defekterna kan också inducera små hålpolaroner, vilket resulterar i förhöjd elektronisk ledningsförmåga vid svag surt tillstånd. Här visar vi att befintlighet av Na_{Fe} är fördelaktig jondiffusionen, eftersom det öppnar en alternativ väg som leder över varje [01$\bar{1}$] diffusionskanal, vilket förmildrar defekternas inverkan. Dessutom möjliggör det en snabbare diffusion jämfört med den längs den väsentliga diffusionskanalen. Därför är den här mekanismen en nyckelfaktor för den förbättrade jonledningsförmågan, som observeras i nanostrukturerad NFS2H.

I kapitel fyra undersöker vi det non-stökiometriska beteendet i alluauditlik-nande $Na_{2+2\delta}Fe_{2-\delta}(SO_4)_3$ katoder för δ = 0, 0,25 och 0,5 (i termer av N_xF_yS där y = 2, 1,75 and 1,5). Den slumpvisa utbytesmetoden har använts för att hitta deras minimala energikonfiguration och fär att visa ett samband mellan energiutbytet och distributionsmönstret av Na i den här klassens material. Resultatet visar den optimala läget i en sekvens av Na4 > Na1 > Na2 > Na3 enligt insättningsmekanismen för Na. Användandet av supercell är ytterst viktigt för att noggrant kunna beskriva non-stäkiometrin i N_xF_yS. Här näst konstrueras kemisk-potentialdiagrammen för varje förening för att förstå skillnaden ur ett termodynamiskt perspektiv och definiera intervallet av kemiska potentialer för energiberäkningar hos defekter. Våra beräknade diagram visar vackert den oundvikliga utfällningen av $Na_6Fe(SO_4)_4$- och $FeSO_4$-fasorenheter, vilket kan ses i experiment. Intressant nog visar det också mäjligheten för att minimera orenhetskoncentrationen i varje N_xF_yS, särkilt i N_2F_2S.

Baserat på de framtagna kemiska potentialerna beräknas formationsenergierna för defekter enligt olika experimentella förutsättningar. Framför allt visar N_xF_yS på en hög concentration av naturligt förekommande defekter, vilka uppkommer spontant under vissa förutsättningar. Resultatet visar med god överensstämmelse den experimentella tendensen för orenhetsutfällning. Dessutom visar det en osannolik formation av kanalblockage och formationen av Fe_{Na}^{1+}-V_{Na}^{1-}- och Na_i^{1+}-Na_{Fe}^{1-}-dominanta orenhetskomplex i de här föreningarna. Slutligen identifierar vi Na_i^{1+}-Na_{Fe}^{1-} som ett ursprung till den inneboende non-stökiometrin, därför att det endast är dominant i den stökiometriska föreningen.

Vidare har profilen hos redoxpotentialen och insättningsmekanismen för Na studerats för varje förening. Vi visar på möjlighet för strukturell utveckling vid borttagande Na, framför allt efter inledande borttagande av Na1. Först får N_xF_yS-föreningar små förändringar, vilka leder till gitterexpansion och strukturella omfördelningar från Fe_2O_{10}-bioktahedrisk till två FeO_5-trigonala bipyramider (kallade d-fas). När fler Na^+-joner tas bort, blir kristallgittret kraftigt förstorat och förändrat till en annan C2/c-struktur (kallad t-fas). De här två faserna förväntas visa sämre prestation Na-jondiffusion jämfört med den ursprungliga, medan det elektrokemiska beteendet knappt förändras p.g.a. deras liknande elektroniska struktur. Dessutom har profilen för redoxpotentialen bestämts för alla faser, också den med Fe-migration. Medelvärdet av

redoxpotentialen för halvt borttagande av Na är lite förminskad från 3,88-3,75 V, följt av ett förhöjt y-värde. Bland de tre föreningarna har $N_{2.5}F_{1.75}S$ högst specifik kapacitet, 107 mAh/g. Dock leder det till en kärnbildning av d-fasen, vilket antas vara anledningen till den skärpa piken vid 4,06 V i den experimentella dQ/dV-grafen. Dessutom anses $N_3F_{1.5}S$ vara ett bra alternative till den välkända $N_{2.5}F_{1.75}S$-katoden, eftersom den kan ge liknande kapacitet, 91 mAh/g och har överlägsen strukturell reversibilitet.

Det sista kapitlet fokuserar på NaMPO$_4$ och MMoO$_4$, vilka används som katoder i hybrida superkondensatorer. I den här delen används första princip-metoder för att förklara och backa upp experimentella resultat. När det gäller NaMPO$_4$, studeras kristallstruktur och elektroniska egenskaper hos NaNiPO$_4$ i marikit- och trifylitfaser. Våra resultat visar elektrokemisk aktivitet i båda faserna hos Ni$^{2+/3+}$-redoxreaktionen och den överlägsna kapaciteten hos tri-fylitfasen beror främst på den tillagda insättningen. För att öka prestationen hos marikit-NaNiPO$_4$, syntetiserades en mixad- NaMn$_{1/3}$Co$_{1/3}$Ni$_{1/3}$PO$_4$. Kon-figurationen med minst energi hos den mixade föreningen tas fram enligt den homogena laddningsfördelningen. Kortfattat tros den mixade föreningen visa faradiskt beteende, mestadels från Ni- och Mn-redoxreaktionerna tillsammans med ökad elektronisk ledningsförmåga.

Dessutom studerar vi effekten av utbyte av M-övergångsmetaller hos fasstabiliteten, elektroniska egenskaper och laddningsförflyttning hos MMoO$_4$ med M = Mn, Co and Ni. Medan MnMoO$_4$ kristalliseras i α-fas, föredrar CoMoO$_4$ och NiMoO$_4$ att bildas i β-fas. Anledningen till den högre redoxpotentialen hos NiMoO$_4$ är relevant för de starka elektrostatiska repulsionerna mellan Ni-katjoner. Våra resultat föreslår att den högsta kapacitansen hos in NiMoO$_4$ bland andra MnMoO$_4$ är p.g.a. den större ytan. Experimentella försök har gjorts för att utveckla en ny ternär metalloxid baserad på Mn-Co-Ni-molybdat med den kemiska formeln Mn$_{1/3}$Co$_{1/3}$Ni$_{1/3}$MoO$_4$ (eller MCNMoO$_4$). Genom att använda oss av SQS-metoden, kan vi bestämma dess stabila struktur, vilken kristalliseras i β-fas. Baserat på kristallstrukturen och elektroniska egenskaper kan vi identifiera den förbättrade cykeleffektiviteten och specifik kapacitet hos MCNMoO$_4$-föreningen.

8. Acknowledgements

This thesis would be never completed without people who have helped me during my last four and half years. Therefore, I would like to take this opportunity to thanks them all.

First of all, I would like to express my deepest regards and gratitude to my supervisor, Prof. Rajeev Ahuja, for giving me a great opportunity to pursue my PhD in his group at Uppsala university, and also for his excellent encouragements and suggestions that make me improve myself and grow as an independent researcher. Secondly, I also want to express my very great appreciation to Dr.Sudip Chakraborty, my co-supervisor, who have continuously helped and encouraged me to get through all the good and bad moments. I truly appreciate his ever-lasting support and patience. I am deeply indebted to the Development and Promotion of Science and Technology Talents Project, Royal Thai government for my scholarship. I submit my heartiest gratitude to my respected Assoc.Prof.Jiraroj T-Thienprasert for very fruitful discussions and interesting ideas. I acknowledge Dr.Manickam Minakshi for the inspiring collaboration experiences in the projects of hybrid supercapacitors.

I am really thankful to Cleber and Emil, my office mate, and also John for their kind helps in every thing. Importantly for bringing up a variety of interesting topics during Fika and Unico time. Many thanks to Amitava for all interesting discussion during lunch time and all entertaining moments. I would like to say thank you to all of my colleagues at the division of Material Theory, particularly, Vivek, Rafael, Arnab, Rubab, Xiao, Sankar, Dr.Tanveer, Xiaoyang, Pritam, Jose, Rodrigo, Emel, Giane, Xin, Dua, Dr.Wei, Dr.Moyses, Dr.Anton, for providing me a great work environment. I am appreciated help from John for the Swedish translation of the summary and also all suggestions and comments from Sudip, Arnab, Rubab, Pritam and Vivek on this thesis.

I am thankful to all Thai friends in Sweden, P'Dew, P'Pikae, P'Cherry, P'Toon, P'M (SLU), P'Noon, P'Tiger, P'Bier, P'View, P'Tong, P'Bow, P'M, P'Tae, P'First, N'Sek and N'Jan, for making my time in Sweden memorable. My studies would have been more difficult without the warm and friendly atmosphere these people created. I also thanks my Super landlords, Pa'Jamlong and Sigge, for their wonderful warm-hearted caring that makes Sweden like my second home. Come to the last, but not least, I thanks my beloved family for their unconditional love, remote mental supports and endless encouragements. And very special thank to my dearest girlfriend, Mook ><, who brightens me up in the darkest days and always be there besides me.

References

[1] Glenn G. Amatucci, Fadwa Badway, Aurelien Du Pasquier, and Tao Zheng. An asymmetric hybrid nonaqueous energy storage cell. *Journal of The Electrochemical Society*, 148(8):A930–A939, 2001.

[2] Vladimir I Anisimov, F Aryasetiawan, and A I Lichtenstein. First-principles calculations of the electronic structure and spectra of strongly correlated systems: the lda+u method. *Journal of Physics: Condensed Matter*, 9(4):767–808, jan 1997.

[3] Rafael B. Araujo, Sudip Chakraborty, and Rajeev Ahuja. Unveiling the charge migration mechanism in Na_2O_2: implications for sodiumâair batteries. *Phys. Chem. Chem. Phys.*, 17:8203–8209, 2015.

[4] Rafael B Araujo, Sudip Chakraborty, Prabeer Barpanda, and Rajeev Ahuja. $Na_2M_2(SO_4)_3$ (m = fe, mn, co and ni): towards high-voltage sodium battery applications. *Phys. Chem. Chem. Phys.*, (14):9658–9665.

[5] I.G. Austin and N.F. Mott. Polarons in crystalline and non-crystalline materials. *Advances in Physics*, 18(71):41–102, 1969.

[6] P. Axmann, C. Stinner, M. Wohlfahrt-Mehrens, A. Mauger, F. Gendron, and C. M. Julien. Non-stoichiometric $LiFePO_4$: Defects and related properties. *Chemistry of Materials*, 21(8):1636–1644, 2009.

[7] M K Aydinol, A F Kohan, and G Ceder. Ab initio calculation of the intercalation voltage of lithium-transition-metal oxide electrodes for rechargeable batteries. *Journal of Power Sources*, 68(2):664–668, 1997.

[8] M. K. Aydinol, A. F. Kohan, G. Ceder, K. Cho, and J. Joannopoulos. Ab initio study of lithium intercalation in metal oxides and metal dichalcogenides. *Physical Review B*, 56(3):1354–1365, 1997. PRB.

[9] Wilder D Bancroft and H L Davis. Raoult's Law. *The Journal of Physical Chemistry*, 33(3):361–370, 1928.

[10] Prabeer Barpanda. Sulfate chemistry for high-voltage insertion materials: Synthetic, structural and electrochemical insights. *Israel Journal of Chemistry*, 55(5):537–557, 2015.

[11] Prabeer Barpanda, Gosuke Oyama, Chris D. Ling, and Atsuo Yamada. Kröhnkite-type $Na_2Fe(SO_4)_2 \cdot 2H_2O$ as a novel 3.25 V insertion compound for na-ion batteries. *Chemistry of Materials*, 26(3):1297–1299, 2014.

[12] Prabeer Barpanda, Gosuke Oyama, Shin-ichi Nishimura, Sai-Cheong Chung, and Atsuo Yamada. A 3.8-V earth-abundant sodium battery electrode. *Nature Communications*, 5:4358, 2014.

[13] A. D. Becke. Density-functional exchange-energy approximation with correct asymptotic behavior. *Phys. Rev. A*, 38:3098–3100, Sep 1988.

[14] P. E. Blöchl. Projector augmented-wave method. *Physical Review B*, 50(24):17953–17979, 1994. PRB.

[15] M. Born and R. Oppenheimer. Zur quantentheorie der molekeln. *Annalen der Physik*, 389(20):457–484, 1927.

[16] Thierry Brousse, Daniel Bélanger, and Jeffrey W. Long. To be or not to be pseudocapacitive? *Journal of The Electrochemical Society*, 162(5):A5185–A5189, 2015.

[17] Thierry Brousse, Mathieu Toupin, and Daniel Bélanger. A hybrid activated carbon-manganese dioxide capacitor using a mild aqueous electrolyte. *Journal of The Electrochemical Society*, 151(4):A614–A622, 2004.

[18] Steven J. F. Byrnes. Basic theory and phenomenology of polarons. 2010.

[19] D. M. Ceperley and B. J. Alder. Ground state of the electron gas by a stochastic method. *Phys. Rev. Lett.*, 45:566–569, Aug 1980.

[20] Sudip Chakraborty, Amitava Banerjee, Teeraphat Watcharatharapong, Rafael B Araujo, and Rajeev Ahuja. Current computational trends in polyanionic cathode materials for Li and Na batteries. *Journal of Physics: Condensed Matter*, 30(28):283003, jun 2018.

[21] M W Chase, Standards National Institute of, and Technology. *NIST-JANAF thermochemical tables*. American Chemical Society ; American Institute of Physics for the National Institute of Standards and Technology, [Washington, D.C.]; Woodbury, N.Y., 1998.

[22] Sung-Yoon Chung, Jason T. Bloking, and Yet-Ming Chiang. Electronically conductive phospho-olivines as lithium storage electrodes. *Nat Mater*, 1(2):123–128, 2002. 10.1038/nmat732.

[23] Sung-Yoon Chung, Young-Min Kim, and Si-Young Choi. Direct physical imaging and chemical probing of $LiFePO_4$ for lithium-ion batteries. *Advanced Functional Materials*, 20(24):4219–4232.

[24] Matteo Cococcioni. The lda+u approach: A simple hubbard correction for correlated ground states. 2012.

[25] Matteo Cococcioni and Stefano de Gironcoli. Linear response approach to the calculation of the effective interaction parameters in the $LDA + U$ method. *Phys. Rev. B*, 71:035105, Jan 2005.

[26] A.R. Dehghani-Sanij, E. Tharumalingam, M.B. Dusseault, and R. Fraser. Study of energy storage systems and environmental challenges of batteries. *Renewable and Sustainable Energy Reviews*, 104:192 – 208, 2019.

[27] Jia Ding, Wenbin Hu, Eunsu Paek, and David Mitlin. Review of hybrid ion capacitors: From aqueous to lithium to sodium. *Chemical Reviews*, 118(14):6457–6498, 2018. PMID: 29953230.

[28] P. A. M. Dirac. Note on exchange phenomena in the thomas atom. *Mathematical Proceedings of the Cambridge Philosophical Society*, 26(3):376â385, 1930.

[29] D. P. Dubal, O. Ayyad, V. Ruiz, and P. Gmez-Romero. Hybrid energy storage: the merging of battery and supercapacitor chemistries. *Chem. Soc. Rev.*, 44:1777–1790, 2015.

[30] S. L. Dudarev, G. A. Botton, S. Y. Savrasov, C. J. Humphreys, and A. P. Sutton. Electron-energy-loss spectra and the structural stability of nickel oxide: An LSDA+U study. *Physical Review B*, 57(3):1505–1509, 1998. PRB.

[31] Debasmita Dwibedi, Chris D. Ling, Rafael B. Araujo, Sudip Chakraborty, Shanmughasundaram Duraisamy, Nookala Munichandraiah, Rajeev Ahuja, and Prabeer Barpanda. Ionothermal synthesis of high-voltage alluaudite $Na_{2+2\delta}Fe_{2-\delta}(SO_4)_3$ sodium insertion compound: Structural, electronic, and

magnetic insights. *ACS Applied Materials & Interfaces*, 8(11):6982–6991, mar 2016.

[32] Brian Ellis, Laura K. Perry, Dominic H. Ryan, and L. F. Nazar. Small polaron hopping in Li_xFePO_4 solid solutions:â coupled lithium-ion and electron mobility. *Journal of the American Chemical Society*, 128(35):11416–11422, 2006. PMID: 16939264.

[33] Paul Erhart, Andreas Klein, Daniel Åberg, and Babak Sadigh. Efficacy of the dft+*u* formalism for modeling hole polarons in perovskite oxides. *Phys. Rev. B*, 90:035204, Jul 2014.

[34] R. P. Feynman. Forces in molecules. *Phys. Rev.*, 56:340–343, Aug 1939.

[35] Christoph Freysoldt, Blazej Grabowski, Tilmann Hickel, Jörg Neugebauer, Georg Kresse, Anderson Janotti, and Chris G. Van de Walle. First-principles calculations for point defects in solids. *Rev. Mod. Phys.*, 86:253–305, Mar 2014.

[36] Christoph Freysoldt, Jörg Neugebauer, and Chris G. Van de Walle. Fully ab initio finite-size corrections for charged-defect supercell calculations. *Physical Review Letters*, 102(1):016402, 2009. PRL.

[37] Colin W. Glass, Artem R. Oganov, and Nikolaus Hansen. USPEX-evolutionary crystal structure prediction. *Computer Physics Communications*, 175(11):713 – 720, 2006.

[38] Zhengliang Gong and Yong Yang. Recent advances in the research of polyanion-type cathode materials for Li-ion batteries. *Energy Environ. Sci.*, 4:3223–3242, 2011.

[39] J.B. Goodenough and K. Mizushima. Electrochemical cell with new fast ion conductors, 1981. US Patent 4,302,518.

[40] Stefan Grimme. Semiempirical gga-type density functional constructed with a long-range dispersion correction. *Journal of Computational Chemistry*, 27(15):1787–1799, 2006.

[41] Stefan Grimme. Semiempirical GGA-type density functional constructed with a long-range dispersion correction. *Journal of Computational Chemistry*, 27(15):1787–1799, 2006.

[42] Reema Gupta, Shibu Saha, Monika Tomar, V. K. Sachdev, and Vinay Gupta. Effect of manganese doping on conduction in olivine $LiFePO_4$. *Journal of Materials Science: Materials in Electronics*, 28(7):5192–5199, 2017.

[43] Arturo Gutierrez, Nicole A. Benedek, and Arumugam Manthiram. Crystal-chemical guide for understanding redox energy variations of $M^{2+/3+}$ couples in polyanion cathodes for lithium-ion batteries. *Chemistry of Materials*, 25(20):4010–4016, 2013.

[44] G. Henkelman, B. P. Uberuaga, and H. A. Jónsson. A climbing image nudged elastic band method for finding saddle points and minimum energy paths. *J. Chem. Phys.*, 113:9901, 2000.

[45] Jochen Heyd, Gustavo E. Scuseria, and Matthias Ernzerhof. Hybrid functionals based on a screened coulomb potential. *The Journal of Chemical Physics*, 118(18):8207–8215, 2003.

[46] Jochen Heyd, Gustavo E. Scuseria, and Matthias Ernzerhof. Erratum: Hybrid functionals based on a screened coulomb potential [j. chem. phys.118, 8207 (2003)]. *The Journal of Chemical Physics*, 124(21):219906, 2006.

[47] Khang Hoang and Michelle Johannes. Tailoring native defects in $LiFePO_4$: Insights from first-principles calculations. *Chemistry of Materials*, 23(11):3003–3013, 2011.

[48] P. Hohenberg and W. Kohn. Inhomogeneous electron gas. *Phys. Rev.*, 136:B864–B871, Nov 1964.

[49] Chi-Chang Hu, Kuo-Hsin Chang, Ming-Champ Lin, and Yung-Tai Wu. Design and tailoring of the nanotubular arrayed architecture of hydrous RuO_2 for next generation supercapacitors. *Nano Letters*, 6(12):2690–2695, 2006. PMID: 17163689.

[50] J. Hubbard and Brian Hilton Flowers. Electron correlations in narrow energy bands - IV. the atomic representation. *Proceedings of the Royal Society of London. Series A. Mathematical and Physical Sciences*, 285(1403):542–560, 1965.

[51] M. Saiful Islam, Daniel J. Driscoll, Craig A. J. Fisher, and Peter R. Slater. Atomic-scale investigation of defects, dopants, and lithium transport in the $LiFePO_4$ olivine-type battery material. *Chemistry of Materials*, 17(20):5085–5092, 2005.

[52] A. Janotti, C. Franchini, J. B. Varley, G. Kresse, and C. G. Van de Walle. Dual behavior of excess electrons in rutile TiO_2. *physica status solidi (RRL) â Rapid Research Letters*, 7(3):199–203, 2013.

[53] Anderson Janotti, David Segev, and Chris G. Van de Walle. Effects of cation *d* states on the structural and electronic properties of III-nitride and II-oxide wide-band-gap semiconductors. *Phys. Rev. B*, 74:045202, Jul 2006.

[54] Anderson Janotti, Joel B. Varley, Minseok Choi, and Chris G. Van de Walle. Vacancies and small polarons in $SrTiO_3$. *Phys. Rev. B*, 90:085202, Aug 2014.

[55] H. Jónsson, G. Mills, K. W. Jacobsen (eds Ciccotti G., B. J. Berne, and Coker D. F.) Ch. *Nudged Elastic Band Method for Finding Minimum Energy Paths of Transitions*. (World Scientific), 1998.

[56] Christian M. Julien, Alain Mauger, Karim Zaghib, and Henri Groult. Comparative issues of cathode materials for li-ion batteries. *Inorganics*, 2(1):132–154, 2014.

[57] Charles Kittel. *Introduction to Solid State Physics*. Wiley, 8 edition, 2004.

[58] Leonard Kleinman and D. M. Bylander. Efficacious form for model pseudopotentials. *Phys. Rev. Lett.*, 48:1425–1428, May 1982.

[59] W. Kohn. Nobel lecture: Electronic structure of matter—wave functions and density functionals. *Rev. Mod. Phys.*, 71:1253–1266, Oct 1999.

[60] W. Kohn and L. J. Sham. Self-consistent equations including exchange and correlation effects. *Phys. Rev.*, 140:A1133–A1138, Nov 1965.

[61] Hannu-Pekka Komsa, Tapio T. Rantala, and Alfredo Pasquarello. Finite-size supercell correction schemes for charged defect calculations. *Phys. Rev. B*, 86:045112, Jul 2012.

[62] G. Kresse and J. Furthm˙ Efficiency of ab-initio total energy calculations for metals and semiconductors using a plane-wave basis set. *Computational Materials Science*, 6(1):15 – 50, 1996.

[63] G. Kresse and J. Furthmüller. Efficient iterative schemes for ab initio total-energy calculations using a plane-wave basis set. *Phys. Rev. B*, 54:11169–11186, Oct 1996.

[64] G. Kresse and D. Joubert. From ultrasoft pseudopotentials to the projector augmented-wave method. *Physical Review B*, 59(3):1758–1775, 1999. PRB.

[65] G. Kresse and D. Joubert. From ultrasoft pseudopotentials to the projector augmented-wave method. *Physical Review B*, 59(3):1758–1775, 1999. PRB.

[66] Stephan Lany and Alex Zunger. Assessment of correction methods for the band-gap problem and for finite-size effects in supercell defect calculations: Case studies for zno and gaas. *Phys. Rev. B*, 78:235104, Dec 2008.

[67] Chengteh Lee, Weitao Yang, and Robert G. Parr. Development of the Colle-Salvetti correlation-energy formula into a functional of the electron density. *Phys. Rev. B*, 37:785–789, Jan 1988.

[68] A. I. Liechtenstein, V. I. Anisimov, and J. Zaanen. Density-functional theory and strong interactions: Orbital ordering in mott-hubbard insulators. *Phys. Rev. B*, 52:R5467–R5470, Aug 1995.

[69] Chaofeng Liu, Zachary G. Neale, and Guozhong Cao. Understanding electrochemical potentials of cathode materials in rechargeable batteries. *Materials Today*, 19(2):109 – 123, 2016.

[70] H. Liu, Q. Cao, L.J. Fu, C. Li, Y.P. Wu, and H.Q. Wu. Doping effects of zinc on $LiFePO_4$ cathode material for lithium ion batteries. *Electrochemistry Communications*, 8(10):1553 – 1557, 2006.

[71] Jiechen Lu and Atsuo Yamada. Ionic and electronic transport in alluaudite $Na_{2+2x}Fe_{2-x}(SO_4)_3$. *ChemElectroChem*, 3(6):902–905, 2016.

[72] G. Makov and M. C. Payne. Periodic boundary conditions in ab initio calculations. *Phys. Rev. B*, 51:4014–4022, Feb 1995.

[73] Rahul Malik, Damian Burch, Martin Bazant, and Gerbrand Ceder. Particle size dependence of the ionic diffusivity. *Nano Letters*, 10(10):4123–4127, 2010. PMID: 20795627.

[74] D. Marinova, V. Kostov, R. Nikolova, R. Kukeva, E. Zhecheva, M. Sendova-Vasileva, and R. Stoyanova. From krohnkite- to alluaudite-type of structure: novel method of synthesis of sodium manganese sulfates with electrochemical properties in alkali-metal ion batteries. *J. Mater. Chem. A*, 3:22287–22299, 2015.

[75] Delyana M. Marinova, Ekaterina N. Zhecheva, Rositsa R. Kukeva, Pavel V. Markov, Diana D. Nihtianova, and Radostina K. Stoyanova. Mixed sodium nickel-manganese sulfates: Crystal structure relationships between hydrates and anhydrous salts. *Journal of Solid State Chemistry*, 250:49 – 59, 2017.

[76] Richard M. Martin. *Electronic Structure: Basic Theory and Practical Methods*. Cambridge University Press, 2004.

[77] Christian Masquelier and Laurence Croguennec. Polyanionic (phosphates, silicates, sulfates) frameworks as electrode materials for rechargeable Li (or Na) batteries. *Chemical Reviews*, 113(8):6552–6591, 2013. PMID: 23742145.

[78] Thomas Maxisch, Fei Zhou, and Gerbrand Ceder. Ab initio study of the migration of small polarons in olivine $li_x fepo_4$ and their association with lithium ions and vacancies. *Phys. Rev. B*, 73:104301, Mar 2006.

[79] Nonglak Meethong, Yu-Hua Kao, Scott A. Speakman, and Yet-Ming Chiang. Aliovalent substitutions in olivine lithium iron phosphate and impact on structure and properties. *Advanced Functional Materials*, 19(7):1060–1070, 2009.

[80] Yu Meng, Qiufeng Li, Tiantian Yu, Sen Zhang, and Chao Deng. Architecture–property relationships of zero-, one- and two-dimensional carbon matrix incorporated na2fe(so4)2Â·2h2o/c. *CrystEngComm*, 18:1645–1654, 2016.

[81] Yu Meng, Sen Zhang, and Chao Deng. Superior sodium-lithium intercalation and depressed moisture sensitivity of a hierarchical sandwich-type nanostructure for a graphene-sulfate composite: a case study on na2fe(so4)2[middle dot]2h2o. *Journal of Materials Chemistry A*, 3(8):4484–4492, 2015.

[82] M. Minakshi, T. Watcharatharapong, S. Chakraborty, and R. Ahuja. A combined theoretical and experimental approach of a new ternary metal oxide in molybdate composite for hybrid energy storage capacitors. *APL Materials*, 6(4):047701, 2018.

[83] Manickam Minakshi, David Mitchell, Rob Jones, Feraih Alenazey, Teeraphat Watcharatharapong, Sudip Chakraborty, and Rajeev Ahuja. Synthesis, structural and electrochemical properties of sodium nickel phosphate for energy storage devices. *Nanoscale*, 8:11291–11305, 2016.

[84] K. Mizushima, P.C. Jones, P.J. Wiseman, and J.B. Goodenough. Lixcoo2 (0<x<-1): A new cathode material for batteries of high energy density. *Materials Research Bulletin*, 15(6):783 – 789, 1980.

[85] Hendrik J. Monkhorst and James D. Pack. Special points for brillouin-zone integrations. *Phys. Rev. B*, 13:5188–5192, Jun 1976.

[86] Qiao Ni, Ying Bai, Feng Wu, and Chuan Wu. Polyanion-type electrode materials for sodium-ion batteries. *Advanced Science*, 4(3):1600275–n/a, 2017. 1600275.

[87] Shyue Ping Ong, Yifei Mo, and Gerbrand Ceder. Low hole polaron migration barrier in lithium peroxide. *Phys. Rev. B*, 85:081105, Feb 2012.

[88] Shyue Ping Ong, Lei Wang, Byoungwoo Kang, and Gerbrand Ceder. Liâfeâpâo2 phase diagram from first principles calculations. *Chemistry of Materials*, 20(5):1798–1807, 2008.

[89] Gosuke Oyama, Shin-ichi Nishimura, Yuya Suzuki, Masashi Okubo, and Atsuo Yamada. Off-Stoichiometry in Alluaudite-Type Sodium Iron Sulfate $Na_{2+2x}Fe_{2-x}(SO_4)_3$ as an Advanced Sodium Battery Cathode Material. *ChemElectroChem*, 2(7):1019–1023, 2015.

[90] Gosuke Oyama, Oliver Pecher, Kent J Griffith, Shin-ichi Nishimura, Roberta Pigliapochi, Clare P Grey, and Atsuo Yamada. Sodium Intercalation Mechanism of 3.8 V Class Alluaudite Sodium Iron Sulfate. *Chemistry of Materials*, 28(15):5321–5328, 2016.

[91] A. K. Padhi, K. S. Nanjundaswamy, and J. B. Goodenough. Phosphoâolivines as positiveâelectrode materials for rechargeable lithium batteries. *J. Electrochem. Soc.*, 144(4):1188–1194, 1997.

[92] J. P. Perdew and Alex Zunger. Self-interaction correction to density-functional approximations for many-electron systems. *Phys. Rev. B*, 23:5048–5079, May 1981.

[93] John P. Perdew and Kieron Burke. Comparison shopping for a gradient-corrected density functional. *International Journal of Quantum Chemistry*, 57(3):309–319, 1996.

[94] John P. Perdew, Kieron Burke, and Matthias Ernzerhof. Generalized gradient approximation made simple. *Phys. Rev. Lett.*, 77:3865–3868, Oct 1996.

[95] John P. Perdew, Kieron Burke, and Matthias Ernzerhof. Generalized gradient approximation made simple [phys. rev. lett. 77, 3865 (1996)]. *Phys. Rev. Lett.*, 78:1396–1396, Feb 1997.

[96] John P. Perdew, Matthias Ernzerhof, and Kieron Burke. Rationale for mixing exact exchange with density functional approximations. *The Journal of Chemical Physics*, 105(22):9982–9985, 1996.

[97] John P. Perdew and Yue Wang. Accurate and simple analytic representation of the electron-gas correlation energy. *Phys. Rev. B*, 45:13244–13249, Jun 1992.

[98] Peter G. Bruce. *Solid state electrochemistry*. Cambridge University Press, New York, USA, 1995.

[99] Marine Reynaud, Mohamed Ati, Sylvain Boulineau, Moulay T. Sougrati, Brent C. Melot, Gwenaëlle Rousse, Jean-Noël Chotard, and Jean-Marie Tarascon. Bimetallic sulfates $A_2M(SO_4)_2 \cdot nH_2O$ (a = Li, Na and m = transition metal): as new attractive electrode materials for Li- and Na-ion batteries. *ECS Transactions*, 50(24):11–19, 2013.

[100] Baskar Senthilkumar, Kalimuthu Vijaya Sankar, Leonid Vasylechko, Yun-Sung Lee, and Ramakrishnan Kalai Selvan. Synthesis and electrochemical performances of maricite-NaMPO_4 (m = Ni, Co, Mn) electrodes for hybrid supercapacitors. *RSC Adv.*, 4:53192–53200, 2014.

[101] A L Shluger and A M Stoneham. Small polarons in real crystals: concepts and problems. *Journal of Physics: Condensed Matter*, 5(19):3049–3086, may 1993.

[102] P. J. Stephens, F. J. Devlin, C. F. Chabalowski, and M. J. Frisch. Ab initio calculation of vibrational absorption and circular dichroism spectra using density functional force fields. *The Journal of Physical Chemistry*, 98(45):11623–11627, 1994.

[103] Manickam Minakshi Sundaram, Teeraphat Watcharatharapong, Sudip Chakraborty, Rajeev Ahuja, Shanmughasundaram Duraisamy, Penki Tirupathi Rao, and Nookala Munichandraiah. Synthesis, and crystal and electronic structure of sodium metal phosphate for use as a hybrid capacitor in non-aqueous electrolyte. *Dalton Trans.*, 44:20108–20120, 2015.

[104] J. M. Tarascon and M. Armand. Issues and challenges facing rechargeable lithium batteries. *Nature*, 414:359â367, 11 2001.

[105] Richard J. D. Tilley. *Defects in Solids*. John Wiley Sons, Inc., 2008.

[106] Chris G. Van de Walle, D. B. Laks, G. F. Neumark, and S. T. Pantelides. First-principles calculations of solubilities and doping limits: Li, Na, and N in ZnSe. *Phys. Rev. B*, 47:9425–9434, Apr 1993.

[107] Chris G. Van de Walle and Jörg Neugebauer. First-principles calculations for defects and impurities: Applications to iii-nitrides. *Journal of Applied Physics*, 95(8):3851–3879, 2004.

[108] David Vanderbilt. Soft self-consistent pseudopotentials in a generalized eigenvalue formalism. *Phys. Rev. B*, 41:7892–7895, Apr 1990.

[109] J. B. Varley, A. Janotti, C. Franchini, and C. G. Van de Walle. Role of self-trapping in luminescence and p-type conductivity of wide-band-gap oxides. *Phys. Rev. B*, 85:081109, Feb 2012.

[110] Faxing Wang, Shiying Xiao, Yuyang Hou, Chenglin Hu, Lili Liu, and Yuping Wu. Electrode materials for aqueous asymmetric supercapacitors. *RSC Adv.*, 3:13059–13084, 2013.

[111] Guoping Wang, Lei Zhang, and Jiujun Zhang. A review of electrode materials for electrochemical supercapacitors. *Chem. Soc. Rev.*, 41:797–828, 2012.

[112] Teeraphat Watcharatharapong, Manickam Minakshi Sundaram, Sudip Chakraborty, Dan Li, GM Shafiullah, Robert D. Aughterson, and Rajeev Ahuja. Effect of transition metal cations on stability enhancement for molybdate-based hybrid supercapacitor. *ACS Applied Materials & Interfaces*, 9(21):17977–17991, 2017. PMID: 28481523.

[113] Teeraphat Watcharatharapong, Jiraroj T-Thienprasert, Prabeer Barpanda, Rajeev Ahuja, and Sudip Chakraborty. Mechanistic study of na-ion diffusion and small polaron formation in kröhnkite $Na_2Fe(SO_4)_2 \cdot 2H_2O$ based cathode materials. *J. Mater. Chem. A*, 5:21726–21739, 2017.

[114] Teeraphat Watcharatharapong, Jiraroj T-Thienprasert, Sudip Chakraborty, and Rajeev Ahuja. Defect formations and ph-dependent kinetics in kröhnkite $Na_2Fe(SO_4)_2 \cdot 2H_2O$ based cathode for sodium-ion batteries: Resembling synthesis conditions through chemical potential landscape. *Nano Energy*, 55:123 – 134, 2019.

[115] L L Wong, H M Chen, and S Adams. Sodium-ion diffusion mechanisms in the low cost high voltage cathode material $Na_{2+2\delta}Fe_{2-\delta}(SO_4)_3$. *Phys. Chem. Chem. Phys.*, 17(14):9186–9193, 2015.

[116] Xifeng Xia, Wu Lei, Qingli Hao, Wenjuan Wang, and Xin Wang. One-step synthesis of comoo4/graphene composites with enhanced electrochemical properties for supercapacitors. *Electrochimica Acta*, 99:253 – 261, 2013.

[117] A. Yamada, S. C. Chung, and K. Hinokuma. Optimized $LiFePO_4$ for lithium battery cathodes. *Journal of The Electrochemical Society*, 148(3):A224–A229, 2001.

[118] Jianyu Yao, Yongji Gong, Shubin Yang, Peng Xiao, Yunhuai Zhang, Kunttal Keyshar, Gonglan Ye, Sehmus Ozden, Robert Vajtai, and Pulickel M. Ajayan. Comoo4 nanoparticles anchored on reduced graphene oxide nanocomposites as anodes for long-life lithium-ion batteries. *ACS Applied Materials & Interfaces*, 6(22):20414–20422, 2014. PMID: 25380030.

[119] Akira Yoshino, Kenichi Sanechika, and Takayuki Nakajima. Secondary battery, May 1987. US Patent 4,668,595.

[120] K. Zaghib, J. Trottier, P. Hovington, F. Brochu, A. Guerfi, A. Mauger, and C.M. Julien. Characterization of na-based phosphate as electrode materials for electrochemical cells. *Journal of Power Sources*, 196(22):9612 – 9617, 2011.

[121] S. B. Zhang and John E. Northrup. Chemical potential dependence of defect formation energies in GaAs: Application to Ga self-diffusion. *Physical Review Letters*, 67(17):2339–2342, 1991. PRL.

[122] Fei Zhou, Kisuk Kang, Thomas Maxisch, Gerbrand Ceder, and Dane Morgan. The electronic structure and band gap of $LiFePO_4$ and $LiMnPO_4$. *Solid State Communications*, 132(3):181 – 186, 2004.

[123] Alex Zunger, S.-H. Wei, L. G. Ferreira, and James E. Bernard. Special quasirandom structures. *Phys. Rev. Lett.*, 65:353–356, Jul 1990.

[124] Wenhua Zuo, Ruizhi Li, Cheng Zhou, Yuanyuan Li, Jianlong Xia, and Jinping

Liu. Battery-supercapacitor hybrid devices: Recent progress and future prospects. *Advanced Science*, 4(7):1600539, 2017.

Acta Universitatis Upsaliensis

Digital Comprehensive Summaries of Uppsala Dissertations
from the Faculty of Science and Technology 1796

Editor: The Dean of the Faculty of Science and Technology

ACTA
UNIVERSITATIS
UPSALIENSIS
UPPSALA
2019